TABLE OF CONTENTS

Page

LIST OF TABLES

LIST OF FIGURES

CHAPTER 1 INTRODUCTION

Although pavements are primarily developed to carry traffic load, they also have to satisfy other functional characteristics. While functionality has historically been defined as the ability to provide a smooth, safe ride to the user, an aspect that is often overlooked is the comfort to the user and the residents living near the pavement.

The logical order of how pavement surface characteristics should be considered in the design process includes: safety, smoothness, and then comfort (including noise generation). However, there is a necessary trade off between these different characteristics. To improve the safety on a concrete pavement it is necessary to increase the friction between tire and pavement. This is usually accomplished by applying texture to the surface. Different textures provide different skid resistance and different noise levels. There is also, common thought that noisy surfaces are the best ones to provide skid resistance.

1.1 Research Objectives

The objectives this research are to:

- assess the influence of the depth, width, and shape of transverse tining on noise generation in PCC Pavements.
- assess the influence of pavement textures on noise generation.
- assess the influence of pavement texture profile on the noise and skid resistance.

1.2 Scope

This research attempts to link the contact stress between the tire and the pavement to the noise generated as the tire travels over the surface.

1.3 Technical Approach

A mathematical model was developed to determine the stress distribution between the concrete pavement and the tire. The stress distribution was transformed to a power density spectrum to represent the noise generated as the tire rolls over the surface. Stress-noise modeling was performed for a set of surfaces and tines geometries. Real scale testing was performed to obtain the noise generated over different surfaces. A laser profilometer was used to obtain an X, Y profile of different texture surfaces. The profile was used as an input for the stress model to obtain transfer functions to incorporate them in the mathematical model. An empirical transfer functions was generated in order to link the computer modeling with real scale testing. Friction testing was performed on the different surfaces and was related to the texture depth obtained from the laser profilometer.

1.4 Organization of Contents

This report presents a literature review in Chapter 2. Chapter 3 presents the use of a mathematical model used to perform predictions of noise levels in the form of power spectrum density plots. Chapter 4 contains results obtained from real scale testing using the Tire/Pavement Test Apparatus for different surface textures and shapes of tines. Chapter 5 presents surface characterization techniques used in this research to help to understand some of the noise generating mechanisms. Chapter 6 presents a way to link the mathematical modeling to the data obtained from testing on the tire pavement test

apparatus. Some of the implications and testing on friction are shown on Chapter 7. Chapter 8 presents a summary and conclusions.

CHAPTER 2 LITERATURE REVIEW

A review of the existing literature on tire-road interaction noise is presented in this chapter. The research needs were identified, and were used to formulate the objectives and research plan used in this study.

2.1 Tire-Road Noise

As the traffic volumes increase the problem of highway noise increases. For many years, research has been conducted on the way to minimize the noise generated by the vehicle. Vehicle noise is composed of various elements, but the two main noise generators are noise from the tire/road interaction and noise from the power train of the vehicle (power unit noise). Power unit noise is composed of the noise from the engine and all it accessories, transmission, and exhaust system noise.

At lower speeds power unit noise is dominant while at higher speeds the tire-road noise is dominant [Sandberg 2002]. There is a certain crossover speed when the noise emitted by the power unit is the same as the one emitted by the tire. Crossover speeds for constant-speed driving are usually reported to be 15-25 km/h for cars and 30-35 km/h for trucks [Sandberg 2002].

2.2 Sound

A wide range of pressure variations, perceived as loudness, and frequencies, perceived as pitch, can be heard by the human ear. A sound is described by both its loudness or intensity and its frequency. The intensity of sound is directly related to the

amplitude of the pressure fluctuations transmitted though the air or other medium and received by the ear [Bruel and Kjaer 2000].

2.2.1 Effect of Loudness

Loudness is a subjective determination of noise that is made by any individual. Small pressure fluctuations around barometric pressure travel as waves in air (or any other medium such as water) and flex the eardrum, creating a sensation of sound. The pressure range that a young, healthy ear can sense is approximately 20 μPa – 63 Pa. The weakest sound a healthy human ear can detect is 20 μPa, five billion times less than normal atmospheric pressure.

A healthy human ear can remarkably tolerate sound pressures more than a million times higher than 20 μPa. To avoid working with unmanageable sound pressure levels and due to the fact that the human auditory response is not linear in nature but rather is logarithmic, the decibel scale is used.

The decibel is an internationally accepted unit used to describe sound pressure fluctuations, perceived as loudness. The decibel, abbreviated as dB, is an indication of sound pressure level (SPL) (Equation 2.1).

$$SPL(dB) = 10\log_{10}(\frac{p^2}{p_0^2}) \tag{2.1}$$

where:

p = the ambient root-mean-square sound pressure; and

p_0 = the reference pressure (2×10^{-5} Pa)

The pressure range of 20 μPa to 63 Pa corresponds to a range of 0 to 130 dB, where 130 dB is the threshold of pain. Table 2.2.1 presents the decibel levels of some common sounds.

Table 2.2.1 Decibel levels of common sounds [Sandberg, 2002]

Effects:	Typical sound source	Sound Pressure (μPa)	Sound Pressure (dB)
Serious hearing damage	Space rocket launch, in the vicinity of the launch pad	200,000,000	140
Hearing damage and pain	Jet engine (25 m distance)	63,245,555	130
Hearing damage after short exposure	Air-raid alarm (5 m distance)	20,000,000	120
Serious hearing damaged hazard	Rock music concert, close to stage	6,324,555	110
Hearing hazard	Jet plane take-off (300 m)	2,000,000	100
Some hearing hazard	Noisy industrial hall	632,456	90
Health effects	Heavy truck, 70 $^{km}/_{h}$ (10 m distance)	200,000	80
Some health effects Severe annoyance	Car, 60 $^{km}/_{h}$ (10 m distance)	63,246	70
Annoyance	Normal conversation (1 m distance)	20,000	60
Some annoyance	Quiet conversation (1 m distance)	6,325	50
Good environment	Subdued radio music	2,000	40
	Whispering	632	30
	Quiet bedroom	200	20
	Rusting leave	63	10
Uncomfortably “quiet”	Anechoic room for sound measurements	20	0

2.2.2 Frequency

The human ear can also detect a large range in frequency, described as cycles per second and given the unit of hertz (Hz). The young healthy human ear can detect frequencies from 20 Hz to 20 kHz. The ear is most sensitive to the frequency range of 2 and 5 kHz [Bruel and Kjaer 2000].

The frequency component of sound is what gives it a tonal quality [Wayson 1998]. For example, the rumble of thunder has a low frequency while a whistle has a high frequency [Bruel and Kjaer 2000]. A sound that has only one frequency is called a pure tone but this is seldom encountered. Most industrial noise is known as broad-band noise and consists of a wide range of frequencies.

The difference in sensitivity to different frequencies is more pronounced at low SPLs (sound pressure levels) than it is at high SPLs as shown in Figure 2.2.1 as a family of equal loudness contours. The SPL required to give the same apparent loudness as a 1 kHz tone at any frequency can be determined in order by following the contour. For example, a 50 Hz tone must be 15 dB higher than a 1 kHz tone at a level of 70 dB in order to give the same subjective loudness. This means that a sound with a lower frequency will be perceived as less loud than one with a higher frequency.

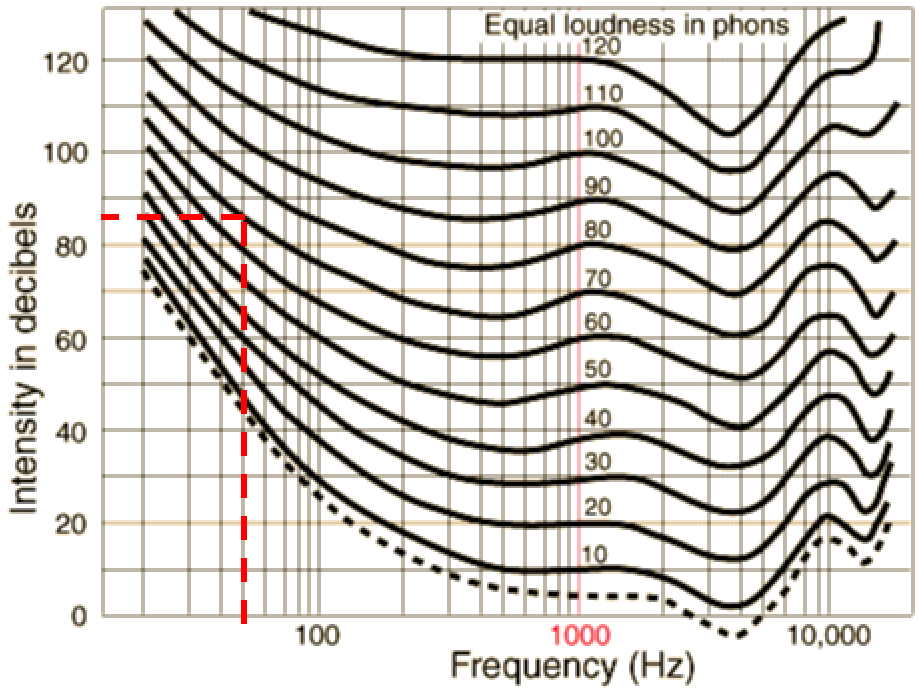

Figure 2.2.1 Equal loudness contours [http://hyperphysics.phy-astr.gsu.edu/]

Pressure variations travel through any elastic medium (such as air) at a given speed, denoted in Equation 2.2 as “c”. The speed of sound through air is generally taken as 770 mph or 344 m/s at room temperature. Frequency is inversely proportional to the wavelength.

$$f = \frac{c}{l} \tag{2.2}$$

where:

λ - wavelength

c - speed of sound

f - frequency

2.2.3 Spectral analysis

The one-third octave spectral analysis is a standard procedure used to analyze acoustical data. The method employs proportional, contrary to constant, bandwidth in the sense, that the spectral values are computed over bandwidth which increases with frequency in a logarithmic scale. This is done by using a series of band pass filters covering the various frequency ranges. A table showing the frequencies for the $^1/_3$ octave bands can be found in Appendix A.

Typically, a single decibel value is reported in road noise research, based on the summation of energy in the overall spectrum. Three basic scales - A, B, and C - have been developed and are internationally accepted. This weighting approximates the way the human ear perceives sound. Scale A represents the way our ears respond to moderate sounds, scale B is for more intense sounds and the C scale represents the way our ears would respond to very loud sounds. The A scale is used most often, and it is designated dB (A). The "A" weighting procedure is described in more detail on 3.1.3 Generation of the Power Density Spectrum.

2.2.4 Sound Propagation

Sound propagates uniformly in all directions decreasing in amplitude as it moves further from the sound source in a free-field condition. When sound encounters an obstacle, part of the sound will be reflected, part of the sound will be absorbed, and part of the sound will be transmitted through the object. How much of the sound is reflected,

absorbed, and transmitted will depend on the amplitude and wavelength of the sound wave and the object's properties.

2.3 What is Noise?

Noise could be described as a sound that is unpleasant. It is however very subjective and depends upon recipient's perception of the noise. Noise is any sound that is unpleasant, generally any sound that interferes with other sounds especially those of speech. It also depends on the kind and magnitude of the sound.

2.4 Noise Generating and Propagating Mechanisms Resulting from Tire/Road Interaction

According to Sandberg [1999], there exists several sound generating and propagating mechanisms and a full understanding of these is necessary to understand the phenomena involved in noise generation due to tire road interaction.

The sound generating mechanisms of tire-road noise generation are commonly divided into two main groups, according to the media in which they occur and their effects. The first one is related to the mechanical vibrations of the tire, termed "structure-borne", and the second, related to the aerodynamic phenomena, called "air-borne". The structure-borne noise can further be classified into impacts and shocks, and adhesion mechanisms [Nelson and Phillips 1994]. The relative contributions of these mechanisms vary with the type of tire, road surface, and vehicle speed [Sandberg and Ejsmont 2002, Nelson 1994]. Figure 2.4.1 shows some of the mechanisms, which are explained in the following sections.

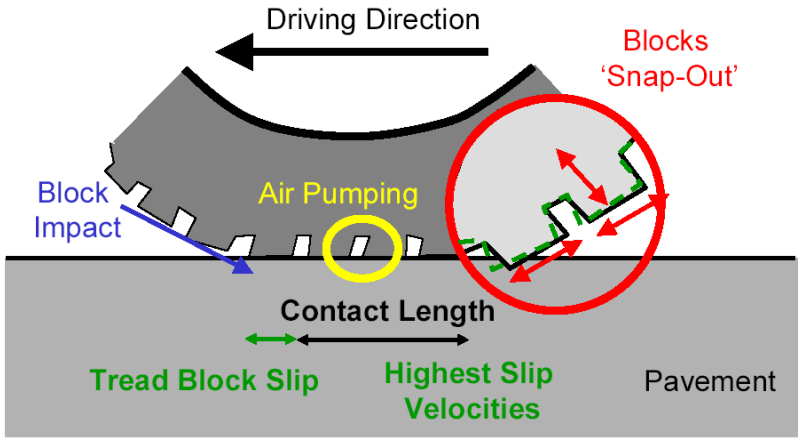

Figure 2.4.1 Overview of noise generation mechanisms [after Nelson 1994]

The main noise generating mechanisms are listed in Table 2.4.1. Furthermore, there are phenomena closely related to the generating mechanisms, which influence the amplitude but which cannot be regarded as pure generation; these are also listed on Table 2.4.1.

Table 2.4.1 Mechanisms of tire/road noise emission [Sandberg, 1999]

Generation Mechanisms	Radial Vibration Mechanism	Impact of tire tread blocks or other pattern elements on road surfaces. Impact of road surface texture on the tire treads.
	Air Resonance Mechanism	Pipe resonance. Helmholtz resonance. Pocket air-pumping.
	Adhesion Mechanism	Stick/slip motions causing tangential tire vibrations. Rubber-to-road stick/release (adhesive effect).
Special amplification or reduction mechanisms	The Horn effect	The curved volume between the tire leading and trailing edges and the pavement constitute something similar to an exponential horn used to amplify sound.
	The Acoustical Impedance effect	Communicating voids in porous surfaces act like sound absorbing material, affecting the source strength. Same, affecting sound propagation to far-field receiver.
	The Mechanical Impedance effect	Pavement gives more or less reaction to tire block impacts depending on dynamic tire/road stiffness proportions. Some tire vibrations may be transferred to the pavement, possibly radiating as sound (speculation).

2.4.1 Structure-Borne Noise

Structure-borne noise travels thru the structure of the tire. The next two sub-sections describe some of its generating mechanisms.

2.4.1.1 Impacts and Shocks

Vibrations are generated in the tires due to the impacts and deflections of the rubber which occur as the tread blocks enter and leave the contact patch with the road surface and as a result of movement of tread elements in contact with the pavement. Vibrations in the tread and sidewall of the tire excite the air surrounding the tire, generating sound pressure waves that propagate away from the tire.

Figure 2.4.2 is a concise representation of the mechanisms of tire-road noise generation, depicting the mechanisms as the tire rolls. As the tread block impacts the road surface, vibrations are driven radially into the tire (Figure 2.4.2a). While the tread block moves through the contact patch, it is subjected to compression, whereas the compression is released when the block leaves the contact patch. This sudden release of compression returns the tire back to its undeflected rolling radius. This phenomenon is known as block snap-out, which excites both the radial and tangential vibration modes [Nelson and Phillips 1994]. The tread compression, as shown in Figure 2.4.2b, also induces radial vibration of the tire carcass. Both these phenomena occur at the lower end of the frequency range (<1 KHz). Another impact phenomenon, this one resulting in vibration, is the tread oscillation. It is attributed to the tangential strain on the tread blocks and impact of the pavement, and is a process dominated at the high frequency range (>1 KHz) [Brite Euram-3415 1994].

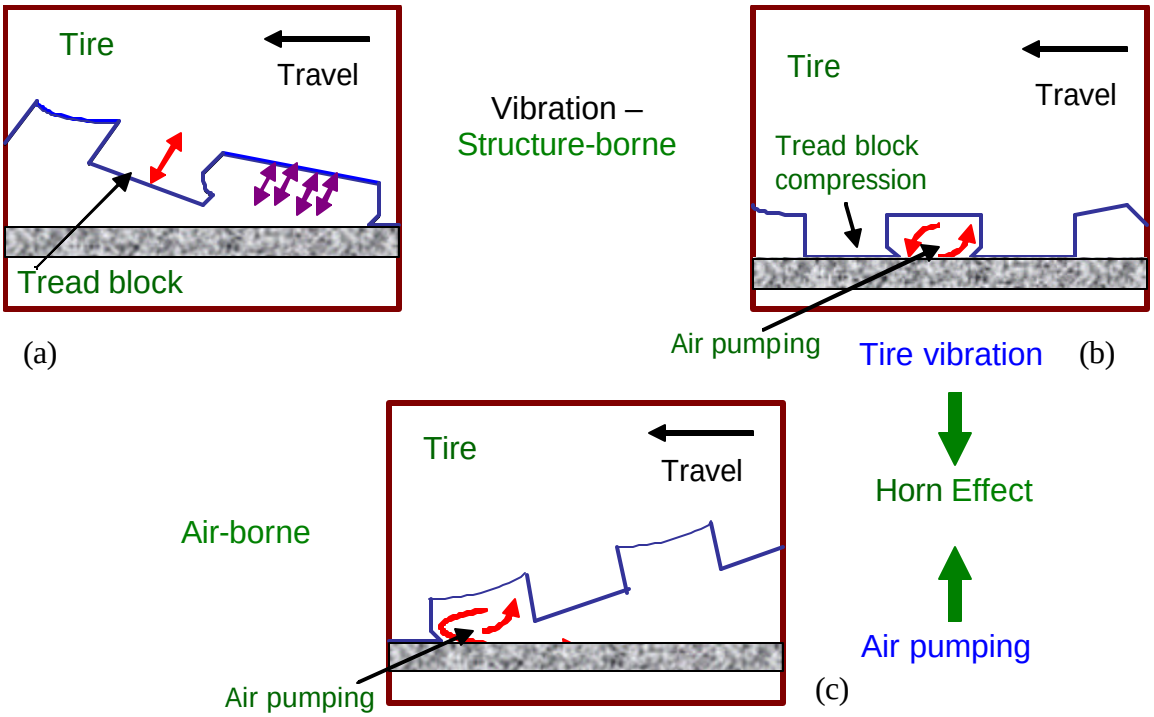

Figure 2.4.2 Different mechanisms of tire-road noise generation; a) Tread block impact, b) Tread block compression, c) Tread block snap-out

2.4.1.2 Adhesion Mechanisms

Adhesion mechanisms are set up by the tire vibrations associated with the frictional losses created in the contact patch between the tire and the pavement [Sandberg and Ejsmont 2002]. These are predominantly tangential forces, produced by the changing radial deflection when the tire flattens in the contact patch. These forces are resisted by friction between the tire and the pavement and by tire stiffness. The friction mechanism is governed by the small scale roughness characteristics or microtexture of the pavement surface [Nelson 1994].

2.4.2 Air Borne Noise

Tire-pavement noise is also generated by several mechanisms which are related to the movement of air in the cavities of the tread pattern. The most common of the air-borne mechanisms is air pumping, shown in Figure 2.4.2c. When the tread block enters the contact patch, air is "sucked in" between the grooves of the tread pattern, and when it leaves the contact patch, air is "pumped out". The pressure modulations caused by this

process are responsible for high frequency noise. Additional air-borne generation mechanisms include:

i. Air turbulence, which is the turbulence around the tire due to the tire displacing air when rolling,
ii. Pipe resonance, which is the air displacement in the grooves in the tire tread, and
iii. Helmholtz resonance, which is the air displacement into or out of the connected air cavities in the tread pattern and pavement surface.

The latter two mechanisms are often considered as special cases of air pumping [Sandberg and Ejsmont 2002].

2.4.3 Amplification or Reduction Mechanisms

Though not strictly generation mechanisms, several other mechanisms in addition to the primary ones described earlier also have been found to augment or reduce the tire-pavement interaction noise. The most important of them is the horn effect. Noise generated at or near the contact patch can be amplified due to the shape of the region between the tire and the pavement surface, immediately in front and to the rear of the contact patch. Multiple reflections between the tire and pavement surface tend to occur, amplifying the sound [Descornet et al. 2000, and Nelson 1994].

2.5 Pavement Structure and Texture Optimization to Reduce Noise

The acoustic and mechanical impedance effects of the pavement surface are suggested as noise reducing mechanisms. The acoustic impedance depends on the communicating voids in the pavement whereas the mechanical impedance depends on the relative stiffness of the tire and the pavement. Much research has been performed to promote the area of quiet highways [Sandberg 2002]. However, few roadways have been developed which provide noise reduction while maintaining long-term safety and durability. The surface texture of concrete pavement selected for a given location is

typically a function of several variables including the amount of traffic, climate, speed limit, cost, and increasingly, location with respect to densely populated areas. While the main purpose of the surface texturing is to enhance safety by reducing the number of wet-weather accidents, increasingly larger numbers of agencies are concerned with reducing tire/road noise to address complaints from residents living close to highways and motorists driving over textured surfaces.

The pavement surface plays a very important role in the propagation of noise from the tire/pavement contact area to the sideline receiver [Wayson 1998]. Surface texture and pavement type both play important roles and the absorption capacity of the pavement surface is extremely crucial. Absorption capacity depends on accessible porosity, specific flow resistance, a shape factor, and the layer thickness [Brite Euram 3415 1994]. An absorptive surface will reduce the horn effect and reduces the sound at the roadside because the sound energy is not as efficiently reflected [Wayson 1998]. Increased macrotexture, that will be described later, results in greater diffusion of the reflected sound wave. Thus, although surfaces with high macrotexture create more noise because of radial vibrations, at the same time this may also result in decreased propagation.

Significant efforts to address the issues of safety and tire/road noise of highway surfaces have been underway for several years both in the US and in Europe. These efforts have resulted in several new surface textures and types of materials that can be used in road construction. The activities in the US have mostly been concentrated in the area of surface texturing. In Europe, an emphasis has also been placed on development of new types of pavement materials and roadway surfaces; including toppings with rubberized matrix, two-layer construction, and porous cement concrete [Alfonso-Ledee et al. 2000].

Practically all of the noise measurements related to tire/road interaction reported in the literature were conducted on field pavements and were therefore always influenced by such parameters as air temperature, wind velocity, vehicle effects, or sound reflection effects. These factors make the interpretation of the noise data more difficult and do not aid in the understanding of fundamental mechanism of tire/pavement interaction. Such

understanding can offer potential benefits with respect to the redesign of tires and/or road surfaces to improve safety while reducing traffic noise.

Portland cement concrete (PCC) pavement is generally durable with good friction qualities, but tends to be noisier than asphalt pavements. Pavement texture can significantly influence the sound generated when a tire rolls over the road. More analysis and development is required to design a road surface that not only reduces overall tire/road noise sound levels, but that is also safe and durable. Open-graded asphalt and porous asphalt surfaces have also been tested in Europe. These types of pavements provide noise reductions of up to 8 dB [Sandberg 1999]. However, the noise reduction capabilities of these types of surfaces diminish with time.

2.5.1 Pavement Texture

Pavement texture is the dominant factor in determining wet pavement friction [Kuemmel 2000]. Prior to the recent attention researchers have given to tire/road noise, surface irregularities were divided into three ranges, microtexture, macrotexture, and unevenness. Tire/road noise research has lead to the introduction of a new range of irregularities, megatexture, which lies between macrotexture and unevenness.

The World Road Association's Permanent International Association of Road Congresses (PIARC) Technical Committee on Surface Characteristics has developed the following classification of surface irregularities as such: microtexture as <0.5 mm (0.02in), macrotexture as 0.5 mm – 50 mm (0.02 – 2 in), megatexture as 50 – 500 mm (2 – 200 in) and unevenness as 0.5 m – 50 m (1.6 ft – 164 ft) [Wayson 1998].

An International Standards Organization (ISO) working group investigated the relative importance of each of the ranges [Wayson 1998]. They found that microtexture is important for safety but it does not have a significant impact on tire/road noise generation. Similarly, the Belgian Road Research Center in Brussels has concluded that neither microtexture, nor unevenness, has any measurable affect on tire/road noise [Sandberg 1999]. Pavement unevenness can cause rattling of the payload of vehicles or induce secondary noises due to ground-borne vibrations in heavy traffic. However, both

macrotexture and megatexture play significant roles in noise generation and in safety [Wayson 1998].

A European state-of-the-art report [Brite Euram 3415, 1994] reports that low frequency noise is caused by tire vibrations and is a function of large wavelengths, or megatexture. Tire tread pattern is thought to control the medium frequencies. The microtexture amplitude has a decisive influence on surface friction, which must be maintained, but this is difficult to implement.

Macrotexture is most often thought of as a pavement with aggregate exposed on the surface but can also be produced by use of porous textures, tining, grooving, grinding, shot blasting or imprinting [Wayson 1998, Beringier and Alfonso-Ledee 1998]. Surface texturing that creates macrotexture allows for water removal but causes radial excitation of tires [Wayson 1998].

Megatexture in a pavement is responsible for radial vibrations and resonance phenomena inside the vehicle [Wayson 1998]. Megatexture can arise due to wear and fatigue of the surface [Sandberg 1999]. No specification to date has been proposed to quantify the amplitude of megatexture.

Texture is usually assessed through spectrum analysis of the road profile recorded by means of a laser distance sensor [Beringier and Alfonso-Ledee 1998]. Specifications for texture profilometers have been standardized in ISO 13473-1 [1997].

It is difficult to measure the megatexture in a porous surface due to the discontinuities, namely pores in the surface. Some researchers [von Meier et al. 1992] found that sound absorption alone cannot describe the relative noisiness of a pavement. They found that the effect of megatexture can interfere with sound absorption and possibly destroy some of the benefits. According to the Brite-Euram project report 3415 [1994], low frequency noise components (less than 1 kHz) are positively correlated with long wavelength texture components (greater than 10 mm) and high frequency noise components are negatively correlated with short wavelength texture components. The opposite effects of texture explain why the acoustic properties of a pavement cannot be predicted by a single value such as the sand patch depth [Beringier and Alfonso-Ledee 1998].

The type of vehicle would also dictate the cross-over frequency value, or the frequency that borders the high and low values. In the case of cars, this value is reported as 1000 Hz, while for trucks, it is reported as 500 Hz [Sandberg and Descornet 1980]. This difference mainly arises due to the difference in tread patterns between trucks and cars. Thus, it becomes all the more difficult to correctly decide the frequencies where noise has to be reduced. The ranges of texture and their most significant anticipated results are shown in Figure 2.5.1 [Wayson 1998].

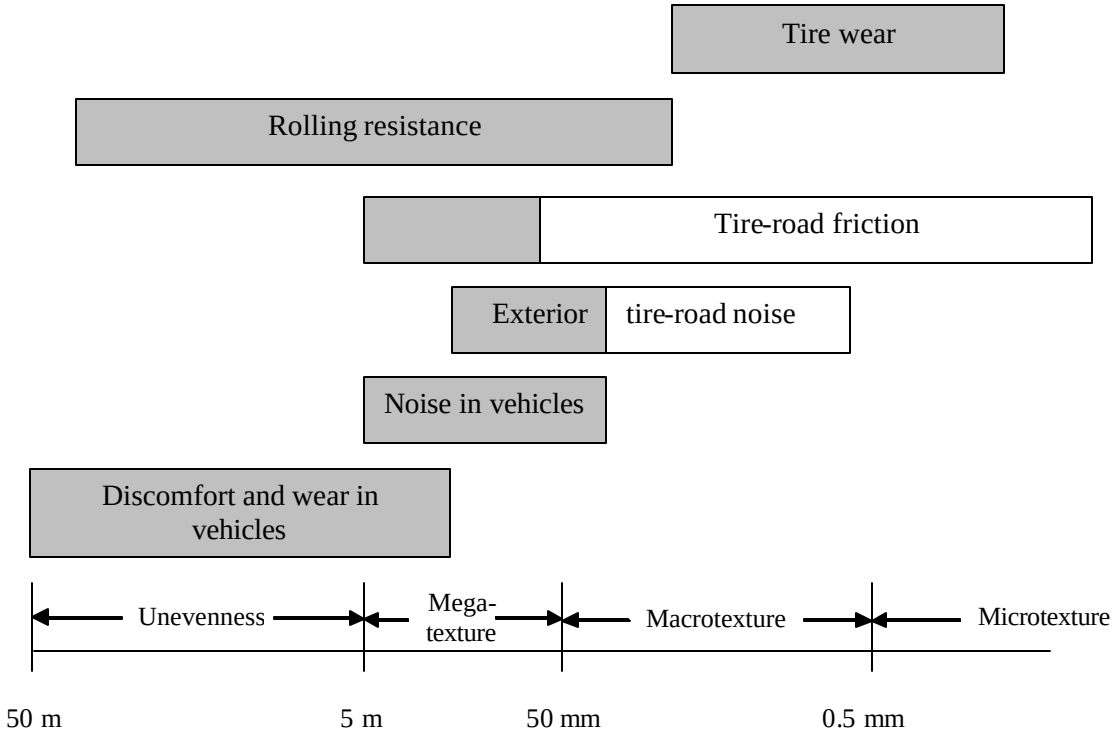

Figure 2.5.1 Ranges of texture and their most significant anticipated results [after Wayson 1998] (Unfavorable effects are shown as shaded boxes)

2.5.2 Internal Porosity

Porosity effectively reduces the air pumping effect, thereby reducing the tire noise [Sandberg and Ejsmont 2002, Brite Euram 3415 1994]. The amplifying effect of the acoustic horn is also reduced when the sound waves are allowed to attenuate through the pores in the surface layer of the material. Acoustic absorption occurs when sound waves pass through the series of pores in the material. Porosity may help reduce spraying of

water in rain conditions. However, it is unclear how the change in the surface texture created by the pore structure will affect the generation mechanisms of the noise.

2.5.3 Friction and Noise

Friction is a property of the tire-road interaction that is derived from a number of tire and road surface characteristics. Due to friction, the tire may transmit longitudinal and lateral forces between the road and the vehicle. Friction constitutes a key factor for safety and drivability. It was believed that coarse (and hence noisy) surfaces were necessary in order to ensure good skid resistance. However, it is now accepted that high friction and low noise are not conflicting requirements [PIARC 1991]. The road surface characteristics that determine friction are megatexture, macrotexture, microtexture, and the pavement interacting with the rubber of the tire. Megatexture and macrotexture can be measured directly but microtexture measurements are indirect, mainly from tire-road friction, using British Pendulum method [Sandberg and Ejsmont 2002].

The skid resistance of various types of road surfaces were calculated using sensor-measured texture depth (SMTD), obtained from laser profile devices [Phillips 1994]. It was concluded from this study that high levels of SMTD, implying good skid resistance, are associated with high levels of megatexture, and therefore high levels of tire-road noise. For porous surfaces, which retain the texture in the form of pores, the skid resistance was found to be higher, even without high levels of megatexture.

2.6 Types of Low Noise Road Surfaces

Sandberg [1999] defines a low noise road surface as one causing at least a 3 dB(A) lower noise than conventional surfaces. In most literature, conventional surface refers to a Dense Asphalt Concrete (DAC) with 11 – 16 mm maximum aggregate size.

A number of low noise road surfaces have been attempted in various countries, and the use of porous asphalt as a low noise road surface has become prevalent in many areas. The use of porous concrete is still in a trial stage. However, modification of

surface texture of concrete pavements by grinding or tining is commonly followed as a means of noise reduction.

Although the use of porous road surfaces dates back to very old times, the reasoning behind using the porous surface was only to provide drainage channels, and not noise reduction. The reduction of noise became a concern only after the development of high speed roadways through urban areas. Most literature relating field experience in the use of low noise road surfaces are about porous asphalt, or about concrete pavements with modified texture.

According to Sandberg [1999], the guidelines for a low noise road surface include:

- A wearing course with as high a voids content as possible from a durability point of view (> 20%, ideally 25 – 30%)
- Thickness of wearing course should be at least 40 mm, for absorbing even the low frequency noise
- Porosity should be such that clogging does not occur, and wide channels are avoided
- Megatexture, especially around wavelengths of 50 – 100 mm, should be avoided by using uniform, not so large aggregate packed close together
- Smooth macrotextures also should be avoided; macrostructure should be maximized at a wavelength of 2 – 6 mm for car tires and 4 - 8 mm for truck tires
- The chippings should ideally be 3 – 6 mm in size, with sharp edges

The following sections take a closer look at some of the low noise road surfaces.

2.6.1 Non-Porous Cement Concrete Surfaces

Conventional cement concrete pavements have higher friction and durability characteristics compared to asphalt pavement, but are noisier [Kuemmel 2000]. Noise reduction on regular cement concrete pavements is accomplished by surface texture modification techniques. These techniques include: grinding (primarily in the longitudinal direction), sawing, tining (both in longitudinal and transverse directions),

broom finish, and Astroturf drag finish. More work has been done on tining compared to the other methods. Tining on concrete surfaces could be either in a regular or a random fashion. The exposed aggregate technique has also been attempted for cement concrete surfaces.

Surface texturing for concrete pavements has been done for many years with the primary purpose of improving the skid resistance of pavements. As per the ACI 325 committee report, [1988] texturing of concrete pavements started in England in the early 1950s. The first grooving of concrete pavements was done on a number of airfield pavements in 1956. Burlap dragging and transverse and longitudinal grooving, using different types of machines and tools, were experimented with highway pavements in the USA in the 1960s and led to the optimization of surface texturing techniques Only in the recent past, the benefits of surface texturing in reducing traffic noise have caught the attention of researchers. The categories of pavement surface texture have been discussed already in section 2.5.1 Pavement Texture.

ACI committee 325 [1988] summarized the various types of texturing for concrete pavements as follows:

i. Artificial turf texture: Created by inverting an artificial turf and dragging on the surface
ii. Transverse tine structure: Created by a single pass of an artificial turf or burlap drag followed by a mechanically operated transverse (in a direction perpendicular to traffic movement) texturing device.
iii. Longitudinal tine texture: Process similar to the transverse tine, except tining is done in a direction parallel to the traffic movement
iv. Transverse broom texture: Obtained by using mechanically operated broom finishing device; striations are of the order of 1/16 to 1/8 in.
v. Longitudinal broom texture: Same as iv but in a direction parallel to traffic movement
vi. Transverse tine with longitudinal artificial turf: Transverse tine is preceded by the longitudinal artificial turf finish for high-speed highways

Transverse and longitudinal grooving can also be applied to hardened concrete pavements by carbide grinding, diamond grinding, sandblasting, or waterblasting. However, grooved concrete pavements generate traffic noise, and this has led, especially in Europe, to the use of alternatives such as chip-sprinkling, exposed aggregates, and porous concrete.

Chip-sprinkling involves the strewing of polish-resistant stones of a determined size evenly to the surface of a compacted and profiled fresh concrete and setting them in such a way that they slightly protrude from the surface, thus creating macrotexture [Fuchs 1981]. This technique, started in Belgium in the early 1970s, does not create unevenness and offers satisfactory comfort to the rider.

Exposed aggregate finish is achieved by washing off the top layer of mortar to expose the mineral structure of concrete. It requires the use of hard and polish-resistant aggregates [Descornet 1993]. This surface can be created either by watering and brushing, or by using a surface setting retarder and brushing off the top unset mortar.

A 25 – 35% traffic-related wear may be expected for surface textures in concrete pavements. This wear is higher in the first two or three years. As a result, it becomes essential to maintain the quality of the surface.

2.6.2 Porous Cement Concrete

The use of porous concrete road surfaces is still in a trial stage. Von Meier [1988] stated that the internal porosity of the cement paste in concrete may be favorable for noise reduction. However, the high megatexture of porous cement concrete makes for uncomfortable driving. Work related to porous cement concrete is ongoing in many countries. Most work is focused on improving the durability and mechanical strength of such concrete in order to make it a viable pavement material.

2.7 Modeling of Tire-Pavement Interaction

Researchers have attempted to model the influence of surface texture geometry on the stress and acoustic characteristics of the pavement. Clapp [1988] developed a model to approximate tire/road interaction behavior using a two dimensional contact theory. In this model, a rigid material is used to describe the pavement texture while a semi-elastic half-plane is used to describe the tire. The pressure distributions associated with the individual contact areas produce fluctuation forces that excite the tire structure. The location and length of an individual pressure distribution determines the contact length and its location on the road surface. This information enables the construction of a deformed profile of the rubber and the estimation of parameters such as depth of penetration, voids area, and ratio of actual to apparent contact on the surface of the pavement.

2.8 Chapter Conclusions

Tire-road noise is an important problem especially in populated areas. There have been numerous attempts to reduce noise generation with out compromising safety and ride quality. Most of these attempts have been are based on a change of surface texture to reduce noise generation without affecting the skid resistance especially on wet climates. This research is focused on understand and model the noise generated as the tire rolls over the pavement by means of the contact stress distribution between the tire and the concrete road and to understand the friction characteristics of these pavements. Some of the parameters covered in this research are: influence of the width, depth, and edge geometry of square tines and the influence of different texturing techniques. An attempt is made to correlate friction with the texture depth and noise.

CHAPTER 3 INFLUENCE OF SURFACE TEXTURE AND TINE GEOMETRY ON CONTACT STRESS AND NOISE GENERATION

This chapter describes the development and the use of a mathematical model to simulate the influence of the surface texture and tine geometry on noise generation caused by tire-road interaction. The noise was modeled by obtaining a contact stress distribution between the pavement and the tire. The tine geometries considered in this study included: square tine, round edges tine, and beveled tine. In addition, different surface textures were also evaluated. This chapter is divided into two sections: mathematical model of the stress and noise is described (section 3.1) and surface modeling of different tine geometries and textures (section 3.2).

3.1 Mathematical Model

This section describes the modeling and data reduction process for obtaining the frequency spectrum that is generated by a tire traveling on a pavement surface. Data reduction was performed to simplify the comparison between different noise spectra. The first step in generating the model was to obtain a static pressure distribution between the tire and the pavement. Once the pressure distribution was determined, it was transformed from a pressure profile in the contact patch area to pressures in a frequency domain. The frequency data was filtered with a $^1/_3$ octave filter for ease of comparison between the different surface textures and tine geometries.

3.1.1 Stress Distribution Modeling

Clapp [1988] developed a model to approximate tire-pavement interaction using a two dimensional contact theory. In this model (Figure 3.1.1); a rigid material is used to

represent the pavement while a semi-infinite elastic half plane is used to represent the tire. A uniform distributed load is applied to the rubber to force contact with the pavement. The pressure distributions associated with the individual contact areas produce forces that excite the tire structure. The location and length of an individual pressure distribution determines the contact length and its location on the road surface, the model considers the texture width equal to a single unit. This information enables the construction of a deformed profile of the tire rubber and the estimation of parameters such as depth of penetration and void area between the deformed tire rubber and the pavement.

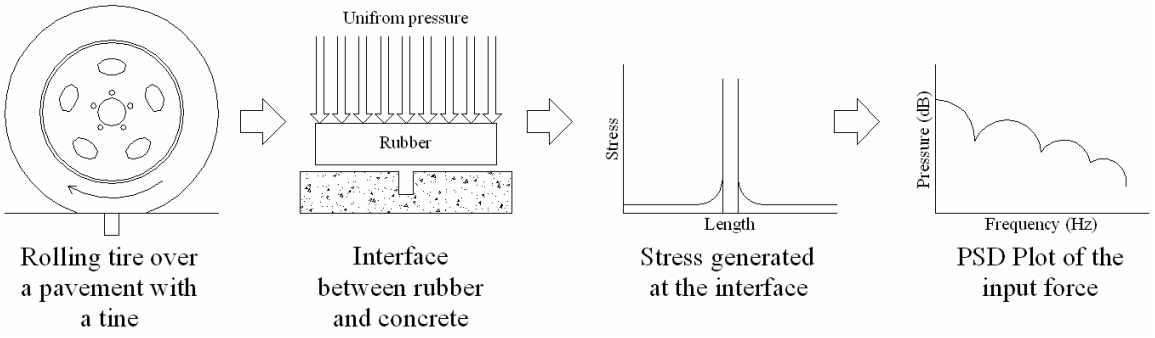

Figure 3.1.1 Noise generation approach

The model is based on analysis of individual contact areas that combine to form the total contact between the tire and a road surface. Figure 3.1.2 illustrates contact between a rigid road surface texture and an elastic rubber half-plane, thus simulating tire-pavement contact. The contact stress produced by a model of individual contact areas is mathematically described by using classical theory of elasticity. Contact pressure is approximated to the external pressure based on the model formulation and known input parameters.

The input parameters for the mathematical model are: pavement surface geometry (X, Y coordinates), tire pressure, modulus of elasticity of the tire, and Poisson's ratio of the tire. A program for calculating the stress distribution can be found in Appendix B.

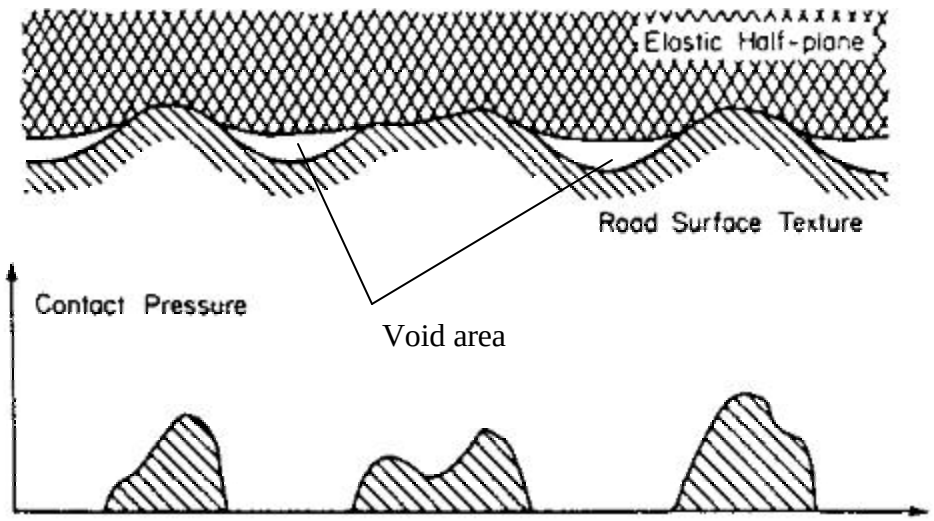

Figure 3.1.2 Profile of tire-pavement contact and associated contact pressure [Clapp 1988]

The computation process is summarized as follows:

i. Define the road profile, external loading pressure, contact length, and Young's modulus of the tire;
ii. Assume the tire is in full contact with the road surface, but the rubber does not penetrate into the voids on the pavement;
iii. Calculate the contact pressure for the length of the contact patch;
iv. Negative pressures indicate no contact, and are reset to zero. Areas of positive pressure determine the contact locations;
v. Compute the contact load and compare this with the external load; these loads are calculated by adding individual pressures with unit width and depth;
vi. Adjust the penetration depth of the tire rubber accordingly if the contact load is not equal to the external load;
vii. Go to step iii and reiterate the process until the average contact pressure is within 5 percent of the external pressure.

3.1.2 Pressure and Noise

As previously discussed, the mathematical model can predict the contact stress distribution between a hard pavement surface and the tire. The contact pressure fields can be transformed into a time-varying pressure by dividing the contact patch length by the vehicle speed to obtain a sampling frequency. At each point in the contact patch, there is pressure acting on the tire; a Fourier transformation can be applied using a previously determined sampling frequency to generate a power density spectrum to identify the frequency content of the stress distribution. The greater the pressures at the tire-pavement interface, the louder the noise generated. The spacing of these pressure events and the speed of the rolling tire influence the frequency at which the main events take place in the power spectrum.

3.1.3 Generation of the Power Density Spectrum

Noise generated by a tire rolling on a concrete surface is associated with different generation and propagation mechanisms. The purpose of this research is to identify the noise generating mechanisms resulting from the contact between a tire and a pavement and to minimize the noise by minimizing the stress generated on the tire-pavement interface.

Tire generated noise can be divided into three parts that influence the final noise output. These components include: Tire dynamics is mainly controlled by the vibration and speed of the tire. Acoustic radiation controlled by the shape and material properties of the tire. The input force describes the stress field that is generated by tire contact on the pavement.

A diagram showing a conceptual view of the three previously mentioned components that contribute to the noise generation is shown in Figure 3.1.3. Each of these components has a particular spectrum that influences the noise generated.

Radiation efficiency (spectrum shown in Figure 3.1.3a) can be described as the ratio of the average acoustic power radiated per unit area of a vibrating surface and the average acoustic power radiated per unit area of a piston that is vibrating with the same average mean square velocity at a particular frequency [Fahy 1985]. Radiation efficiency

is affected by the stiffness of the tire and flexural modes of deformation. It is a measure of how the tire emits sound at different frequencies. It is not affected by the speed of the tire.

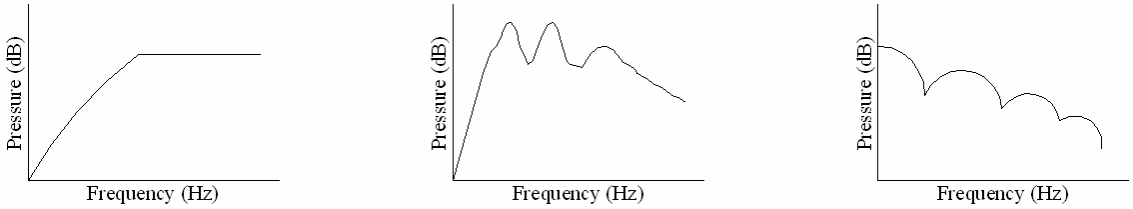

a) Acoustic radiation b) Tire dynamics c) input force

Figure 3.1.3 Power spectra influencing noise generation and propagation

A number of factors affect tire dynamics (spectrum shown in Figure 3.1.3b): tire construction, tire contact road characteristics, speed of the vehicle, and wheel load. A unique tire dynamics spectrum exists for any given tire at a certain inflation pressure, loading condition, and speed [Kim 2003].

The input force (spectrum shown in Figure 3.1.3c) is one part of the total noise that is generated by excitation of the tire rubber as it rolls over different geometries on the road surface. This excitation produces vibrations in the tire that are transferred to the air and produce the noise we hear. The excitations of the rubber can be described by the contact stress distribution generated between the tire rubber and the pavement; since the contact stress distribution obtained by modeling is static, it is necessary to apply a fast Fourier transformation (FFT) to simulate the dynamic behavior.

The stress distribution (shown in Figure 3.1.4) is different for each surface and will generate different frequencies and pressures on a pressure spectrum. The transformation from contact stresses to pressure spectrum has to take into account that there are two main stress events as a tire rolls over a tine on a concrete road. These events are at the beginning and at the end of contact patch of the tire and will have different sound pressure intensities depending on the position of the microphone that is recording them. If the microphone is located at the front side of the contact patch, the second event will have a lower magnitude.

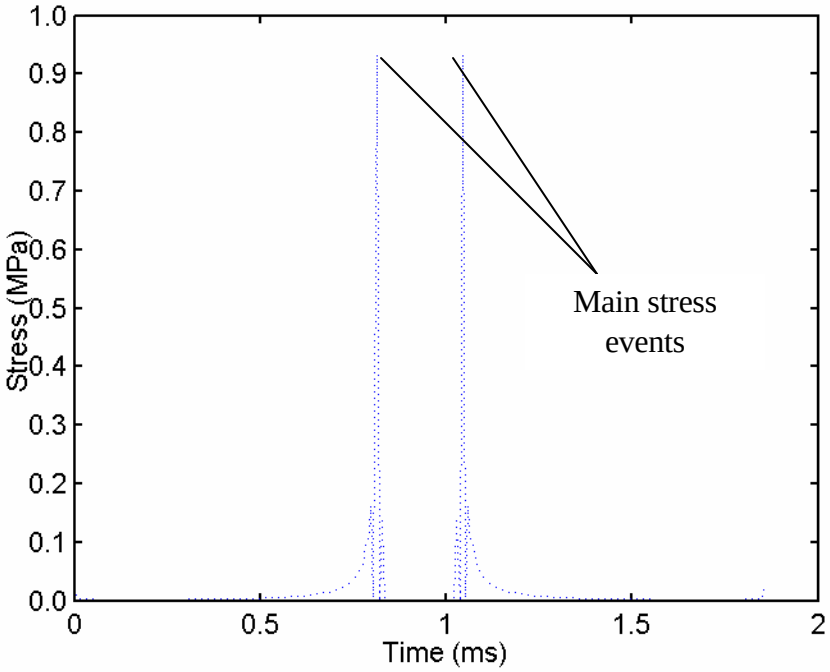

Figure 3.1.4 Typical stress distribution for a square tine in time domain

To take into account the existence of two events is necessary to change the contact stress distribution by adding a second, mirror event scaled down at a distance equal to the length of the patch area as shown in Figure 3.1.5. In our experiments, the registration of these events had a time difference of 0.0042 s, and since the speed of the rolling tire was 13.4 m/s, the distance of these events will be 5.63 cm. The scaling factor for the second event was 0.443, and was calculated by averaging the difference of intensities in the collected data. The FFT of the stress distribution with the two events will be better approach in describing the input force spectrum; this is because if only one event is present the modulation effect of the main frequency will be controlled by the distance between the edges of the tine rather than by the size of the tire patch area. If the frequency modulation is controlled by the size of the tine, small changes on tine width will have larger effects on the spectrum and this was not confirmed during experiment.

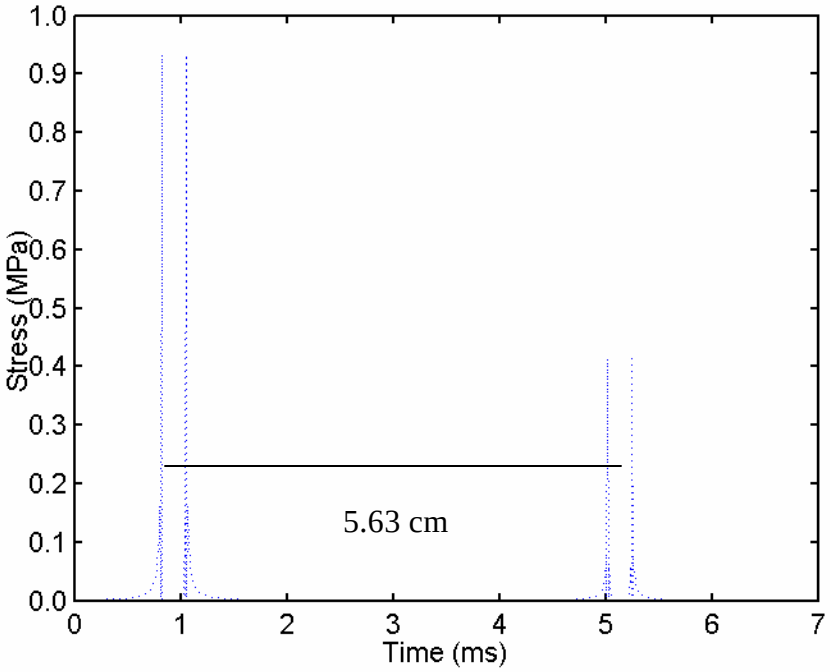

Figure 3.1.5 Conceptual view of the stress distribution for square tines separated by 5.63 cm; 0.0042 s of time separation between the events at a speed of 13.41 m/s

As previously described, the input force spectrum is obtained by applying a FFT to the static pressure distribution of two mirror events separated by the length of the contact patch. To compare efficiently the input force to the final noise output is necessary to scale and filter the noise spectrum, and to calculate the overall band level. One of the scaling procedures implemented was "A" weighting. "A" weighting is a common procedure used in sound recollection; it reduces the sensitivity of microphones in the lower and higher frequencies, in a way that roughly mimics human ear response. The human ear is most sensitive to sounds at mid frequencies (500 to 4,000 Hz) and is progressively less sensitive to sound at frequencies above and below this range. A graph showing the frequency response for "A" weighting is shown in Figure 3.1.6, (the scaling is the same as in the next power spectrum plots for ease of comparison). The original data are plotted as the dashed red line and the "A" weighted as the solid black line. A table and a Matlab program for applying "A" weighting can be found in Appendix A.

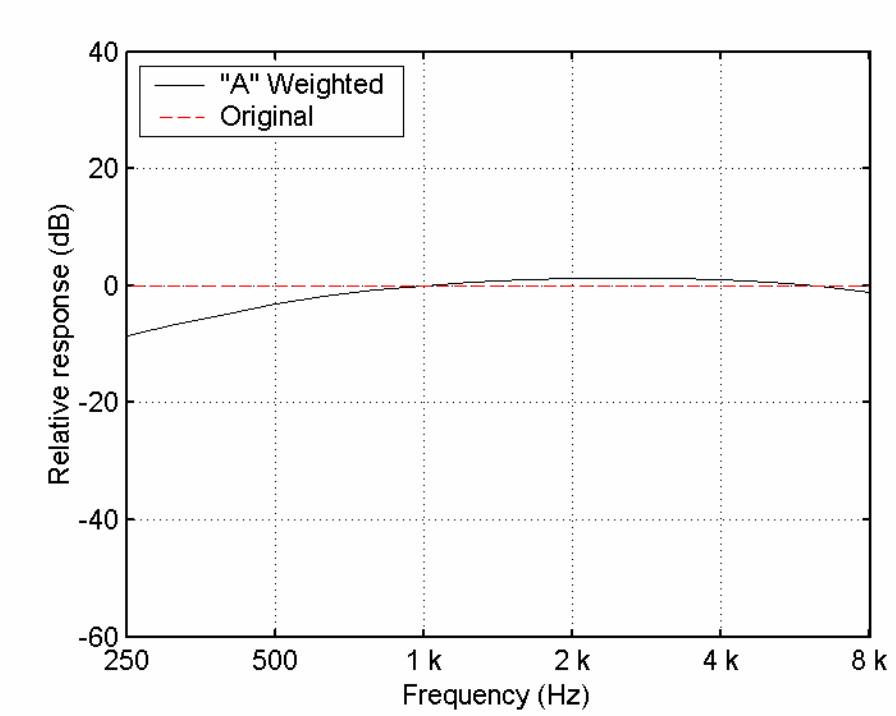

Figure 3.1.6 Frequency response for "A" weighting

The filtering procedure used to simplify the comparison between frequency spectra is based on using a $^1/_3$ octave narrow band analyzer. The $^1/_3$ octave analyzer is perhaps the most widely used amongst the available analyzers. As the name suggests, this method splits the octave into three parts. The application of the filter is done by adding the sound pressures over a range of frequencies. This range of frequencies changes in small increments for low frequencies and becomes greater as frequency increases, meaning that the filter adds more data on high frequencies than on low frequencies. The frequency distribution after applying the $^1/_3$ octave filter becomes linear on a logarithmic scale. The addition of the sound levels has to be done in non-scaled pressure units (Pascal) and not in decibels since decibels refer to the human audible scale. A table with $^1/_3$ octave bands and a Matlab program to apply the filter can be found in Appendix A.

The overall band level of sound can be calculated by the addition of pressures in a given frequency range; as before, the addition has to be done in non-scaled pressure units after the $^1/_3$ octave band filter has been applied. A program can be found in an Appendix A.

In summary, the procedure to obtain the input force frequency spectrum is:

i. Obtain a contact stress distribution for the surface in question.
ii. Transform the single event stress distribution to a two event using a mirror image of the stress with a separation equal to the length of the contact patch area.
iii. Apply a fast Fourier transformation to the contact stresses taking into account the sampling frequency.
iv. Apply "A" weighting to the power spectrum.
v. Apply a $^1/_3$ octave filter to the frequency spectrum.
vi. Calculate the overall sound pressure level.

The output noise pressure is generated by the multiplication of the three spectra shown in Figure 3.1.3, but of these, only the input force is influenced by the surface texture of the road. The other two spectra will be constant for any given type of tire at any given speed; therefore minimizing the input force spectrum will minimize the final pressure spectrum. If the tire dynamics and radiation efficiency spectra are multiplied a transfer function can be develop to transform an input force spectrum to the final noise power spectrum. However, since modeling of tire dynamics and radiation efficiency is quite complicated, in this research the transfer function was calculated by dividing the experimentally measured noise by the input force spectrum obtained from modeling. This transfer function was calculated for each of the types of tines and will be compared for each of the cases where experimental data was obtained.

3.2 Modeling of Various Surfaces Textures and Tine Geometries

The stress distribution model was used to describe the stress and ultimately noise generated by different surface textures and various geometries of tining patterns. Modeling of these surfaces will help understand the implications of varying size, shape,

and depth of tines on stress generated. A stress distribution was obtained for each surface and was related to the noise that the tire will emit while running over the surfaces.

A set of five tine geometries to be analyzed was selected. The selection was done in a way that modeling of different essential characteristics was considered, like width and depth of the tine, and also modeling of special geometries that could reduce the amount of noise generated. Samples of the changing patterns in the modeling of geometries are given in Table 3.2.1; all of these different geometries were modeled for a length of 25 mm.

Table 3.2.1 Summary of geometries and textures used in the models

	Type of variation	Section geometry	Approach
Modeled and evaluated on the TPTA	Width of the tine	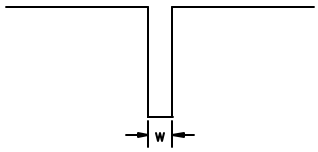	Varying tine width evaluates the influence of the width on peak stresses between the tire and the pavement.
	Depth of the tine	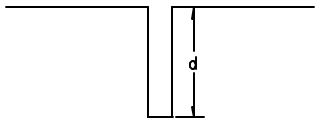	Varying tine depths helps detect up to which point the depth is an influence on the stress distribution.
	Curvature on the edge of the tine	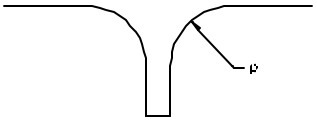	Varying ?, helps to reduce the stress concentration at the edges of the tine by distributing it over a larger area.
	Bevel on the edge of the tine	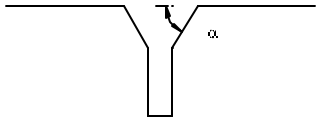	Varying a, helps to reduce the stress concentration by distributing the stress in more than two edges.
Modeled only	Depth of uniform texture	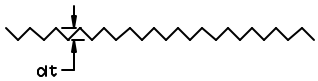	Varying texture depth to detect its influence on stress generation in an artificial triangular scenario.
	Height of uniform texture	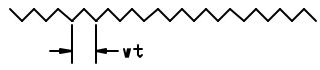	Varying texture width to detect its influences on the stress generation on surfaces.
	Height of random texture	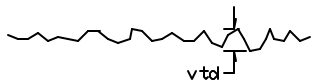	Varying texture depth to asses its influence in a realistic random scenario similar to real textures.

3.2.1 Variation of Tine Width

The tine width was varied to asses its influence on stress generation. Tine width varied between 0.2 mm and 6 mm in 0.2 mm increments, for a uniform depth of 10 mm. Figure 3.2.1 shows the schematic of the width variation.

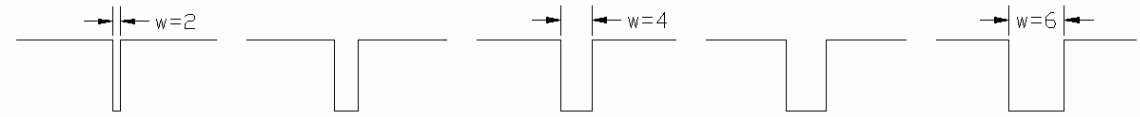

Figure 3.2.1 Schematic of width variation with constant depth of 10 mm

Tine width influence on stress generation is shown in Figure 3.2.2. The observed variation of the peak stress levels is due to the precision of the iterative process in load computation that was set to 5%; had the precision been set to a smaller value, the data points would have converge near the trend. Due to the considerable amount of computational time needed to obtain the exact values the peak stress, the values of stress corresponding to the trend line were used in the simulation presented in this document. In general, it can be observed that, the peak stresses tend to decrease as the tine width increases.

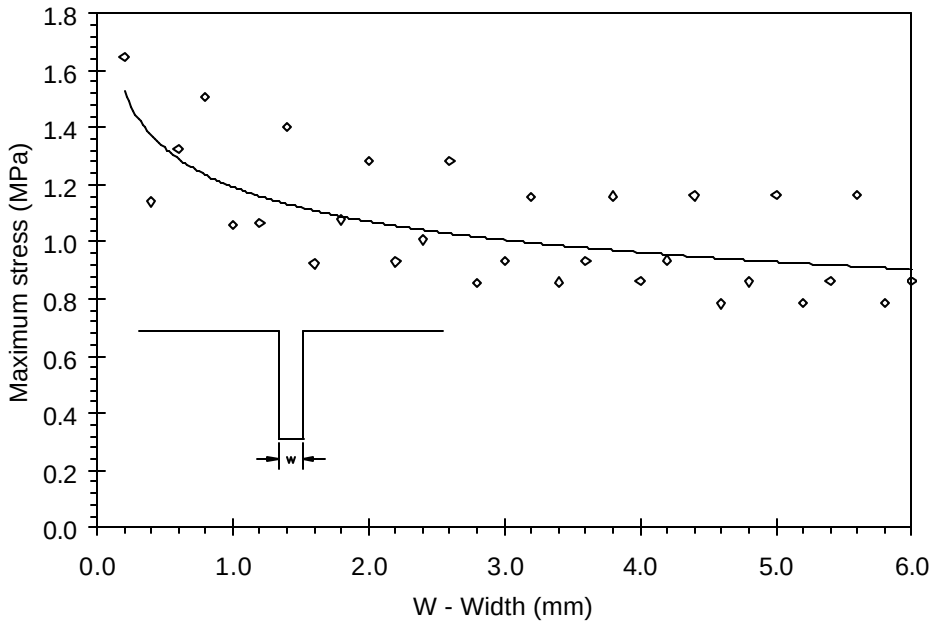

Figure 3.2.2 Influence of tine width on stress generated in 10mm deep tine with variable width (from 0.2 to 6mm in .2mm increments)

The influence of the tine width on the penetration of the rubber into the tine is shown in Figure 3.2.3; there is less penetration as the width of the tine is incremented. A relationship between the intensity of the stress and the deformation of the rubber can be seen by comparing both graphs. In general, reduced stress results in lower penetration.

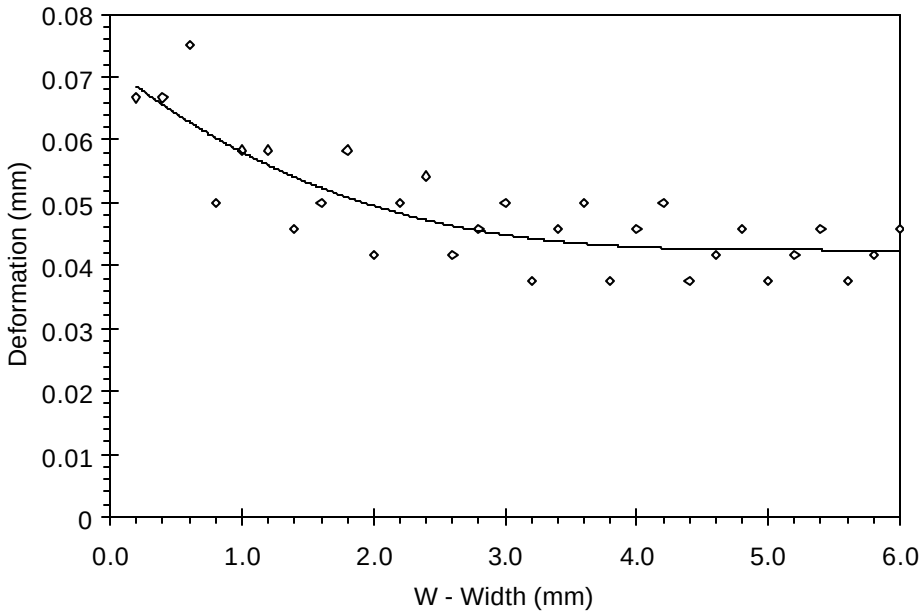

Figure 3.2.3 Influence of tine width on deformation of the rubber for 10 mm tine depth (with varing width from 0.2 to 6 mm in .2 mm increments

A deformed shape of the rubber and stress distribution for a single 3 mm wide and 10 mm deep tine is shown in Figure 3.2.4. The stress distribution (dotted blue) concentrates at the edges of the tine reaching a peak value of 0.93 MPa; the stress concentration is due to an abrupt change in geometry on the contact surface. The penetration of the rubber (dashed red) has a value of approximately 0.05 mm. The tire rubber penetration into the tine influences the air pumping noise generating mechanism; however, this has not been taken into account when calculating the power spectrum.

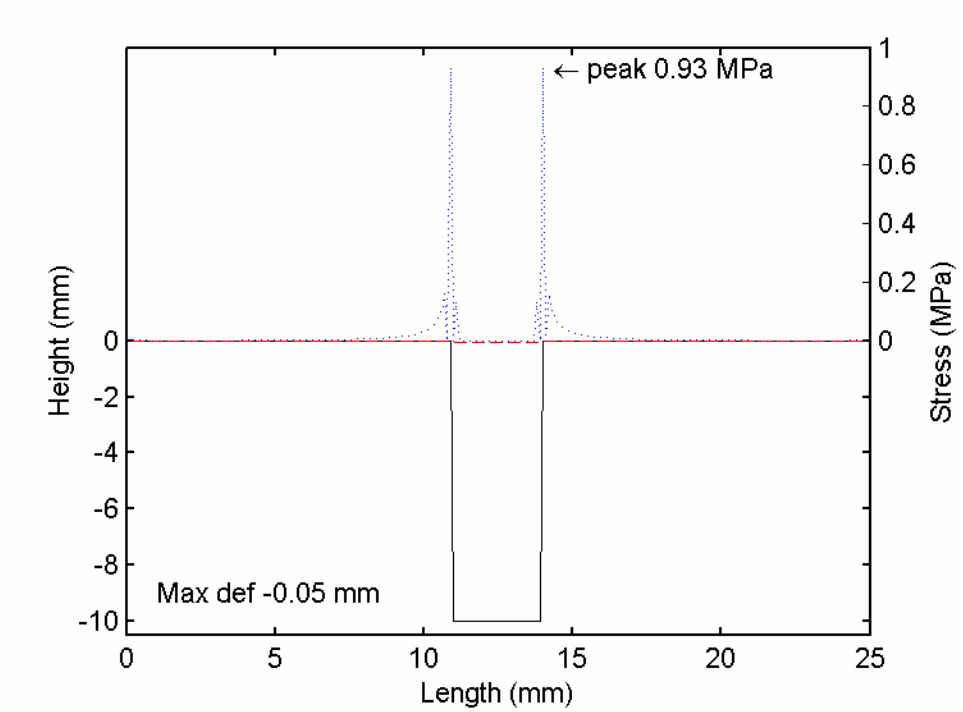

Figure 3.2.4 Geometry (solid), Stress distribution (dotted), and deformation (dashed) for a single square tine having 3mm width and 10mm depth.

The power density spectrum for this tine is shown in Figure 3.2.5; the black solid line is the power spectrum after "A" weighting, the dashed red line is the power spectrum before "A" weighting, and the solid blue line is the power spectrum after applying a $^1/_3$ octave filter. As indicated by the power spectrum, the intensity of the pressure has a tendency to fluctuate at a value of 150 dB for frequencies below 2 kHz. After this, frequency modulation waves are more predominant giving a higher pressure of 160 dB. The overall band level for this tine is 164.91 dB.

As the width of the tine changes, the PSD shifts the frequency at which the main pressure is located. Figure 3.2.6 shows the PSD of a tine with a 2 mm width and 10 mm depth. Comparing Figure 3.2.5 and Figure 3.2.6, it can be seen that there is an increment of 2 to 3 dB at pressure levels below 2 kHz for the 2 mm wide tine. There is also some shifting in the modulation of the main events due to the width of the tine. Equation 3.1 shows a formula to obtain frequency at which the spectrum presents its main wave, the rest of the waves being modulations of the first wave. The overall band level for the 2 mm case is 166.91 dB; this is an increment in comparison to the 3 mm case, and this

increment agrees with the increment of peak stress levels shown in Figure 3.2.2 as the tine width becomes smaller.

$$F = \frac{V}{D} \tag{3.1}$$

where:

F – Frequency (Hz)

V – Speed (m/s)

D – Distance between main events in the stress (m)

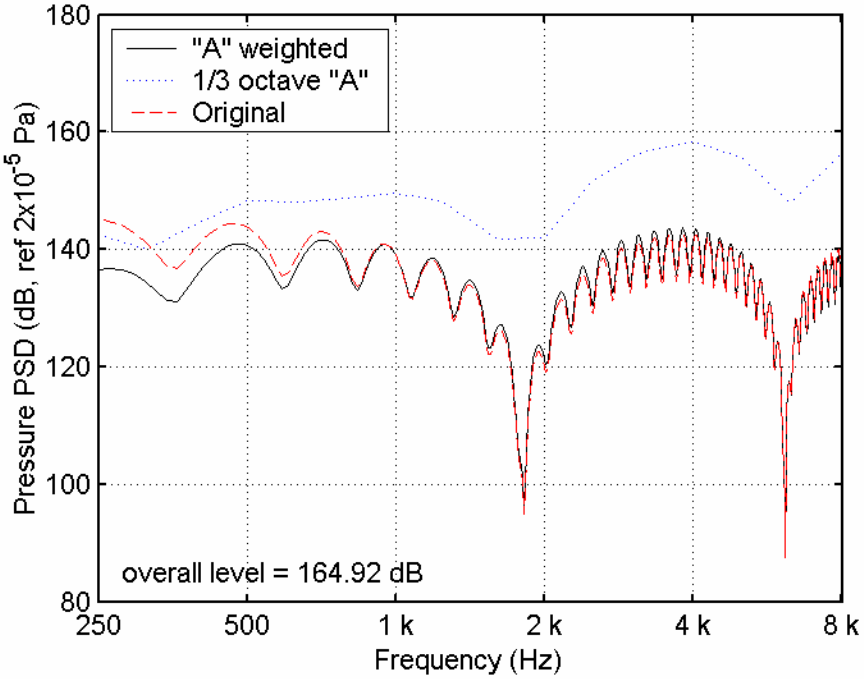

Figure 3.2.5 Frequency spectrum of the stress distribution for a square tine with 3 mm width and 10 mm depth at a speed of 13.41 m/s of a

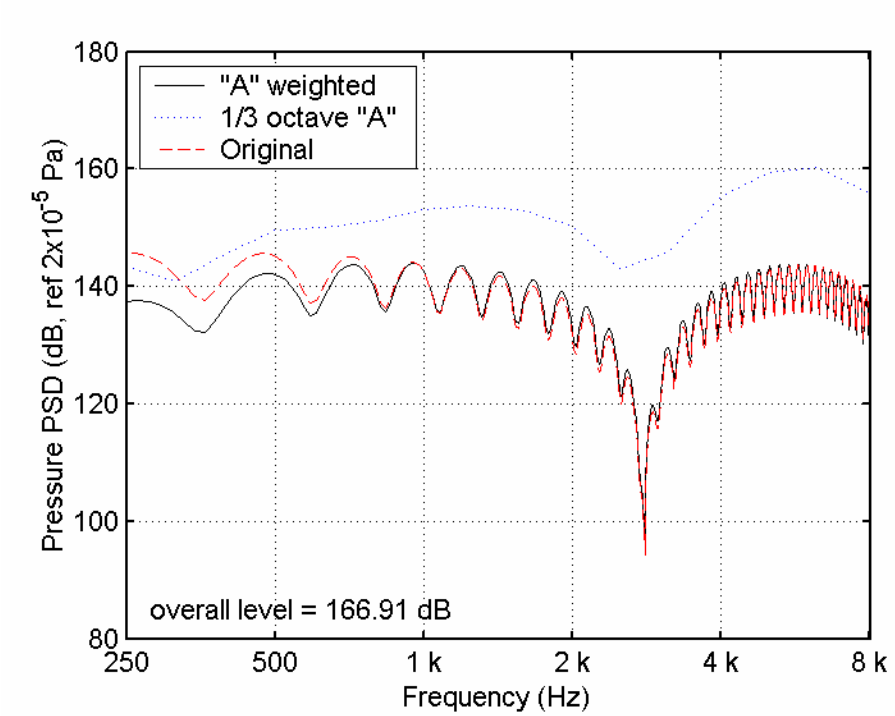

Figure 3.2.6 Frequency spectrum of the stress distribution for a square tine with 2 mm width and 10 mm depth at a speed of 13.41 m/s of a

3.2.2 Variation of Tine Depth

Learning that the peak stress generated by the tine is not influenced by the depth may change the design of tines to deeper ones; that will improve drainage and skid resistance on pavements.

The tine depth was varied to assess its influence on the surface stress generation. The penetration of the rubber into the tine was also computed. The variation of tine depth was investigated for a 3 mm width. The depth was varied from 0 mm to 1 mm in increments of 0.1 mm. A sample pattern of depth variation is shown in Figure 3.2.7.

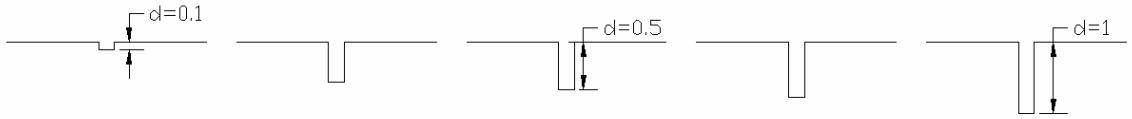

Figure 3.2.7 Schematic of tine depth variation

The influence of depth on stress generation is shown in Figure 3.2.8. Here the peak stress reaches a maximum level of 1 MPa at a certain depth. This maximum stress

level is related to a point at which the deformed rubber stops penetrating into the floor of the tine as the tine depth is incremented.

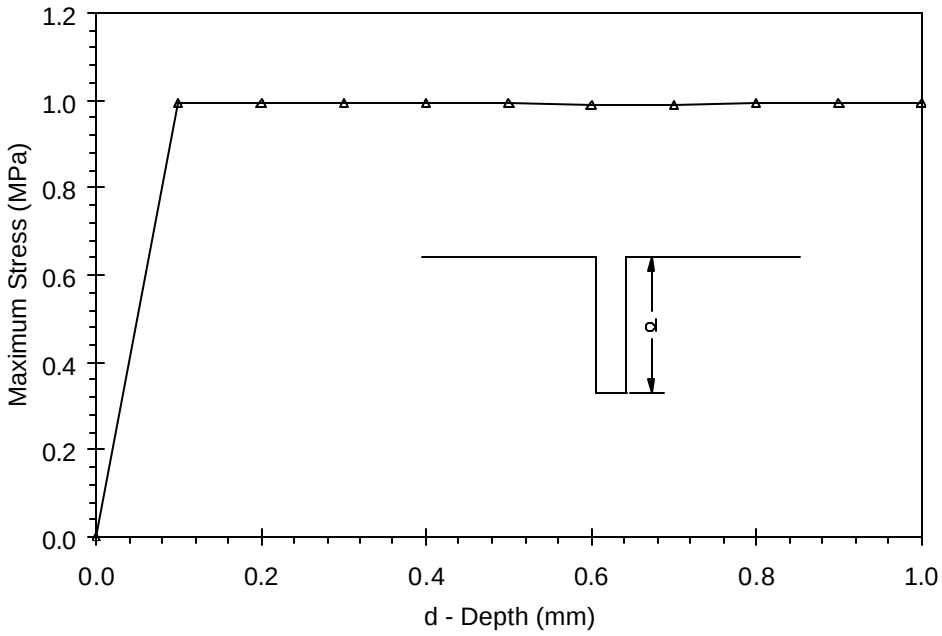

Figure 3.2.8 Peak stresses for different tine depths from 0 to 1.0 mm at 0.1 mm increments for a 3 mm width tine

The typical stress distribution for a tine with shallow depth is shown in Figure 3.2.9 for a single square tine 3 mm wide and 0.5 mm deep. The peak stress is 0.99 MPa and at this resolution, it does not seem to be affected by the depth of the tine. The penetration of the rubber into the tine is 0.053 mm. From these results, it can be concluded that the stress will be constant for any depth above this value. In other words from the point of view of stress and noise generated in the tine the depth of the tine does not need to be grater that 0.053mm however, other reasons such as: water drainage, skid resistance, and air pumping may lead to a need for a deeper tine.

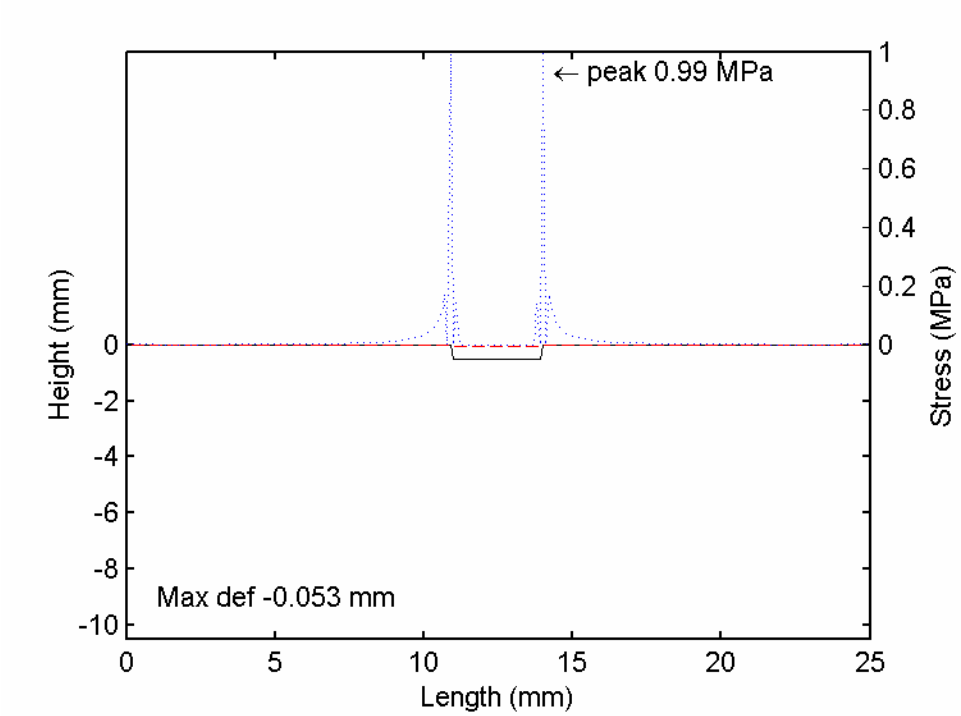

Figure 3.2.9 Geometry (solid), stress distribution (dotted), and deformed shape (dashed) for a single square tine with 3mm width tine 0.5mm depth

The power density spectrum for a 3mm wide and 0.5mm deep square tine is shown in Figure 3.2.10; the black solid line represents the power spectrum after "A" weighting, the dashed red line represents the power spectrum before "A" weighting, and the solid blue line represents the power spectrum after applying a $^1/_3$ octave filter. This power density spectrum is similar to the one obtained for a 10 mm deep tine. The similarity is the result of the same spacing and similar magnitude of the main contact stresses. The intensity of the pressure has a tendency to fluctuate at about 152 dB for frequencies below 2 kHz. After that, the frequency modulation waves are more predominant giving a higher pressure of 159 dB. The overall band level for this tine is 166.47 dB; this value is almost the same as the one obtained for 10 mm deep tine. The difference in the overall band level and in the levels on the spectrum is due to the change in the peak stress level from 0.93 MPa for the 10mm deep tine to 0.99 MPa for the 0.5 mm deep tine. The difference in stress level may also be related to the precision of the iterative process that was set to 5%.

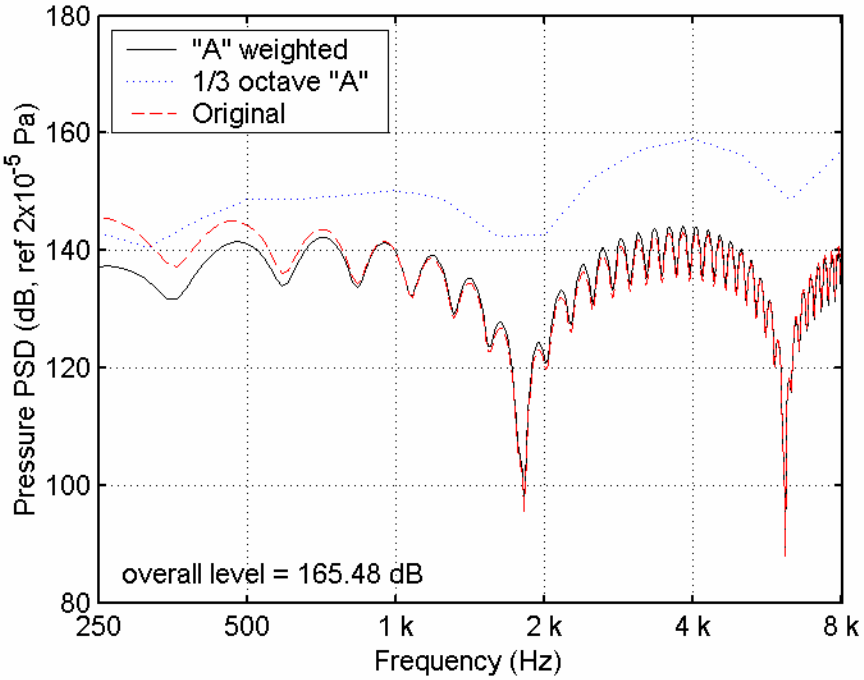

Figure 3.2.10 Frequency spectrum of the stress distribution for a speed of 13.41 m/s of a square tine with 3 mm width and 0.5 mm depth

3.2.3 Tines with Rounded Edge

The edges of the tines were rounded to investigate how removing the sharp edge affects the stress concentration. The implementation of the rounded edges was done gradually to analyze at which point curvature is optimal. The modeling started with a standard rectangular tine and then quarter circles were introduced in the edges. The variation of the circle geometry was done by changing the radius, starting from 0.0 mm radius (square edge), and incrementing 0.1 mm each time to the maximum value equal to the depth of the tine (10.0 mm). Figure 3.2.11 shows how the geometry variation was implemented.

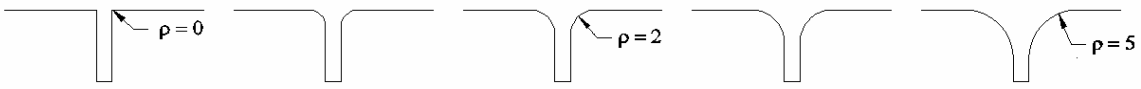

Figure 3.2.11 Schematic of the changing pattern of tines with rounded edge

The simulations for rounded tines were performed at tine widths of 2, 3, 4, and 5 mm. The results of the analysis are displayed in Figure 3.2.12. The peak stress at the

tine does not appear to be influenced significantly by the width of the tine after a radius of 1.7 mm. The peak stress reaches a constant value of approximately 0.15 MPa after the radius reached 6 mm.

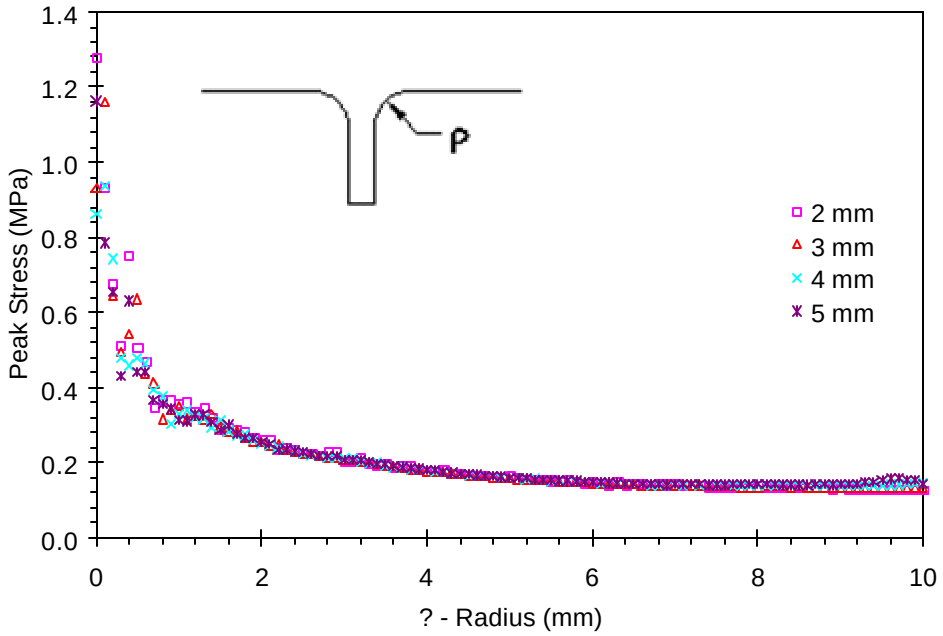

Figure 3.2.12 Peak stress in tines with rounded edge for tines 2, 3, 4, and 5 mm wide and 10 mm deep. The radius varied from 0 to 10 mm with 0.1 mm increments

The typical stress distribution for a rounded edge tine with 3 mm radius is shown in Figure 3.2.13 this figure shows how the stress was distributed over a larger area helping reduce the stress consentration at the edge of the tine. The stress reduction lowers the peak stress from 0.93 MPa for the suaqred tine to 0.20 MPa for the rounded edge tine with a 3 mm radius.

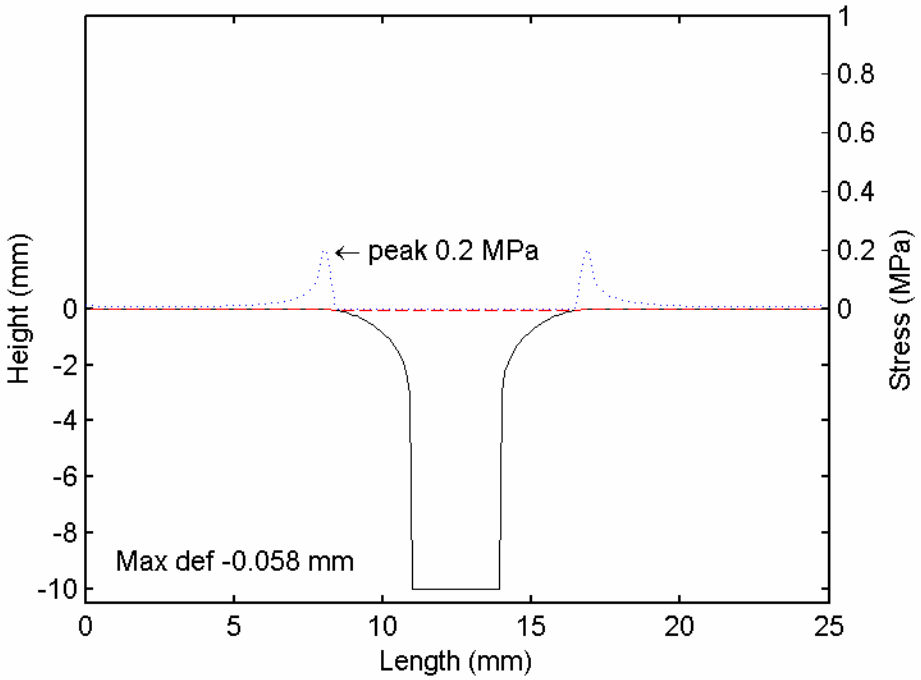

Figure 3.2.13 Geometry (solid), stress distribution (dotted), and rubber deformation (dashed) for tines with rounded edges 3 mm radius and 10 mm depth

The PSD plot of the rounded edge tines is shown in Figure 3.2.14. Comparing this spectrum to the one obtained for the square tine (Figure 3.2.5), it can be seen that there is a considerable reduction in the pressure on the tire rubber at frequencies between 250 Hz and 1 kHz (drop from 150 to 135 dBA). It can be concluded that this decrease is due to the rounding of the edges of the tine. In addition, a decrease in the size of the wave modulation (from 4000 to 1800 Hz) was observed, due to the increment in the distance between the centers of the two primary stress concentrations that were shifted by the rounding of the edges. The overall noise level was reduced from 164.91 dB for the square tine to 162.02 dB for the rounded edge tine.

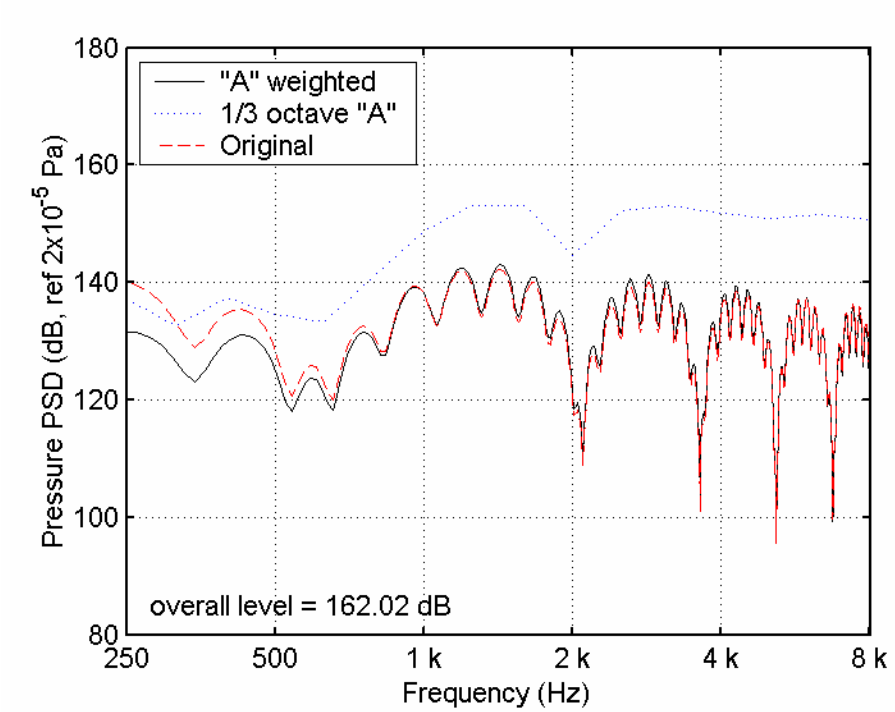

Figure 3.2.14 Frequency spectrum of the stress distribution for a speed of 13.41 m/s of a tine with 3 mm width, 10 mm depth, and rounded edges 3 mm radius

Figure 3.2.15 shows a comparison between the PSD spectra for tines with rounded edges for radius of 0, 1, 2, 3, and 4 mm. The tine with 0 mm radius can be interpreted as a square tine. As it is shown, a variation on the edge radius changes the location of the main stress concentrations resulting in a change on the modulation frequency.

The penetration of the rubber into the tine is also an important aspect of the analysis as it is related to air-pumping generation mechanism. The influence of the radius of the tine edge on the penetration of the rubber is shown in Figure 3.2.16. Here the influence of the width of the tine is observed, the bigger the tine the lesser the penetration of the rubber for a small radius. As the radius is incremented, the effect of tine width becomes less significant. As the radius increases, the penetration of the rubber increases from 0.05 to 0.058 mm by adding the 3mm radius to the edge of the tine. The tendency of having a lower stress related to higher deformation is also shown in this case.

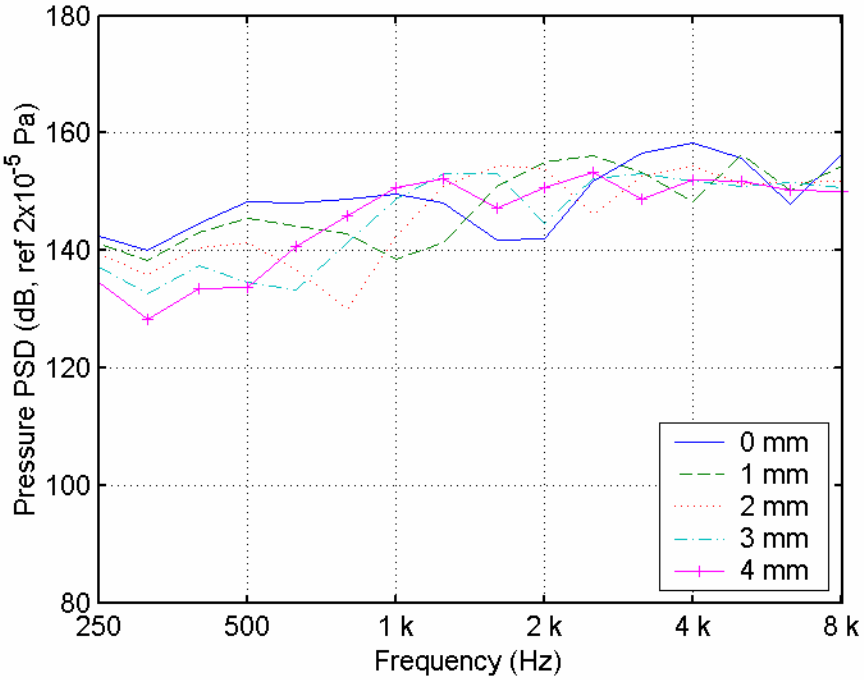

Figure 3.2.15 PSD plot for rounded edge tine with radius of 0, 1, 2, 3, and 4 mm and constant width of 3 mm

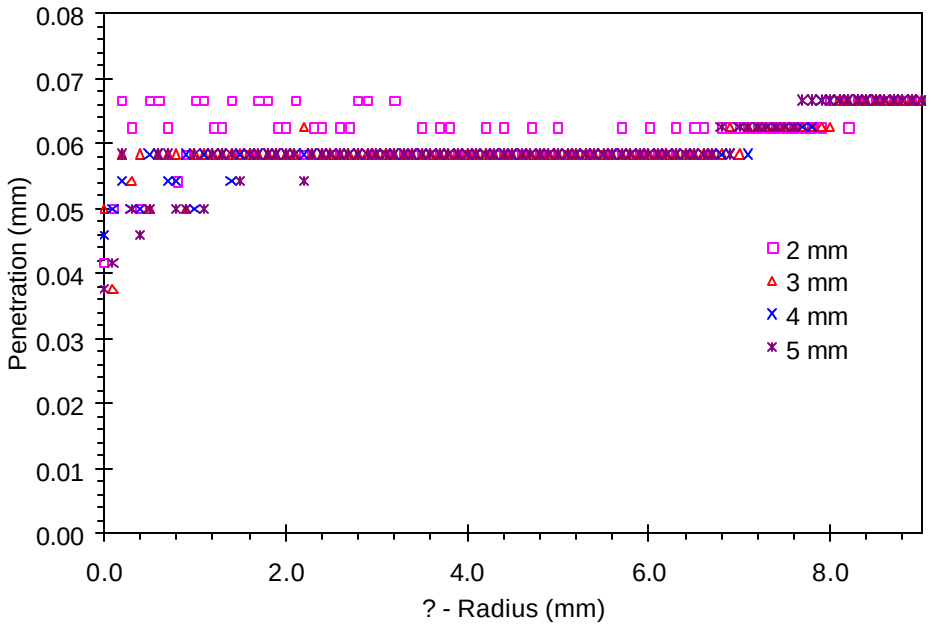

Figure 3.2.16 Maximum penetration of the rubber for tines with rounded edges; for widths of 2, 3, 4, and 5 mm and 10 mm depth. The radius was varied from 0 to 9 mm at 0.1 mm increments

3.2.4 Tines with Beveled Edge

The initial entry angle of a beveled type of tine was varied to assess its influence on the maximum stress and the maximum deformation of the rubber. The tines with widths of 2, 3, and 4 mm were analyzed. For each width, the entry angle was changed from 0° to 45° at the increments of 1°. A sample variation of the geometry of the tines is shown in Figure 3.2.17.

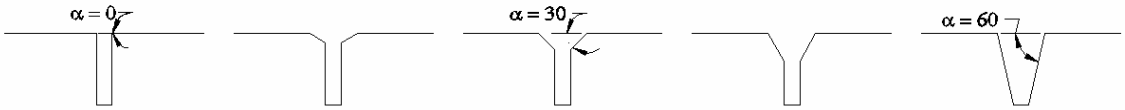

Figure 3.2.17 Schematic of changing pattern for tines with different entry angle

The influence of the entry angle on stress is shown in Figure 3.2.18. Two groups of data are shown: one with the peak stress diminishing to a certain point (M) and second with the peak stress increasing (E). At low entry angles the tine looks like a square tine and the stress distribution was similar having the two main stresses concentrated at the edges of the tine this range is marked by the (M) area on the graph. At higher entry angles, the stress distribution changes the location at which the main stresses are concentrated, the stress concentrations are now at the points of change of slope marked by (E) on the graph. The influence of the angle change on the peak stress stops at 25° for the three different widths.

The behavior of the rubber at low angle tines implies that the tire rubber does not deform much and that the high stress will be located in the inner part of the tine (M) where the tire suffers higher deformation and stresses, as shown in Figure 3.2.19. In this case, the stress concentrations are in four points instead of two in comparison with a square tine. The stresses at the center of the tine are higher than at the outer edges. The stress at the center points for a 1° angle is 0.64319 MPa and in the outer part is 0.1 MPa; the maximum rubber deformation for this angle is 0.092 mm. The peak stress is considerably less than that observed for a square tine. The reduction of the peak stress happens because some of the stress from the middle edges of the tine is taken by the outer edges of the tine.

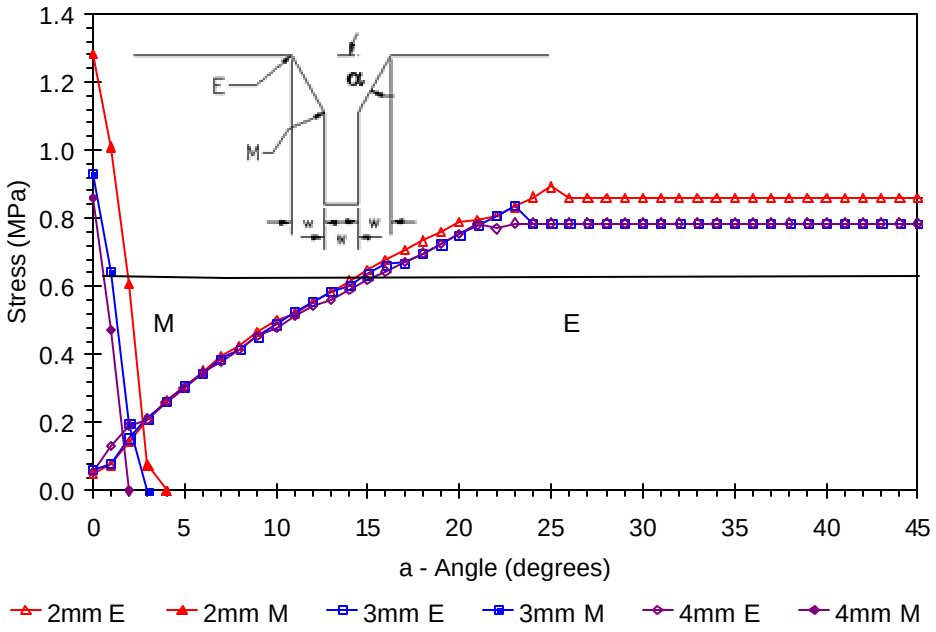

Figure 3.2.18 Peak stresses for bevel tines for varying entry angle. Tine widths of 2, 3, and 4mm, tine depth of 10mm, entry angle varying from 0° to 45°

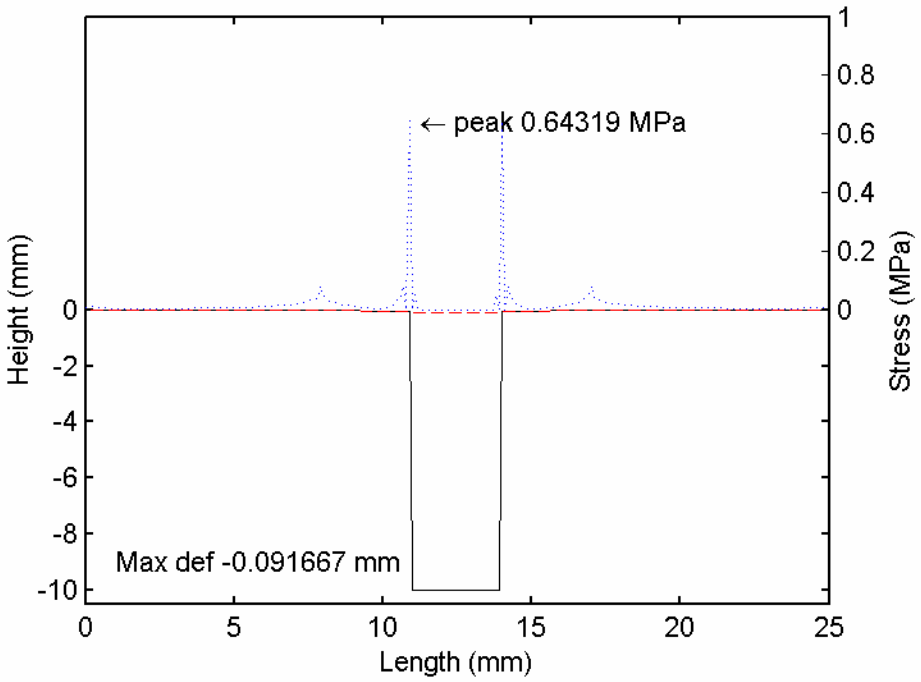

Figure 3.2.19 Geometry (solid), stress distribution (dotted), and rubber deformation (dashed) for 3 mm wide tines, with entry angle of 1° and 10 mm depth

Figure 3.2.20 shows the PSD plot for bevel tine having a 1° angle and 3 mm width. The pressures for frequencies below 1 kHz are lower than 135 dB, lower than the 150 dB for the square tine without the bevels. The overall sound level is 160.70 dB this level is lower than the one on the rounded edge tine that was 162.01 dB. The modulation effect for this is 3.8 kHz.

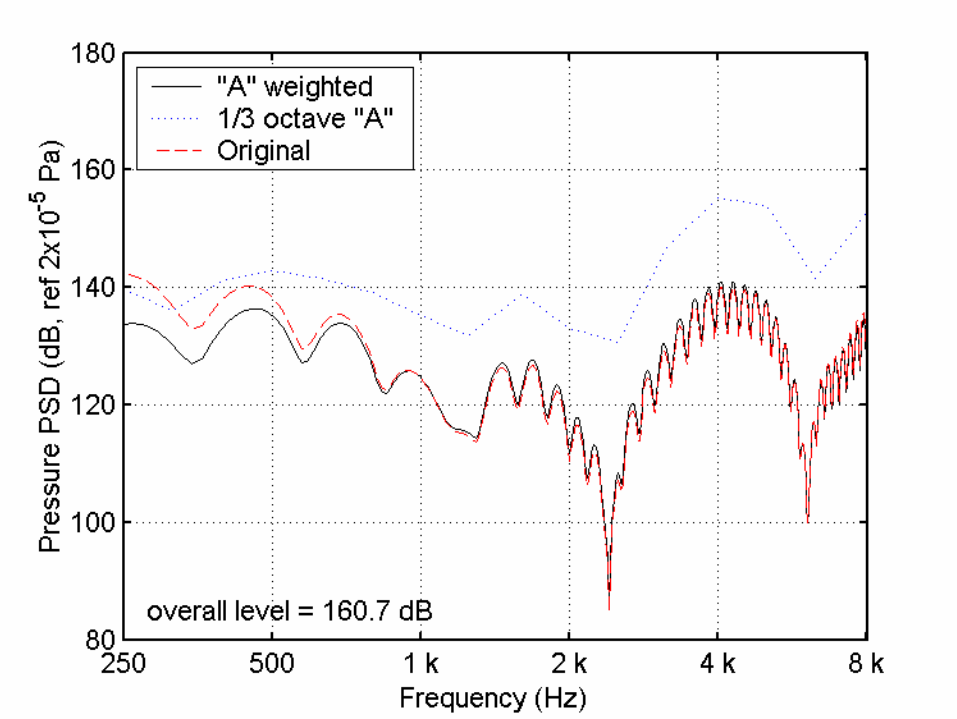

Figure 3.2.20 Frequency spectrum of the stress distribution for a speed of 13.41 m/s for a tine with 3 mm width, 10mm depth, and entry angle of 1°

At a larger angle, higher stresses concentrate in the initial part of the tine (E) and the middle part of the tine does not generate stresses, as shown in Figure 3.2.21. In this case, the rubber does not deform enough to penetrate into the middle part of the tine because there is a difference of height between the inner and the outer edges of the tine. The peak stress for a 10° angle is 0.48 MPa this is lower than 0.64 MPa for the 1° angle because it is distributed over a larger area of the surface of the tine. The maximum deformation of the rubber is 0.058 mm, smaller than the 1° bevel. This shows that there is a tendency of higher stress concentrations at higher deformations.

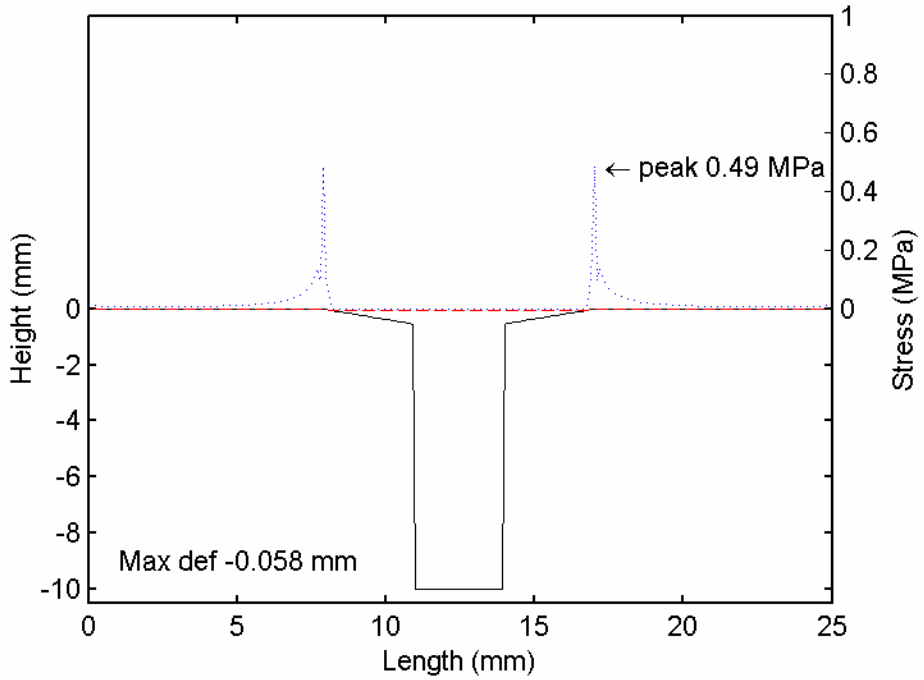

Figure 3.2.21 Geometry (solid), stress distribution (dotted), and rubber deformation (dashed) for tines with 3 mm width, entry angle of 10° and 10 mm depth

The PSD plot for this stress distribution is shown in Figure 3.2.22; this spectrum follow the same pattern as the one for the rounded edge, but having a slight increment in the pressure of approximately 1 dB. The overall noise level is 162.7 1 dB, which is, 0.69 dB higher than the rounded edge tine. The similarities among these two spectra are due to the spacing between the two main events that is approximately 9 mm. The intensity of the peak stress gives a small rise in the overall band level on the spectrum.

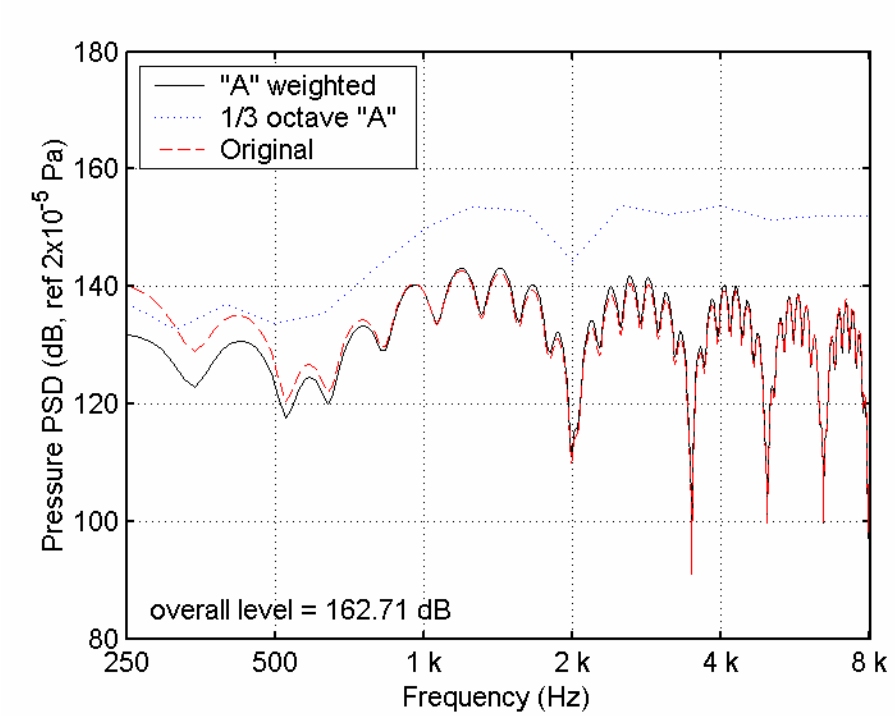

Figure 3.2.22 Frequency spectrum of the stress distribution for a speed of 13.41 m/s for a tine with 3 mm width, 10mm depth, and entry angle of 10

The lowest peak stress case is where the peak stresses in the bevel tine are concentrated almost equally on the external and internal edges of the tine, as shown in Figure 3.2.23 for the 3 mm width case. This angle varies for the different widths of the tine. For the case of a tine of 3mm width and an angle of 2°, the stress at the outer part of the tine is 0.19 MPa and in the inner part of the tine is 0.20 MPa. The maximum rubber penetration for this tine is 0.125 mm; this deformation lowers the peak stress.

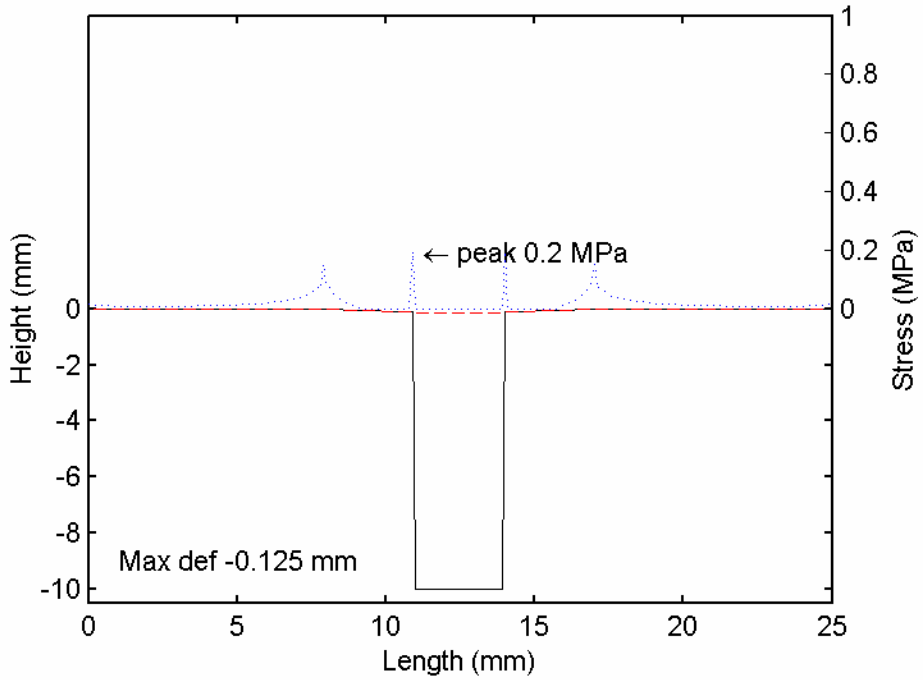

Figure 3.2.23 Geometry (solid), stress distribution (dotted), and rubber deformation (dashed) for tines with 3 mm width, entry angle of 2° and 10 mm depth

The PSD plot for this stress distribution is shown in Figure 3.2.24. This plot is similar to the 10° bevel and the 3 mm circle edge, but it has less energy in the full frequency range of the spectrum. The decrease in energy is an effect of lower peak stresses, and the similarities in the shape of the spectrum are due to the spacing of the stress concentration points. The power spectrum shows levels below 135 dB for frequencies below 1 kHz, having the minimum value of 135 dB on frequencies around 500 Hz. The overall band noise level for this case is 158.27 dB being the lowest for any bevel angle for this tine width.

Comparing the different modes for the bevel tine, a noise level reduction is shown for the "optimum" entry angle 2°, with an overall pressure level of 158.26 dB on the rubber. The other two modes have noise levels of 162.71 and 160.7 dB. For this case, the prediction of having lower noise levels by minimizing the peak stress concentration seems to be valid.

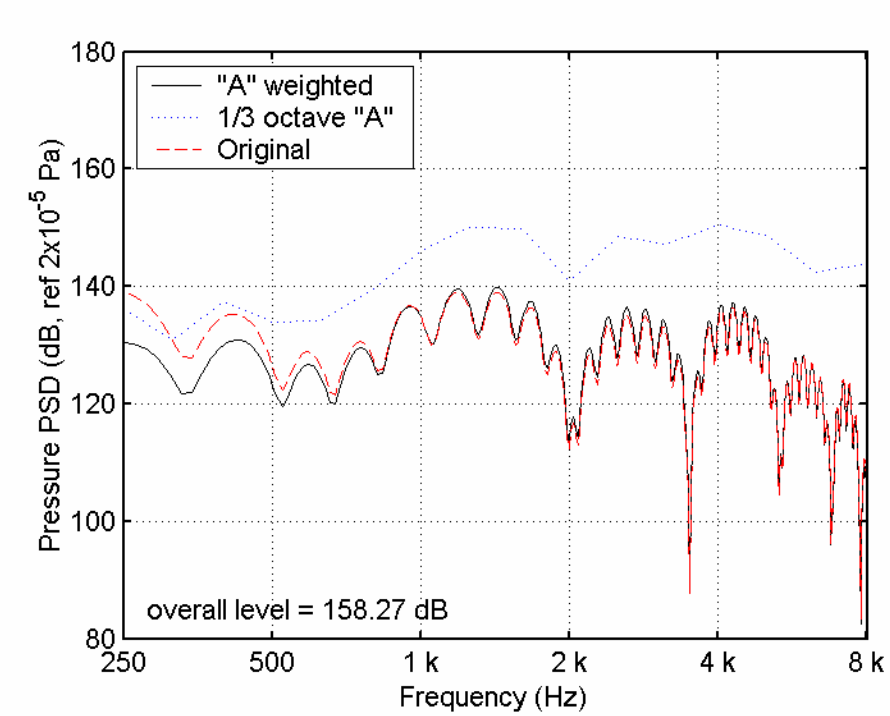

Figure 3.2.24 Frequency spectrum of the stress distribution for a speed of 13.41 m/s for a tine with 3 mm width, 10mm depth, and entry angle of 2°

In Figure 3.2.25, a relationship between tine width, lowest stress concentration angle, and stress concentration is shown. It can be seen that as width is incremented the angle of the lowest stress concentration point decreases; this tendency is crudely shown because of the modeling resolution having the angle change in increments of 1°. The peak stresses show the same tendency as the width of the tine increases, this tendency agrees with what was shown for the square tine.

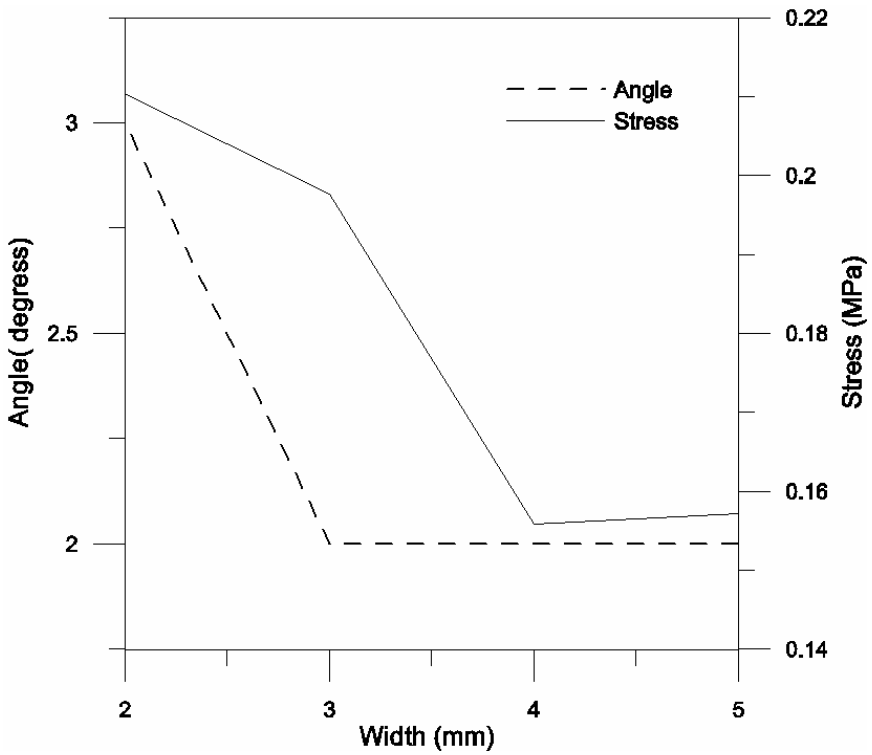

Figure 3.2.25 Relationship between width, peak stress, and angle; for bevel tines with widths of 2, 3, 4, and 5 mm

The influence of the bevel angle on the tire deformation is shown in Figure 3.2.26; here is important to note that the maximum penetration of the rubber for each of the different widths is at the same angle as the lowest peak stresses for each one of these cases. Lower stresses are seen at higher deformations. The influence of the penetration of the rubber is important for the air pumping phenomena. The peak deformation for the optimal angle of 2° for a 3 mm width tine is 0.125 mm.

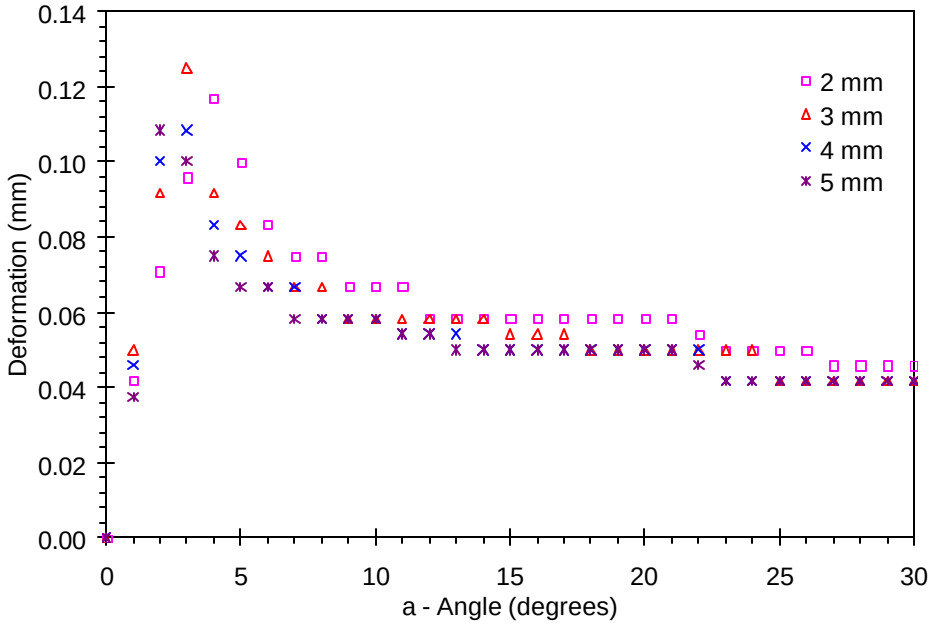

Figure 3.2.26 Maximum penetration of the rubber for bevel tines; for 1, 2, 3, 4, and 5 mm widths and 10 mm depth, varying entry angle from 0° to 30° with 1° increments

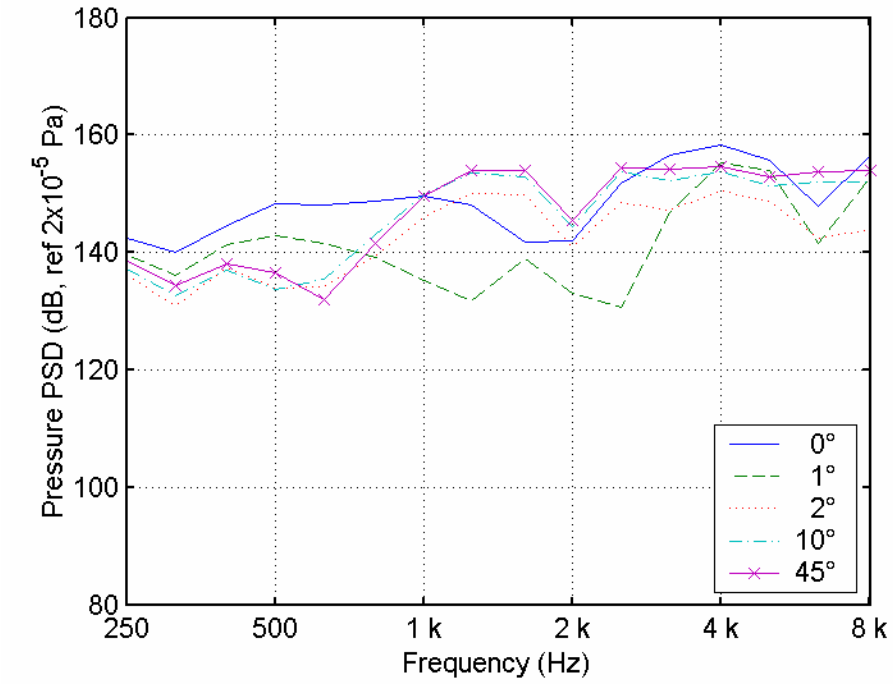

Figure 3.2.27 Comparison between PSD spectra of different angle of bevel tines; 0, 1, 2, 10, and 45° bevel

3.2.5 Variation of Depth of Uniform Texture

The depth of a uniform triangular texture of a wavelength of 1.0 mm was varied to assess the influence of the depth on the stress generation. The variation in the texture depth was done in increments of 0.01 mm to a maximum of 1 mm. The influence in stress generation is shown in Figure 3.2.28. Two tendencies are shown. In the first tendency, the peak stress start from 0 MPa and goes to a maximum value of 0.23 MPa, this happens because the modeled surface starts initially as a plain surface, and then the dents start growing in the surface generating stresses. When the depth of the dents is small, the rubber deforms enough to penetrate deep into the dents and relieves some stress, as shown in Figure 3.2.29. In the second tendency, the depth of the triangular texture is larger and the rubber will penetrate less in comparison to when the texture is small. After 0.03 mm, the influence of the depth becomes constant for this wavelength, reaching a peak stress of 0.23 MPa at 0.03 mm of wave depth.

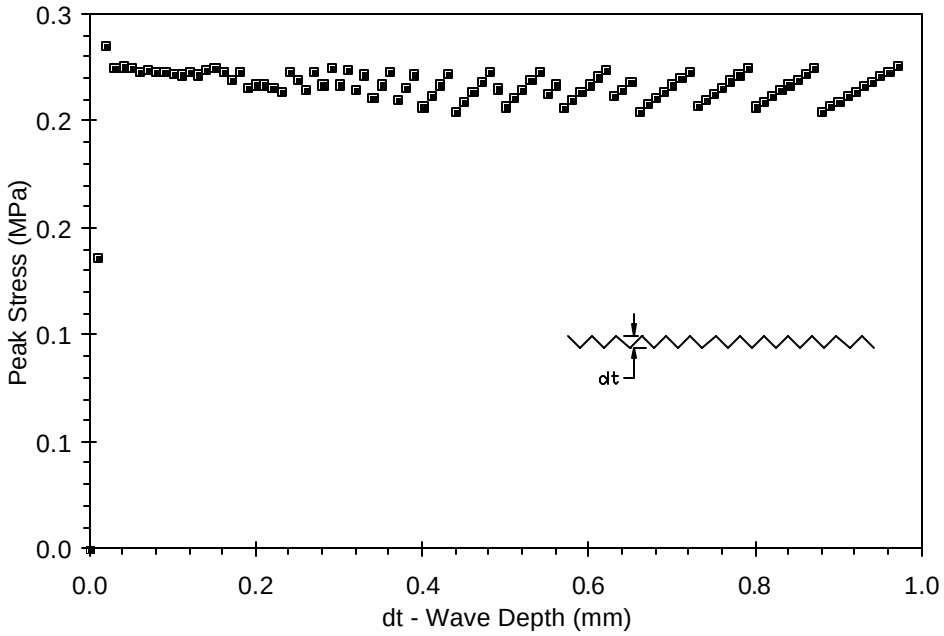

Figure 3.2.28 Maximum stresses for uniform triangular texture varying the texture depth; with a 1.0 mm wavelength varying the depth from 0.01 to 1 mm in 0.01 mm increments

The stress distribution shown in Figure 3.2.29, suggests that the stress concentrates at the tips of the texture. The stress has two different magnitudes; this issue

is not related to the surface texture, it is a modeling issue, since the program is trying to balance the applied load to the stress generated. Sometimes one of the peaks of the texture will be higher that others. The peak stresses are 0.217 and 0.15 MPa. This intensity is considerably smaller that for the tines because the stress is distributed in the whole length of the texture, as compared to two or four points for the square and beveled tines.

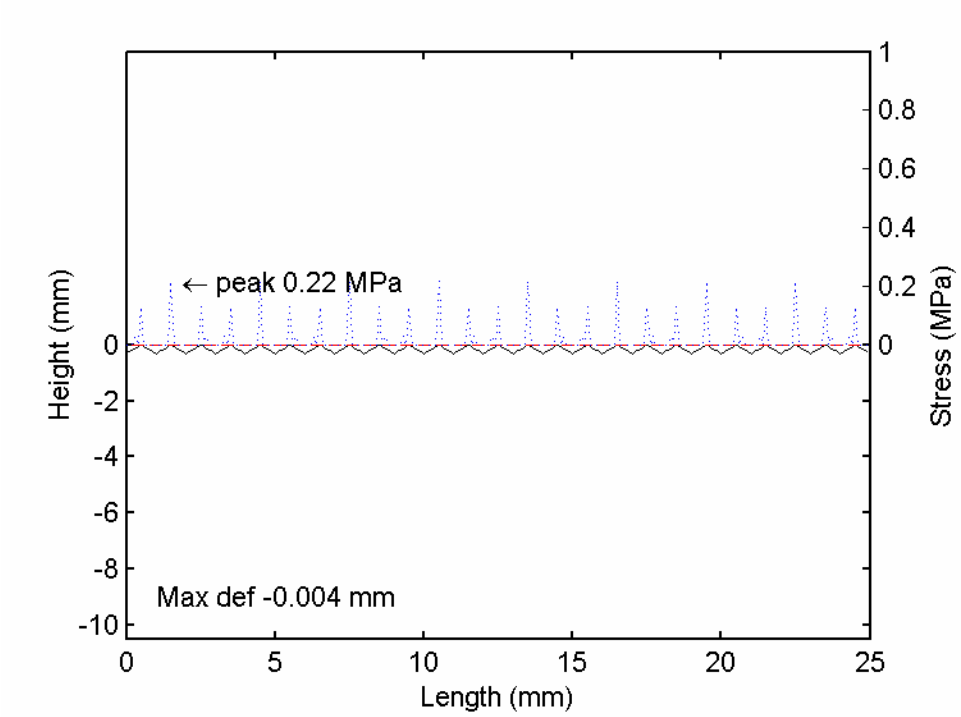

Figure 3.2.29 Geometry (solid), stress distribution (dotted), and rubber deformation (dashed) for uniform triangular texture with 1 mm wavelength and 0.3 mm depth

The PSD plot is shown in Figure 3.2.30; for this case, the filtered spectrum has a pressure level below 140 dB for frequencies above 600 Hz. Below this frequency, there is a reduction of pressure to 110dB at 500 Hz. The overall noise pressure level is 155.45 dB. The maximum deformation of the rubber for this wave depth is 0.0035 mm. Figure 3.2.31 shows the maximum deformation for different depths. The maximum deformation reaches a value of 0.0035mm for depth above 0.3 mm.

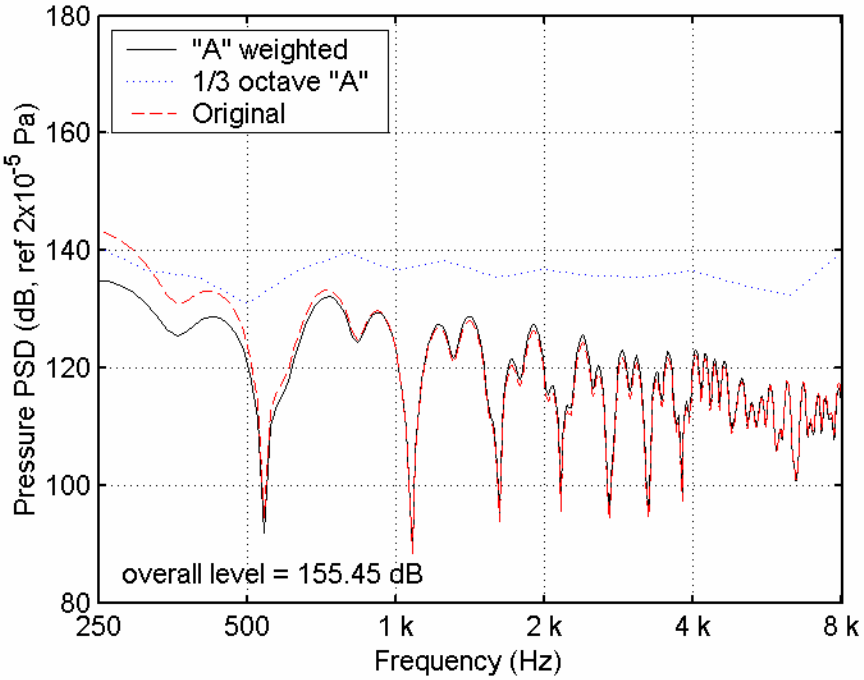

Figure 3.2.30 Frequency spectrum of the stress distribution for a speed of 13.41 m/s for a uniform triangular texture with 1 mm wavelength and 0.3 mm depth

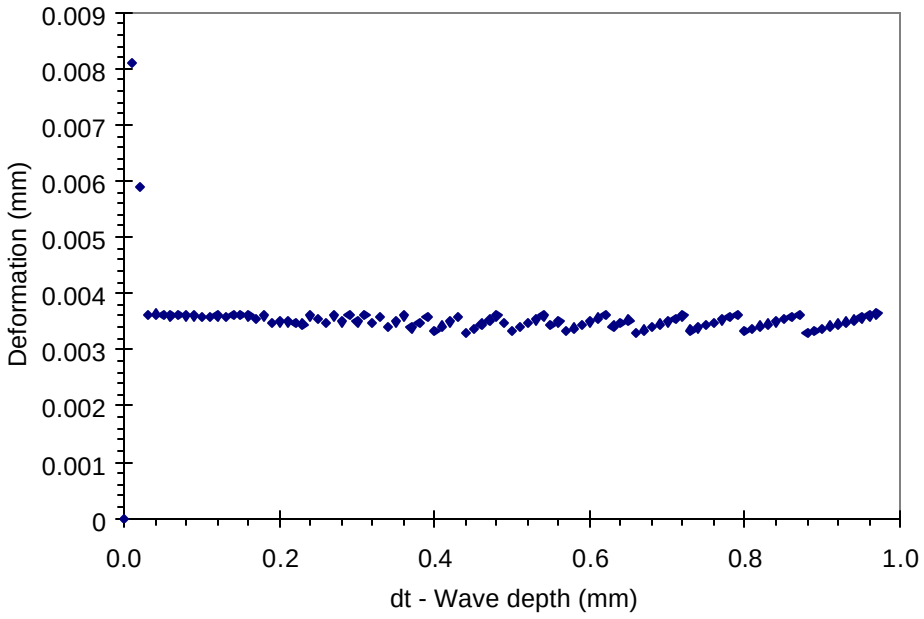

Figure 3.2.31 Maximum deformation for uniform triangular texture varying the texture depth from 0.01 to 1 mm in 0.01 mm increments with 1.0 mm wavelength

3.2.6 Variation of Width and Depth of Uniform Texture

The width and the depth of a uniform texture were varied, to asses the influence on stress generation. The wavelength was varied in a way that full waves were always produced in the texture length (250 mm) and the height was always exact as shown in Figure 3.2.32. The different wavelengths were 12.5, 5.0, 2.5, 1.0, 0.5, and 0.2 mm and the height was varied from 0 to 4 mm. Figure 3.2.33 shows a relationship between width (wavelength) and depth of a uniform texture is shown.

Figure 3.2.32 Schematic of changing textures with different wave lengths

The wavelength limits the maximum stresses produced on this type of texture. As the texture wavelength decreases, the peak stresses decrease; this is because as the texture becomes finer the influence of the area at the peak of the wave becomes less significant in the stress generation as shown in Figure 3.2.33.

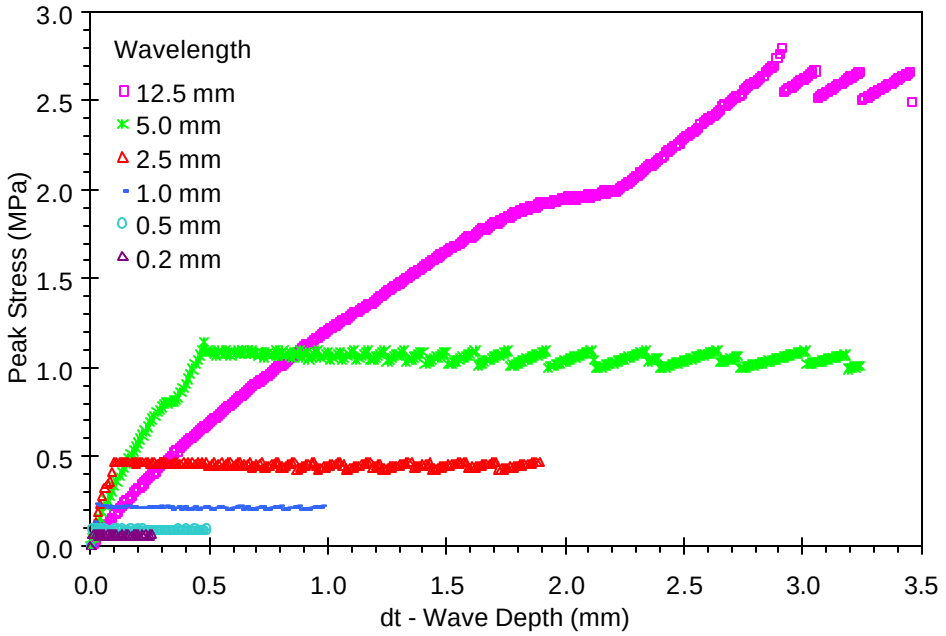

Figure 3.2.33 Maximum stresses for uniform triangular textures varying the texture depth and wavelength; with a 12.5, 5, 2.5, 1, 0.5, and 0.2 mm wavelengths varying the depth from 0.01 to 4 mm in 0.01 mm increments

Figure 3.2.34 shows the stress distribution, rubber deformation, and geometry of a relatively low depth wave texture. The contact area between the tire and the pavement is high, and consequently the stresses on the rubber are low in comparison with higher texture. This texture is considered low depth because the stress is distributed over a large area of the texture tips. The stress generated is distributed over a large area of the triangular shape having a lower value. The peak stress for a triangular texture with a wavelength of 0.5 mm and a depth of 0.15 mm is 0.464 MPa. As is shown in Figure 3.2.34, there are five main stress concentration regions on the length of the surface of 25 mm each one at the peak of the crest of the wave. The maximum deformation of the rubber for this scenario was 0.0323 mm.

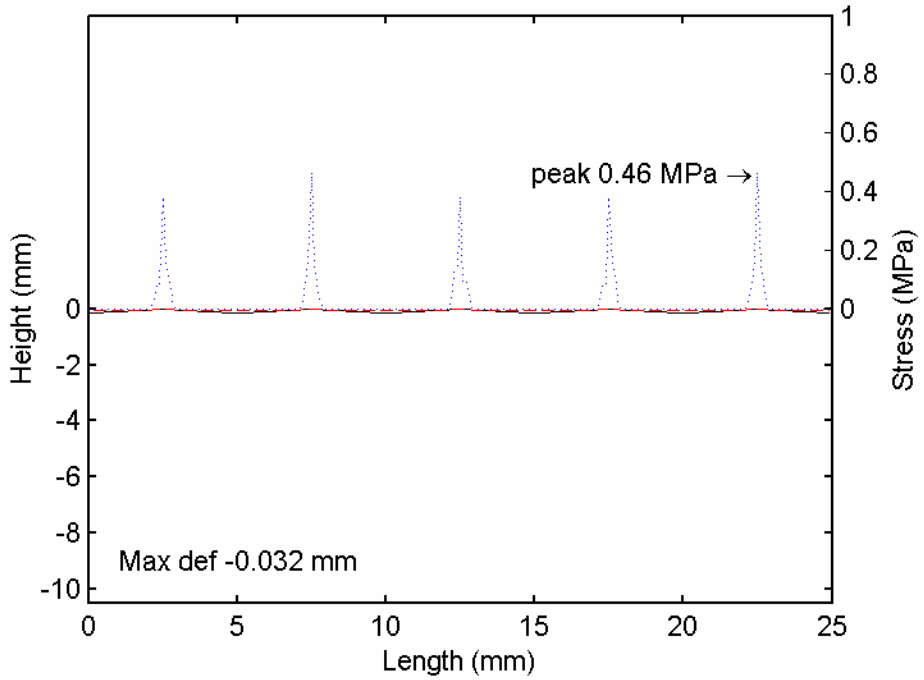

Figure 3.2.34 Geometry (solid), stress distribution (dotted), and rubber deformation (dashed) for uniform triangular texture with 5 mm wavelength and 0.15mm depth

The PSD plot for a texture with a relative low depth is shown in Figure 3.2.35. It can be seen that the pressure level for frequencies between 500 Hz and 2 kHz is fluctuates around 140 dB. The frequency modulation for this tine was 2 kHz. The overall pressure level is 165.53 dB.

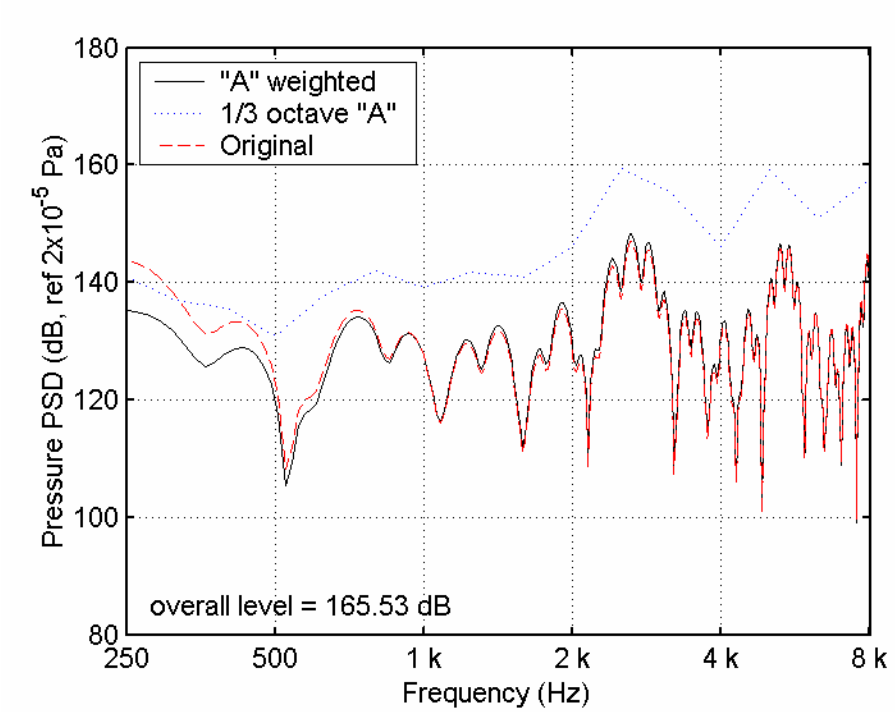

Figure 3.2.35 Frequency spectrum of the stress distribution for a speed of 13.41 m/s for a uniform triangular texture with 5 mm wavelength and 0.15 mm depth

Figure 3.2.36 shows the stress distribution, rubber deformation, and geometry of a medium depth wave texture. In this case, the contact area of the rubber on the texture is less; this gives increases the stress generation. The stress generated is distributed over a smaller area of the triangular shape, resulting in a higher stress concentration at the tip of the triangle. The sum of the areas under the stress plot will be equivalent for the two cases because the total load is the same. The peak stress for the triangular texture with 5 mm wavelength and a depth of 0.35 mm is 0.814 MPa. The stress distribution for the 25 mm sample shows the same five stress concentrations. The penetration of the rubber is 0.03 mm, decreasing from the previous case because as the stress concentrates in a smaller area the deformation decreases.

The PSD plot for a texture with a medium depth is shown in Figure 3.2.37; this spectrum is almost identical to the one for 0.15 mm depth. The similarities are caused by the spacing of the main stress concentration locations. Only a slight increase in the overall level from 165.53 to 166.44 dB is observed; this is a consequence of the rise of the peak stresses from 0.46 to 0.81 MPa.

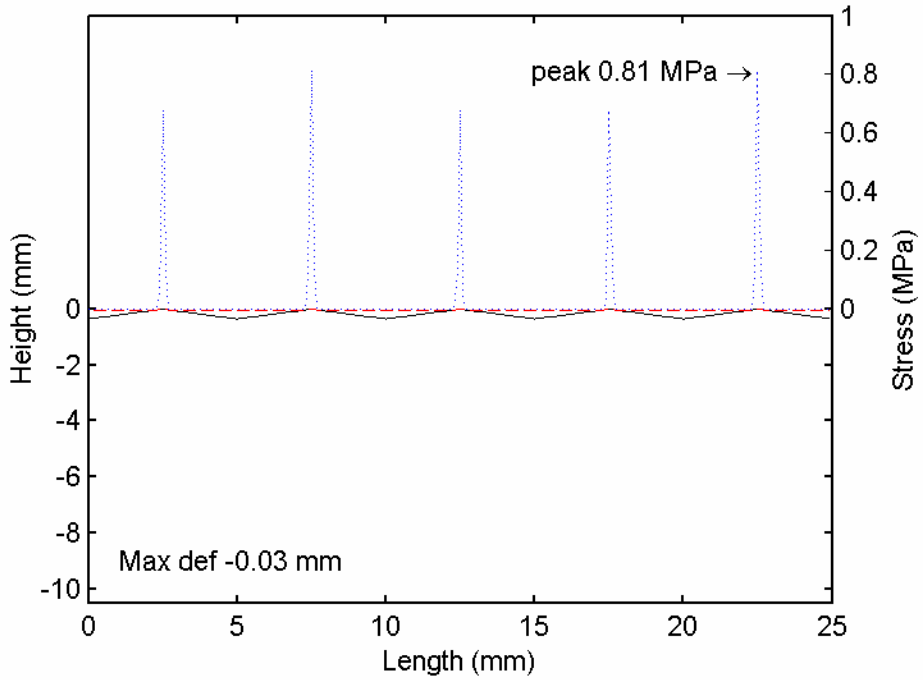

Figure 3.2.36 Geometry (solid), stress distribution (dotted), and rubber deformation (dashed) for uniform triangular texture with 5 mm wavelength and 0.35mm depth

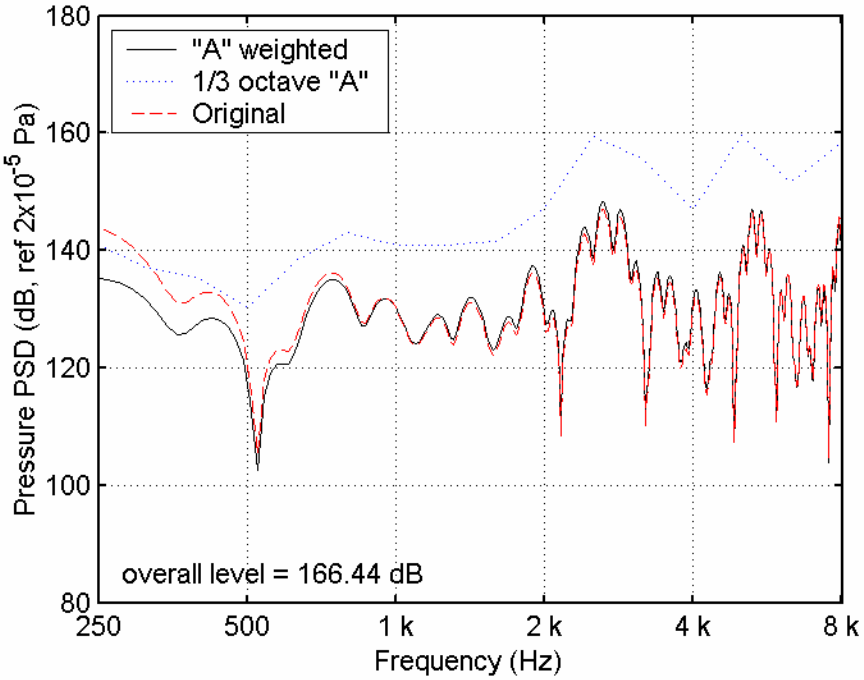

Figure 3.2.37 Frequency spectrum of the stress distribution for a speed of 13.41 m/s for a uniform triangular texture with 5 mm wavelength and 0.35 mm depth

Figure 3.2.38 shows the stress distribution, rubber deformation, and geometry of a texture with a relatively high depth, compared with the previous ones; in this case, we can see that the area of contact between the rubber and the concrete is relatively small, and thus generates higher stresses. The generated stress is distributed over a small part of the triangular shape giving rise to high stress concentration values at the tip. As the previous case, the summation of the area under the stress plot will be equivalent to the two previous textures. The peak stress for the triangular texture with 5 mm wavelength and a depth of 0.60 mm is 1.09 MPa. This case shows the same five concentrations for the 25 mm long texture each of these concentrations being at the peak of the wave. The deformation of the rubber was 0.0175 mm, showing the same tendency of lower deformations for higher stress concentration.

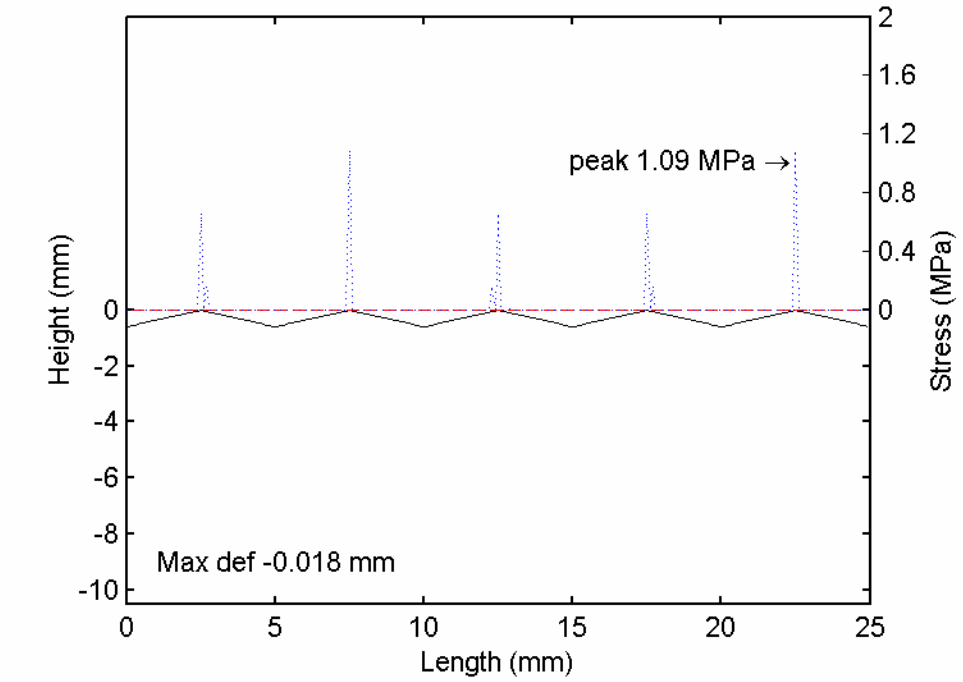

Figure 3.2.38 Geometry (solid), stress distribution (dotted), and rubber deformation (dashed) for uniform triangular texture with 5 mm wavelength and 0.60 mm depth

The PSD plot for a texture with a high depth is shown in Figure 3.2.39. This spectrum is almost identical to the one for 0.15 mm and 0.35 mm depth. The similarities

are caused by the spacing of the main stress concentration locations, with only a slight decrease on the overall level from 166.44 to 166.36 dB.

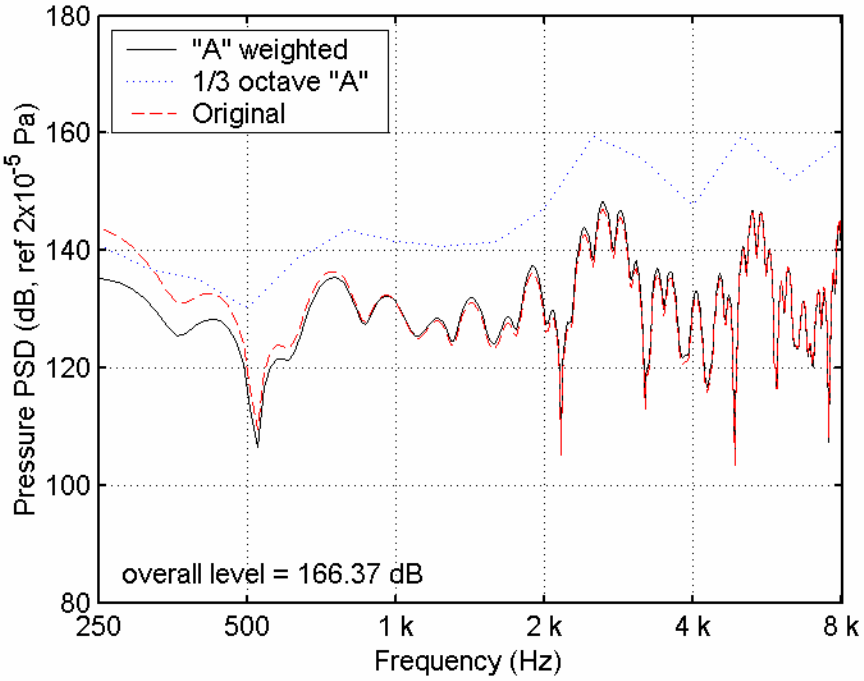

Figure 3.2.39 Frequency spectrum of the stress distribution for a speed of 13.41 m/s for a uniform triangular texture with 5 mm wavelength and 0.6 mm depth

Figure 3.2.40 shows a comparison between depths of 0.15, 0.35, and 0.60 mm for the same wavelength. The levels on the spectrum are incremented at all frequencies as the depth of the wave length is incremented; this happens because as the depth is increased the peak stresses that are generated are incremented as well. There was no change in the modulations because the stress locations do not change as the depth is incremented on the intensity changes.

A comparison by means of a cumulative stress distribution for the different wavelengths between the three cases is shown in Figure 3.2.41; on this graph, three different paths of the stress distribution are shown. The one for 0.15 mm wave depth has the highest number of points with lower stress concentration, meaning that there are multiple points with low stress. The second one with 0.35 mm of wave depth has a lower number of points with low stress concentrations; this is because the stress is focusing on a smaller area. The third one with 0.60 mm of wave depth has the fewest number of points

with low stress concentrations for the samples shown consequently having the highest stress located at fewer points.

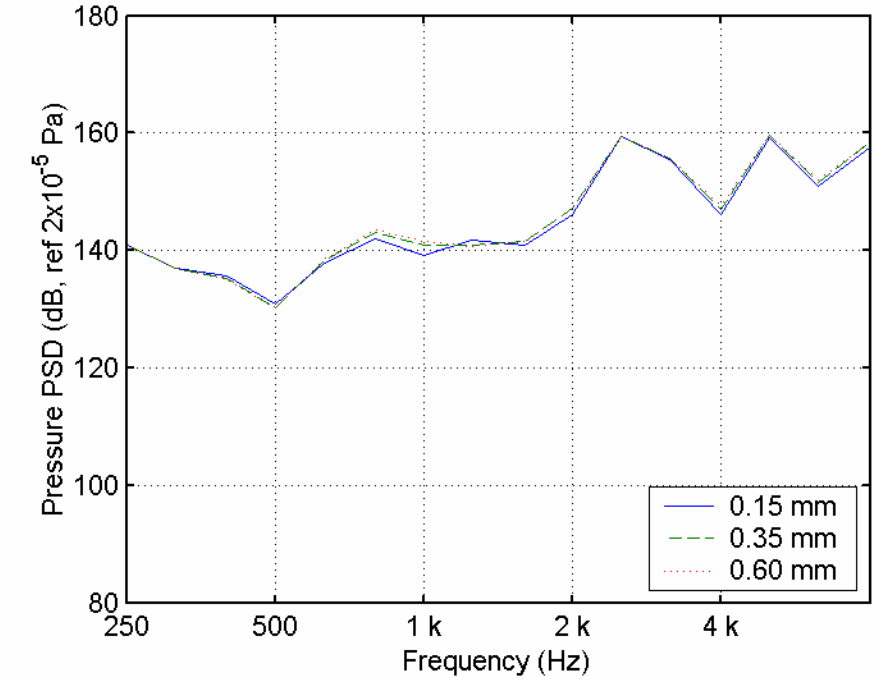

Figure 3.2.40 PSD plots for different wave depths for 0.15, 0.35, and 0.6 mm

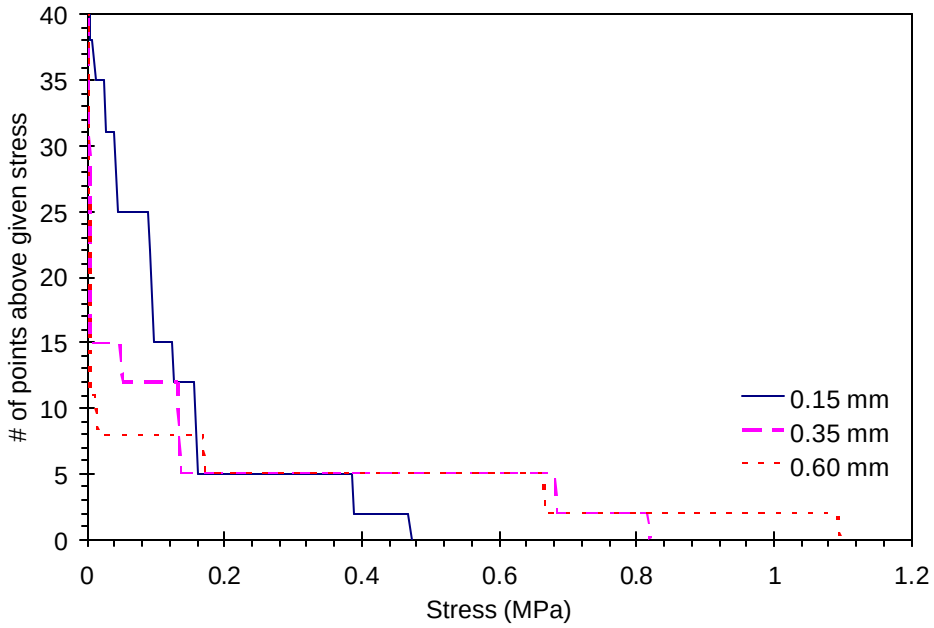

Figure 3.2.41 Cumulative distribution of the stress profile for different wave depths of 0.15, 0.35, and 0.60 mm with a wavelength of 5 mm

The previous examples of the stress distribution show how the contact area between the peaks of the texture influences the stress generated. When the texture height is incremented, the contact area decreases giving a rise to the stress concentration; after a certain height the stress concentration on the peaks of the texture reaches constant value because the influence of the area becomes negligible. A relationship between texture wavelength and maximum peak stresses reached is shown in Figure 3.2.42. This relationship is almost linear; the value for a wavelength of 25.0 mm is not included in this relationship because a constant value of stress was never reached during the modeling.

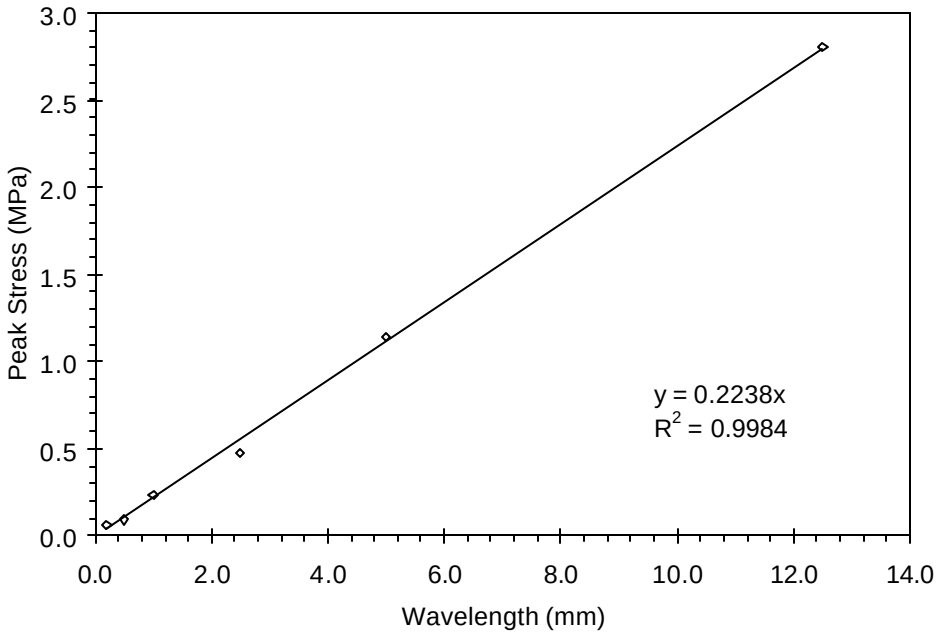

Figure 3.2.42 Relationship between wavelengths and maximum peak stress generated

3.2.7 Variation of Depth of Random Texture

The maximum depth difference of a random texture was varied to asses the influence on the stress generation. The generation of this texture was done through uniformly distributed random numbers by using them as a factor with the desired depth. This generates a maximum depth difference that is used in this case as the reference depth. The depth was varied from 0.01 mm to 1 mm in increments of 0.01 mm. This type of texture resembles more the typical texture of a normal pavement compared to the uniform triangular texture. The peak stresses generated by the depth difference in the

random texture are shown in Figure 3.2.43. The deformation of the tire rubber is shown in Figure 3.2.44. it can be observed that the deformation follows the same tendency as the peak stresses for this case.

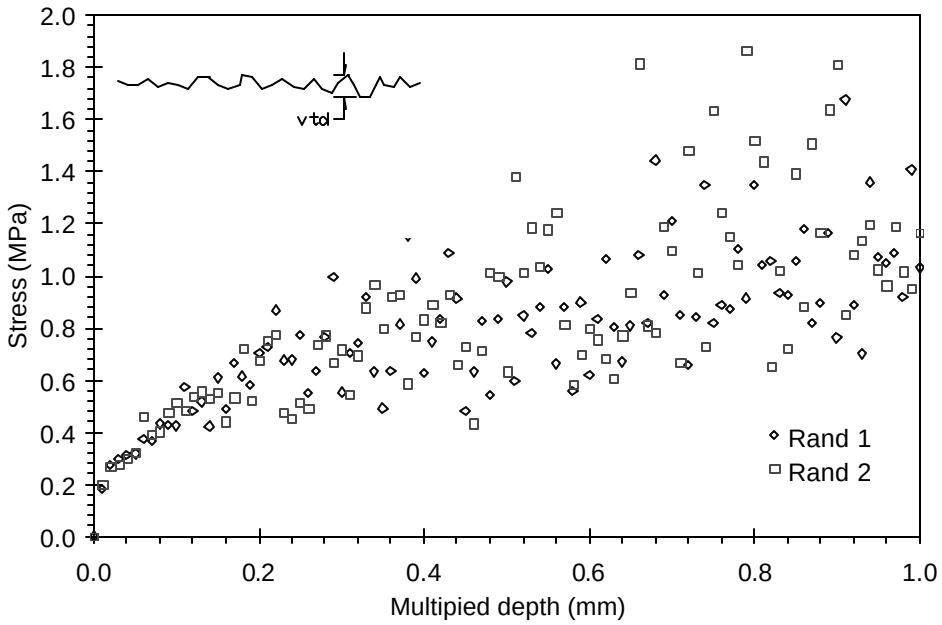

Figure 3.2.43 Maximum stresses for textures with uniform horizontal spacing (0.1 mm) and random depth; varying the texture depth multiplier from 0.01 to 1 mm with 0.01 mm increments

A sample of a random texture shape and stress distribution is shown in Figure 3.2.45. The stress concentration locations are in random positions; the peak stress is 0.47 MPa for a multiplied depth of 0.45 mm. This value is not absolute for this depth but has a range as shown in Figure 3.2.43. The deformation of the rubber is 0.013 mm for this case, but also this value also has a range as shown in Figure 3.2.44.

The PSD plot for the random texture is shown in Figure 3.2.46. It can be seen here that the pressure level has a tendency to be constant with frequency with a value around 155 dB. The overall noise pressure level is 164.16 dB.

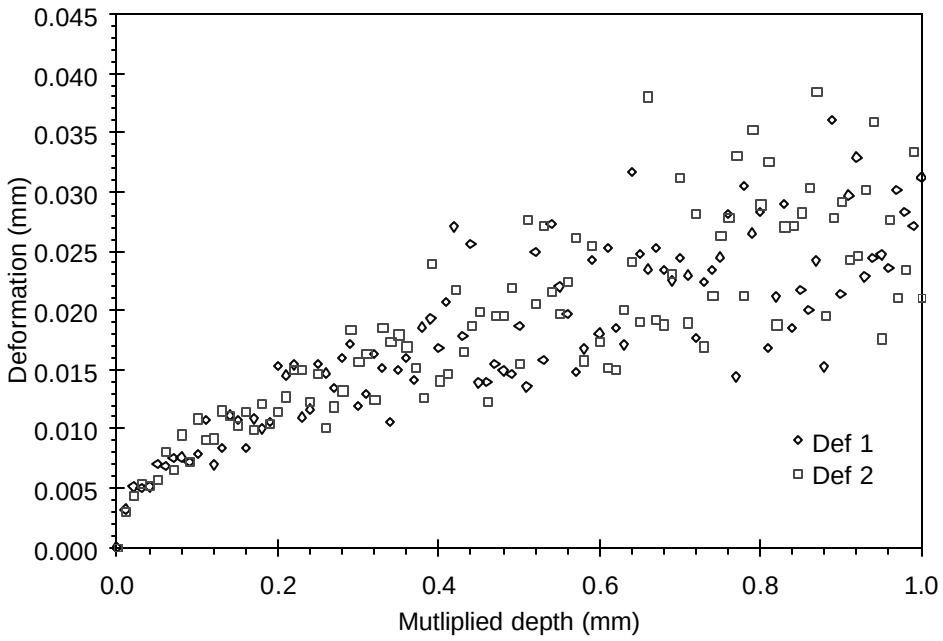

Figure 3.2.44 Maximum penetration of the rubber textures with uniform horizontal spacing (0.1 mm) and random depth; varying the texture depth multiplier from 0.01 to 1 mm with 0.01 mm increments

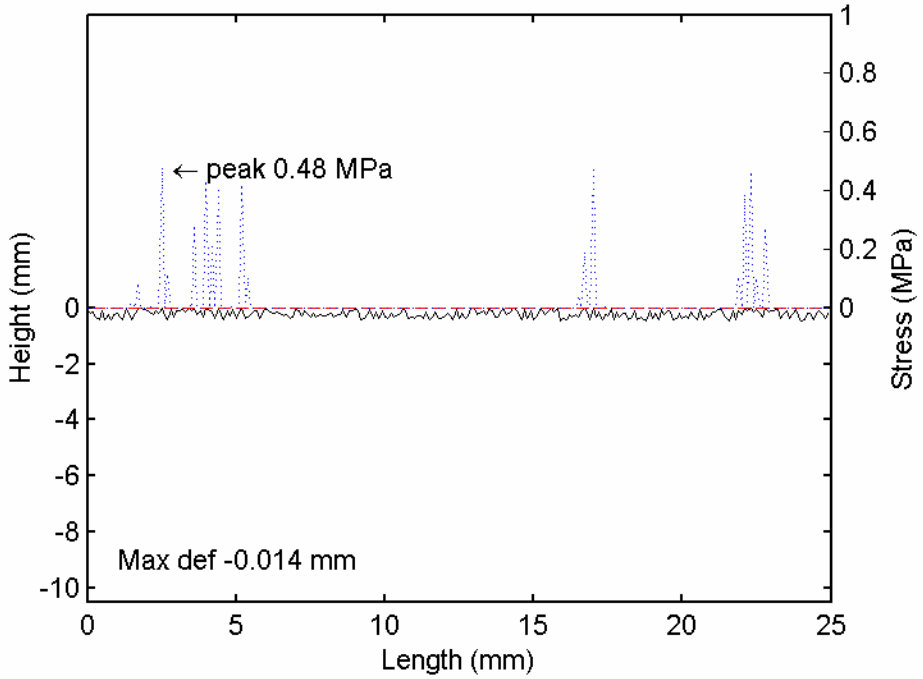

Figure 3.2.45 Geometry (solid), stress distribution (dotted) and rubber deformation (dashed) for random texture with 0.45 mm of multiplied depth

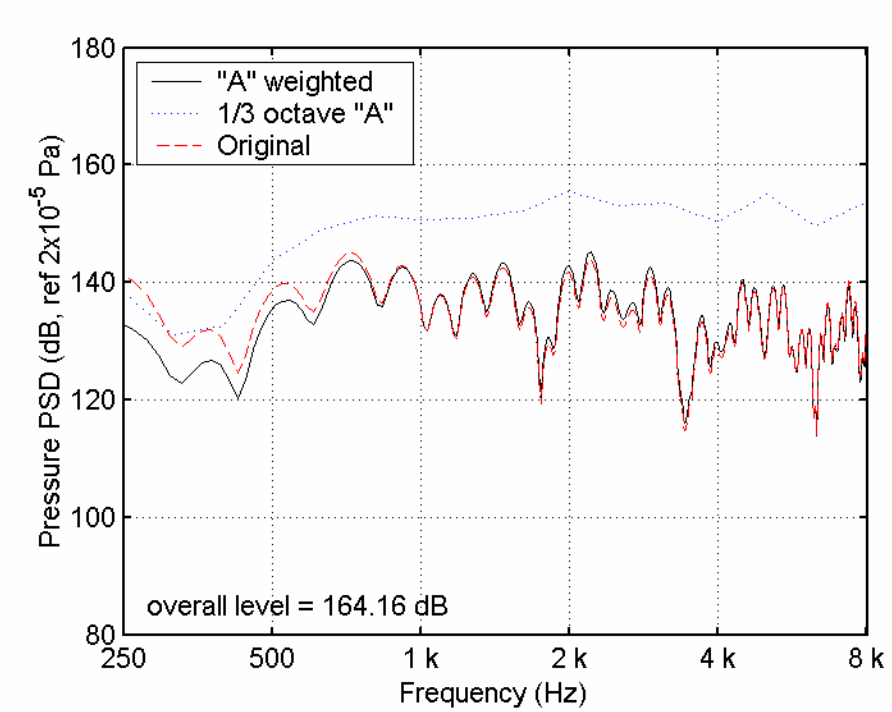

Figure 3.2.46 Frequency spectrum of the stress distribution for a speed of 13.41 m/s for a random texture with 0.45 mm of multiplied depth

3.3 Chapter Conclusions

After performing stress-noise modeling on the different features of the tine geometry and different surface textures, it can be concluded that:

As tine width is changed, there is a change in the modulation frequency of the PSD. The modulation frequency is reduced as the tine width is increased. The overall sound levels had a slight reduction as the width of the tine was increases.

The next variation performed was a change in tine depth. The minimum depth tested was 0.1 mm. From this depth to deeper textures, the contact stress distribution remained the same. From this, it is concluded that tine depth does not affect the stress distribution for depths greater than 0.1 mm.

The next variation performed was rounding the tine edges in order to re-distribute the stress concentration over a larger surface generating a reduction in the peak stress levels. As the radius of the rounded edge was increased, the peak stress was reduced.

This happened for the four different widths tested. The rounding of the edges produced a change in the location of the peak stresses. This change in location resulted in a change of the modulation frequency of the PSD plots.

The next variation performed on the tine edge geometry was beveling the edges of the tines. The bevel was introduced progressively from lower to bigger angles. As the tine edge angle is introduce, the stress concentration started to decrease to a minimum value. After that minimum value, the stress concentration increased up to a value lower than its initial one. The beveling of the geometry produced a change in the location of the main stress concentration that resulted in a change of the modulation frequency of the PSD plot.

The next chapter provides a description of the tire/pavement test apparatus, casting of the samples, and testing performed.

CHAPTER 4 MEASUREMENTS OF NOISE ON TIRE PAVEMENT TEST APPARATUS

This chapter describes the capabilities of the tire/pavement test apparatus (TPTA). Construction of the pavement sections, selection and production of surfaces, and acoustical data acquisition and results, are also described in this section.

4.1 Tire Pavement Test Apparatus

The Tire/Pavement Test Apparatus (TPTA) (shown in Figure 4.1.1) was built to perform tests to better understand the fundamental tire-pavement noise generation mechanisms.

4.1.1 Description

The apparatus is capable of utilizing different pavement samples and tire loading conditions in a controlled environment to simulate tire-pavement interaction and noise generation. The TPTA consists of a stationary drum 3.7 m in diameter. The pavement sections are placed on the circumference of the TPTA. The pavement sections used in this study had different lengths (ranging from 164.26 to 228.37 cm), varying texture type, were 60 cm tall, and have a depth of approximately 20 cm. The outer diameter of the ring with the pavement sections in place was 4.1 m. The existing design can accommodate pavements of different thickness. The TPTA has two rotating arms and can apply a maximum load of 4.45 kN using a screw jack system. The rotating assembly is driven by a DC motor that connects to a gear box and a belt drive system. The drive system is mounted inside the stationary drum having an air cooling system present to

control the temperature while no data is being collected. The TPTA is located inside a hemi-anechoic chamber.

Figure 4.1.1 General view of the tire pavement test apparatus at Purdue University

4.1.2 Physical Capabilities

The TPTA has the ability to run at constant speed ranging from 0 to 50 km/h measured at the interface between the tire and the pavement. The TPTA is equipped with a loading system that allow normal loading between the tire and the pavement to be adjusted over a range from 0 to 4.45 kN; this allows simulation of vehicles up to two tons.

4.2 Construction of Pavement Sections

The concrete slabs that were used in the tests on the TPTA were prepared using ready mix concrete ordered from a local producer.

4.2.1 Mixture Proportions

The mixture proportions of concrete used for this study are shown in Table 4.2.1. This type of mixture is considered a typical paving mixture in the state of Indiana.

Table 4.2.1 Mixture proportioning for concrete slabs used on the TPTA

Material	Proportion (kg/m^3)
Coarse Aggregate #8	1032
Fine Aggregate #23	748
Portland Cement	401
Water Reducer Agent	12
Air entraining Agent	8
Water	98

4.2.2 Details of the molds

The molds used to prepare sections of the pavement used in this study are shown in Figure 4.2.1. The blue prints of the molds are shown in Figure 4.2.2 and Figure 4.2.3. The forms were made of machined steel and have removable side plates to facilitate demolding and removing of the slabs. Three different lengths of the slabs were used in this study to allow different configurations of testing on the TPTA. These lengths were: 228.37, 206.96, and 164.26 cm. The entire pavement surface over which the tire rolled consisted of six separate, interchangeable segments, as shown in Figure 4.2.4. The width of the test slabs was 61 cm and the depth was 20 cm.

Figure 4.2.1 Molds used for casting of the pavement segments (note optional top plates at both ends)

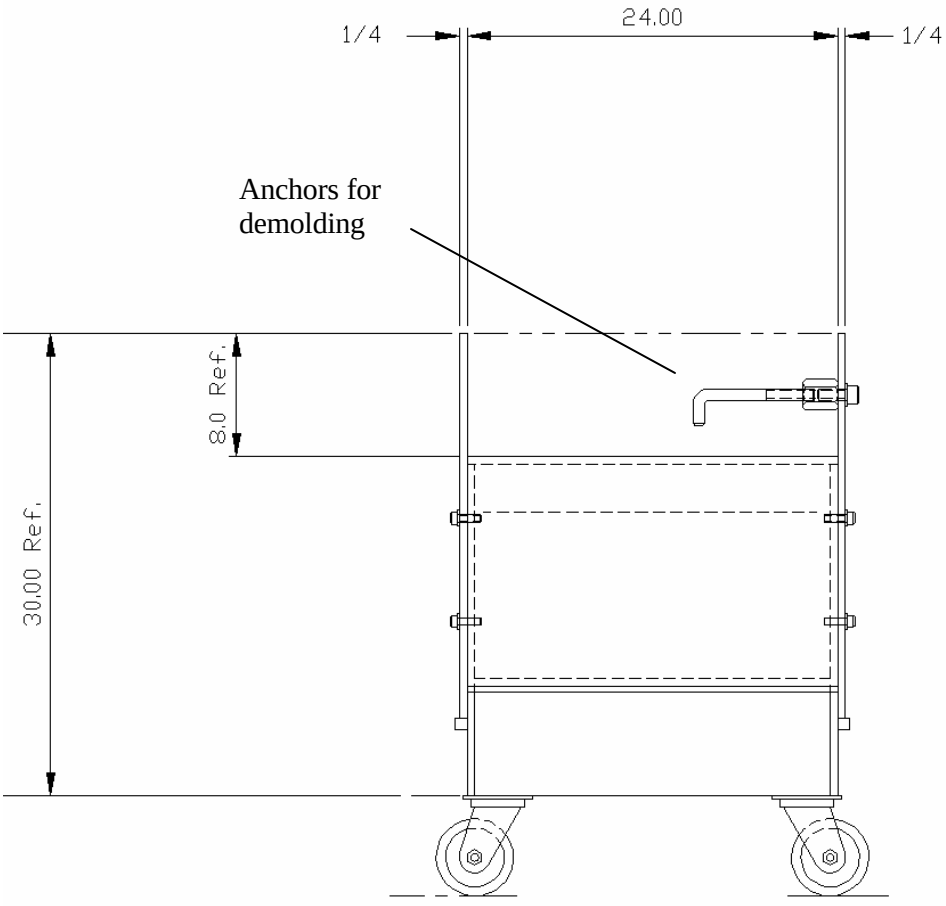

Figure 4.2.2 Blue print of the mold used for casting of the test slabs (side view). All dimensions are in inches

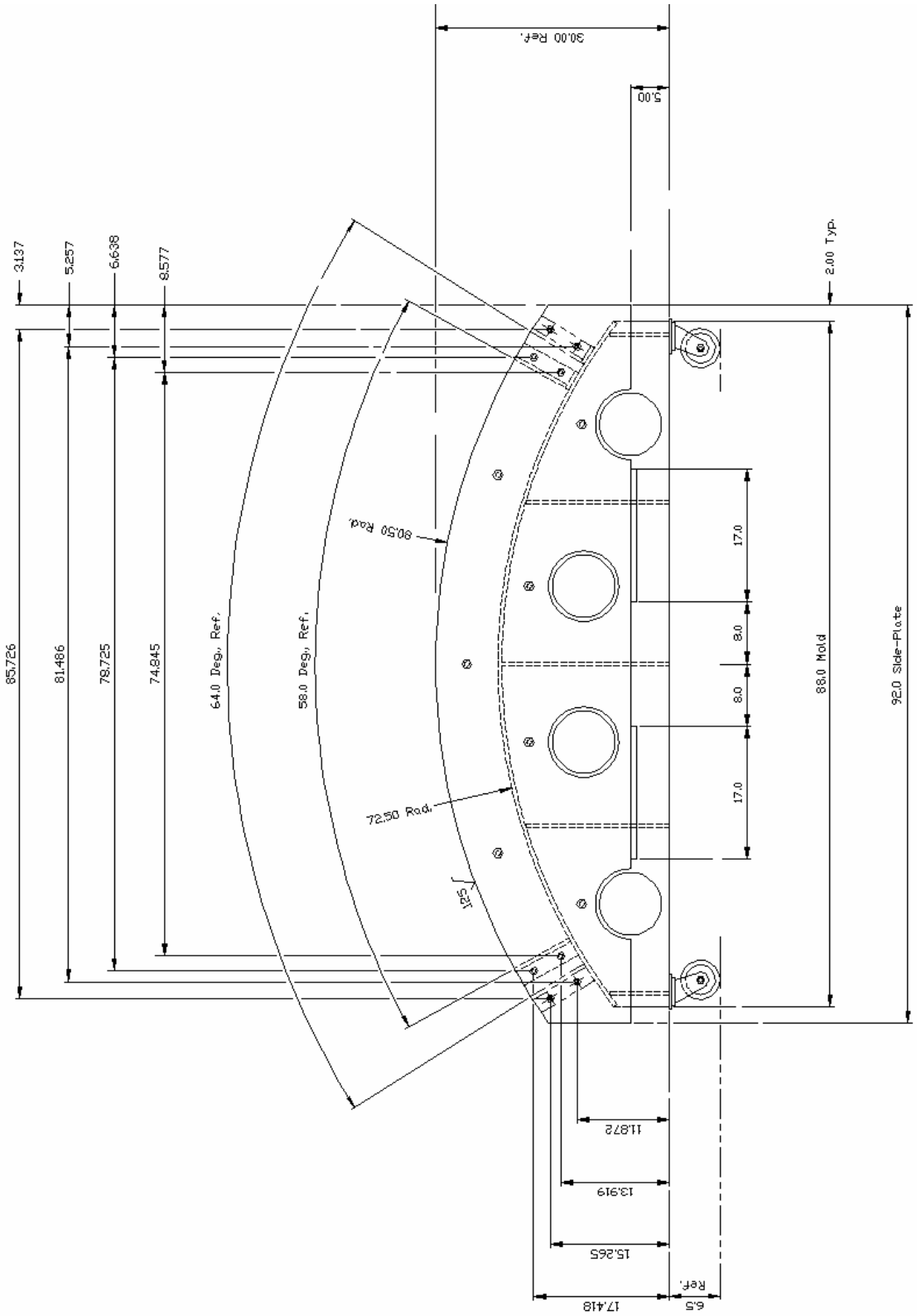

Figure 4.2.3 Blue print of the mold used for casting of the test slabs (front view). All dimensions are in inches

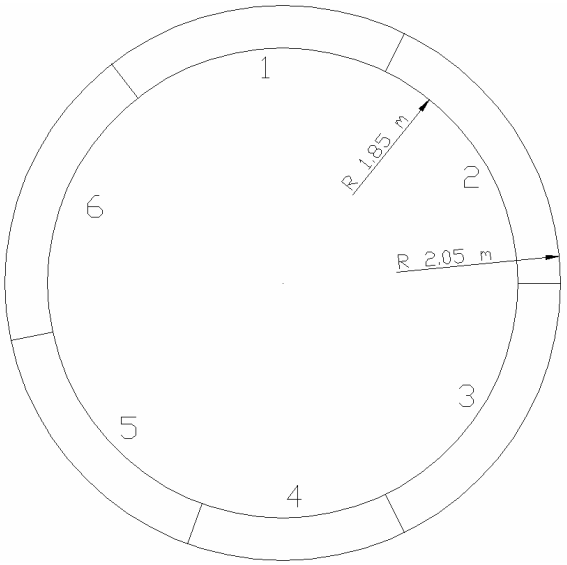

Figure 4.2.4 Top view of segments of the TPTA

4.2.3 Casting and Curing Techniques

Before placement of concrete, all surfaces of the molds were cleaned and primed with demolding oil. The side plates were tightened and, when necessary, optional top plates (see Figure 4.2.1) were placed at the low ends to prevent the mixture from slumping. The top plates were used to help in the casting procedure by minimizing the slumping at the low ends of the mold. Anchor bolts were placed on one side of the molds to help in the demolding process and transportation of the slabs (see details in Figure 4.2.2). The concrete was cast directly from the ready-mix truck into the molds in a single layer as shown in Figure 4.2.5.

The concrete was consolidated using internal vibration and by striking the sides of the molds with a rubber hammer, ensuring that the corners and edges of the mold were properly vibrated. The concrete was then screeded perpendicular to the direction of the tire path using a steel angle. The surface was finished using a steel trowel. The final finishing was done using steel or magnesium trowel for the plain slabs; other finishing techniques were used for additional types of surfaces. The final finishing depended on the type of surface desired for testing. For description of final finishing techniques, the reader is referred to section 4.3.1 Techniques of Surface Preparation.

Figure 4.2.5 Casting of the slabs

The concrete was cured using wet burlap that was placed over the concrete surface after the initial set of the concrete took place. The burlap was then covered with transparent plastic to minimize moisture loss. The burlap was rewet daily and the curing process continued for a minimum of five days after casting.

The slabs were demolded after five days. The side walls of the molds were detached and the slabs were lifted by the anchor bolts with help of a moving crane and transported to the TPTA facility for testing.

4.3 Selection and Production of Surfaces

The road surfaces used for testing were selected to match the real pavement textures and new types of possible low noise textures. Types of road surfaces used in this test are show in Table 4.3.1.

Table 4.3.1 Types of surfaces studied on the TPTA

Type of surface	Approach or Purpose
Steel trowel finish	Produced plain finish slabs to obtain base case noise spectrum
Magnesium trowel	Produced plain finish slabs to obtain base case noise spectrum
Ground surface	Produced to minimize the effect of surface and joint variations on the TPTA
Broom longitudinal	Produced to assess the influence of longitudinal broom texture on noise and friction
Broom transverse	Produced to assess the influence of transverse broom texture on noise and friction
Astroturf longitudinal	Produced to assess the influence of Astroturf texture on noise and friction
Transverse tining with different geometries	Produced to assess the influence of local tine geometry on noise generation
Transverse tining with even (25 mm) spacing	Produced to assess the influence of series of uniformly spaced tines on noise generation

4.3.1 Techniques of Surface Preparation

Steel trowel finish (Figure 4.3.1) was done by passing a steel trowel parallel to the direction of the tire movement. The final finishing was performed after the screeding was completed.

Figure 4.3.1 Steel trowel finish

Magnesium trowel finish is shown in Figure 4.3.2. This finish was accomplished by passing a magnesium towel parallel to the direction of the tire movement. The finishing was performed after screeding with the steel angle was concluded.

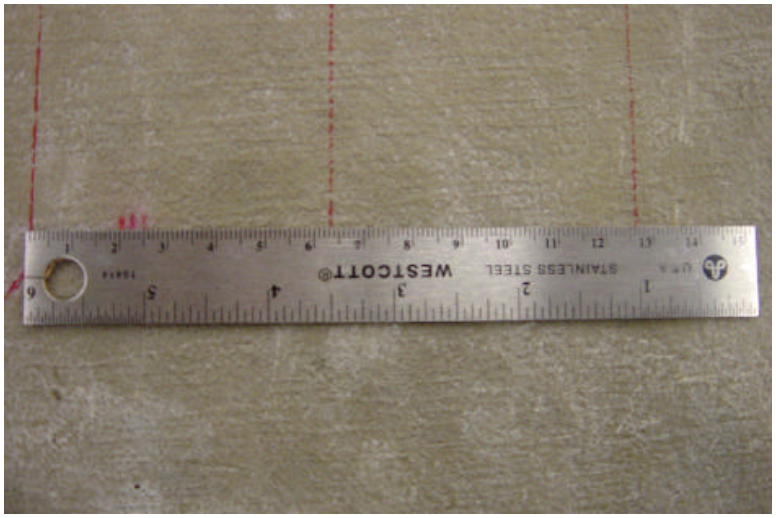

Figure 4.3.2 Magnesium trowel finish

The ground surface, shown in Figure 4.3.3, was prepared by grinding a slab with a steel or magnesium trowel finish. The surfaces were ground to remove any surface irregularities and improve uniformity of the joints between the slabs when they were mounted in the TPTA. The grinding of the surfaces was performed while the slabs remained mounted on the TPTA. A special attachment consisting of three cup grinders, as shown in Figure 4.3.4, was mounted to the rotating arm. The screw loading system of

the rotating arm was used to control the depth of grinding. The grinding was performed by manually moving the rotating arm with the grinders running.

Figure 4.3.3 Grounded concrete surface

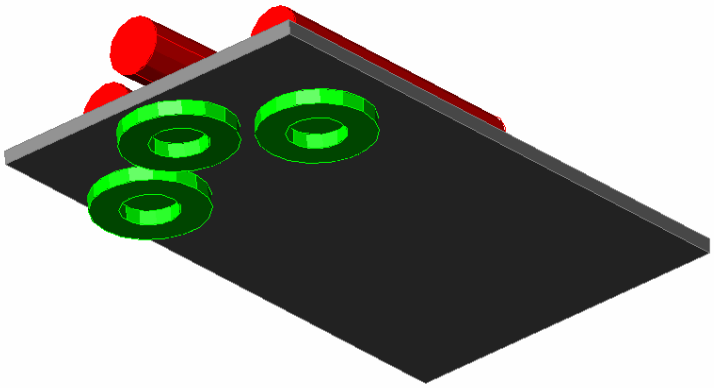

Figure 4.3.4 Grinding attachment for the TPTA

The broom texture, shown in Figure 4.3.5, was prepared by passing a stiff broom longitudinally or transversely over the surface of the concrete. The texturing was done after an initial steel trowel finish. The casting of the broom texture samples was done using the optional top plates to minimize the slumping of the mixture.

Figure 4.3.5 Broom textured concrete surface

The Astroturf texture, shown in Figure 4.3.6, was prepared by passing an Astroturf mat over the surface of the concrete with a concrete block, functioning as a ballast placed on the top of the mat. The direction of the texture was parallel to the movement of the tire. The texturing was done after an initial steel trowel finish.

Figure 4.3.6 Astroturf textured concrete surface

Transverse tining with different geometries was produced by grinding transverse tines using blades with special geometries on a plain ground slab. The geometry of the grinding blades is shown in Figure 4.3.7; these blades were mounted on a right-angled grinder with a rail system to control depth. The spacing between each tine was 25 cm to

ensure that the pervious tine was not affecting the next tine. An example of rounded edge tine is shown in Figure 4.3.8

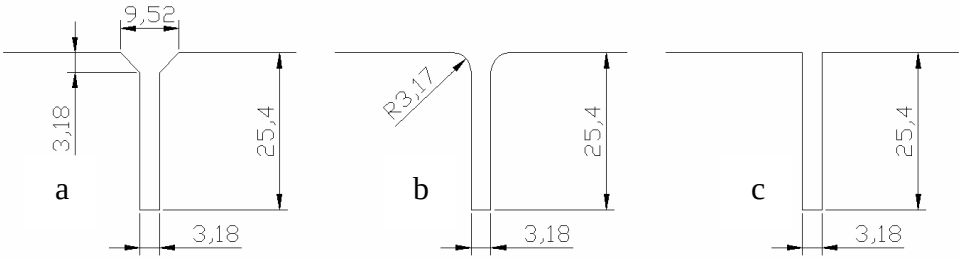

Figure 4.3.7 Ground profile created by the different blade geometries used to cut different transverse tines (mm); a) beveled edge, b) rounded edge, and c) square

Figure 4.3.8 transverse rounded edge tine

Transverse ground tines, shown in Figure 4.3.9, were produce using a circular saw mounted over a rail system to control depth. The tines were ground into a surface ground slab. The width of the tines was approximately 3 mm. The depth of these tines was approximately 10 mm. The tines were evenly spaced 25 mm.

Figure 4.3.9 Ground tines (uniformly spaced at 25 mm)

4.3.2 Mounting of Road Sections on the TPTA

The pavement surface over which the tire rolled consisted of six separate, interchangeable segments. Three lengths of slabs were used and included four 228.37 cm long segment, one 206.95 cm long segment and one 164.26 cm long segment. The total length of the six slabs placed on the TPTA was 1284.70 cm. The pavement segments were mounted over a rubber mat to reduce noise at the steel drum concrete pavement interface. The samples were secured to the TPTA using steel clamps that were attached to the anchor system, as shown in Figure 4.3.10.

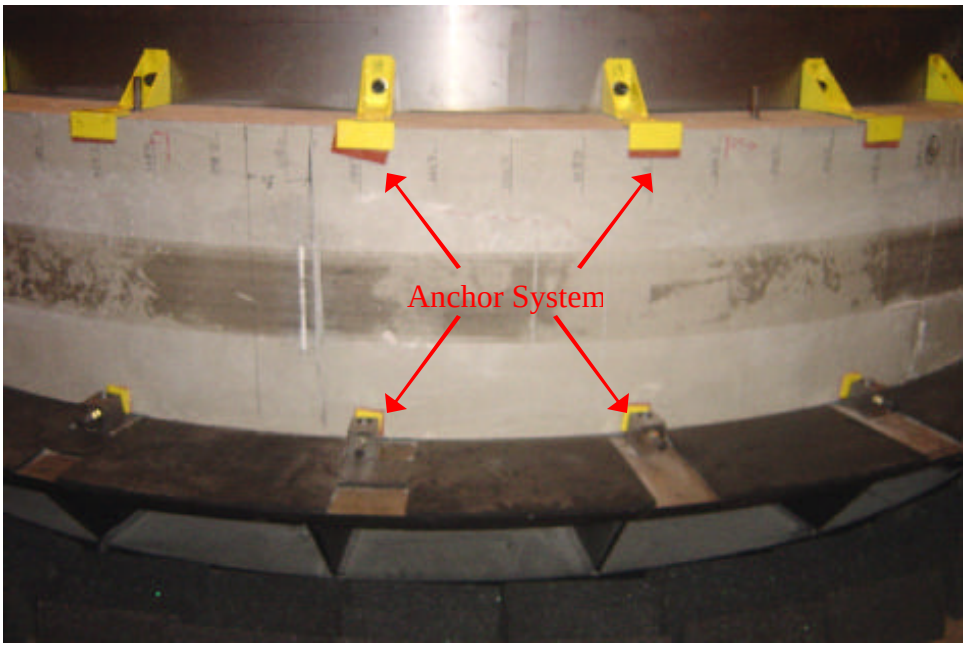

Figure 4.3.10 Anchoring system used to attach pavements segments to the test ring of the TPTA

4.4 Data Acquisition

The TPTA was equipped with a Bruel & Kjaer PULSE Noise and Vibration Analysis Type 7700 system that uses wireless technology. This allowed the system to communicate with the PULSE computer without the need for a slip-ring arrangement.

The TPTA was equipped with an array of five microphones that traveled with the tire, as shown in Figure 4.4.1. The microphone array was set up in such a way that three of the microphones satisfy the requirements of the Close Proximity Method (CPX) draft standard [ISO/CD 11819-2]. Two other microphones were placed 5 cm above the pavement surface and away from the tire surface. Only one of these five microphones (lead microphone located 5cm above the pavement surface) was used to collect data in this study. The other four microphones were not used in this study.

Data collection for this system, to be used in conjunction with the modeling, was performed using time averaging over 100 passes of the tire over the surface in question. The averaging technique was chosen to be based on time rather than frequency because

this collection technique of data averages out random noises such as wind noise and random mechanical noise. Time average data collection produces only noise data that occur always at the same time relative to the trigger. The data was obtained in an "A" weighted in a narrow band spectrum for frequencies from 0 to 6400 Hz. The data was later filtered using $^{1}/_{3}$ octave narrow band analyzer algorithm to be able to compare it to the data obtained by computer modeling.

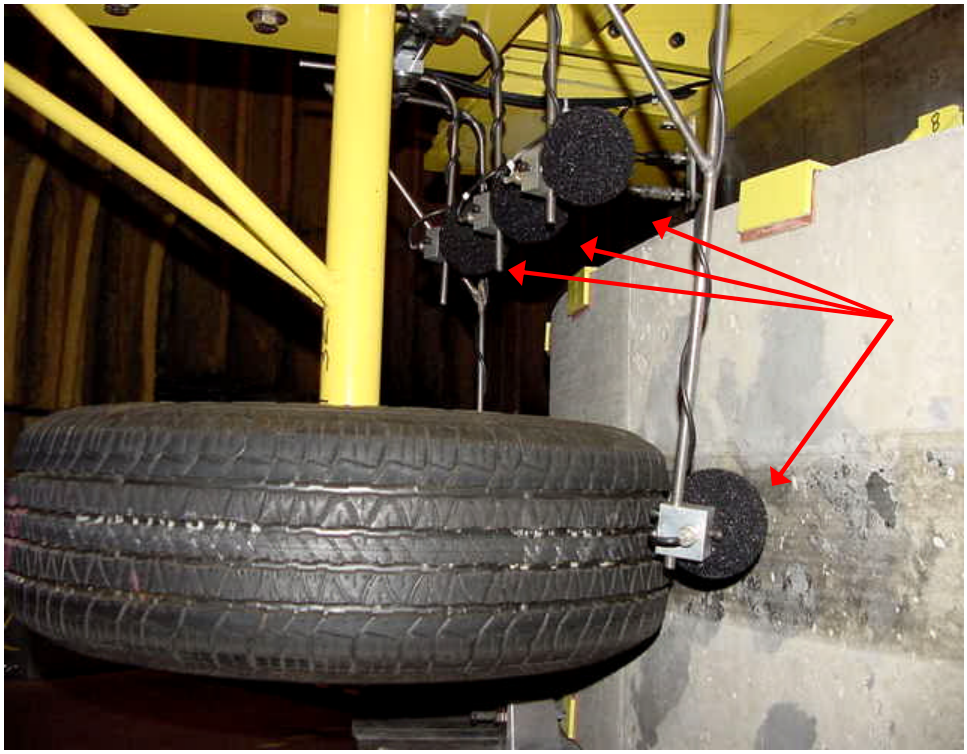

Figure 4.4.1 Five microphone array that traveled with the tire (the fifth microphone is located behind the tire)

4.5 TPTA Test Results

The noise data obtained for different pavements are described in this section. The data is shown in the form of PSD plots directly obtained from the TPTA by time averaging and/or frequency averaging. The frequency averaged data is shown as a means of comparison between the different techniques for data collection. The data has been

"A" weighted during collection. The overall noise level is also calculated for all the samples.

The data collected using time averaging disregards anything that is random in time (for example wind noise). Wind noise is an important factor affecting noise generation especially on textured pavement such as the Astroturf and broomed textured. It is important to note that time averaging spectra are intended only for comparing the computer modeled input force spectra with the data collected.

Frequency average data does not disregard wind noise and provides a more accurate description of the actual noise, but relating frequency averaged data to the stress modeling will be more difficult. In this study frequency averaged data was only used to correlate friction for different textures to overall noise levels.

4.5.1 Textured Surfaces

In this section power spectrum density plots of noise data are shown for the textured surfaces. The collected data is shown as the black solid line, the blue dotted line shows data after filtering $^1/_3$ octave filter. The data is presented in two sets of plots for each surface. The first plot was made using frequency averaging as a data collection procedure. The second plot was made using time averaging as a data collection technique. All the data presented was collected using the near leading microphone.

4.5.1.1 Magnesium Trowel

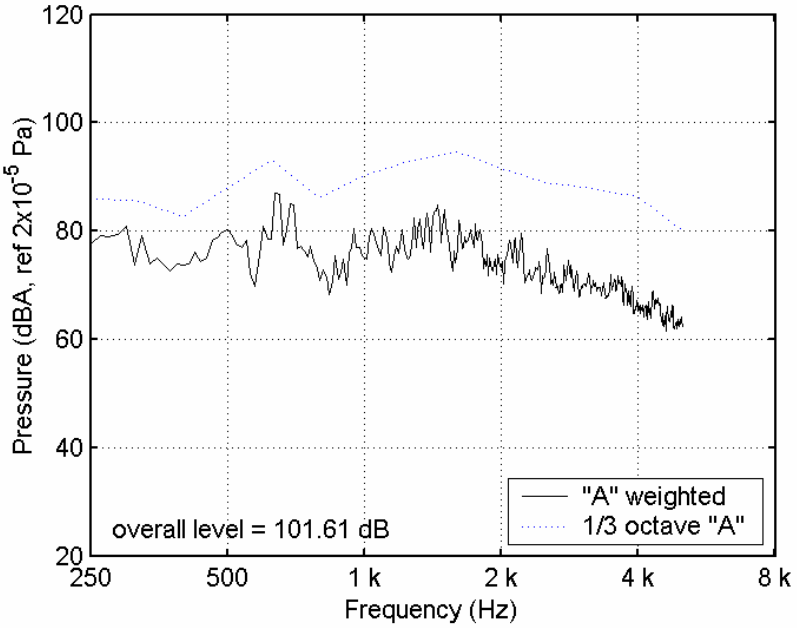

Figure 4.5.1 Frequency averaged PSD plot of noise collected from the magnesium trowel finish concrete surface (lead microphone, unthreaded tire, 13.4 m/s)

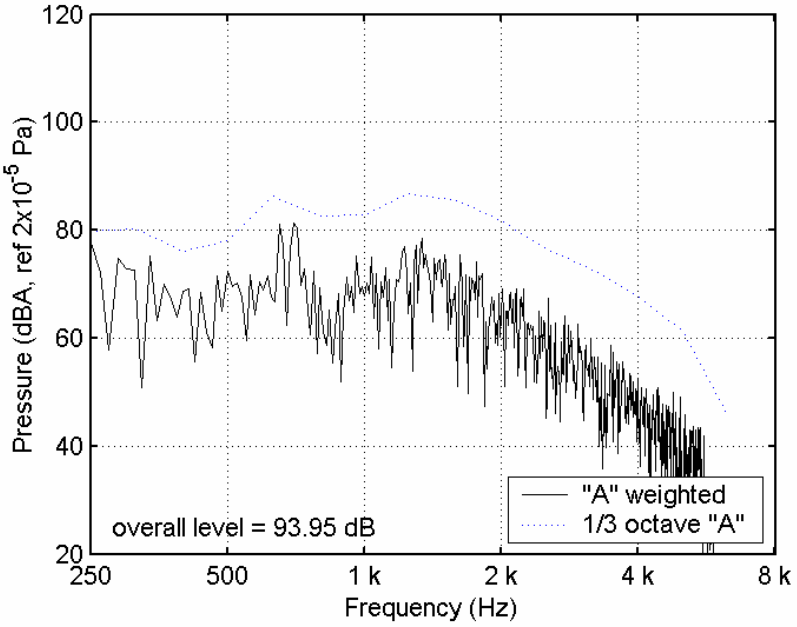

Figure 4.5.2 Time averaged PSD plot of noise collected from the magnesium trowel finish concrete surface (lead microphone, unthreaded tire, 13.4 m/s)

4.5.1.2 Broom Longitudinal

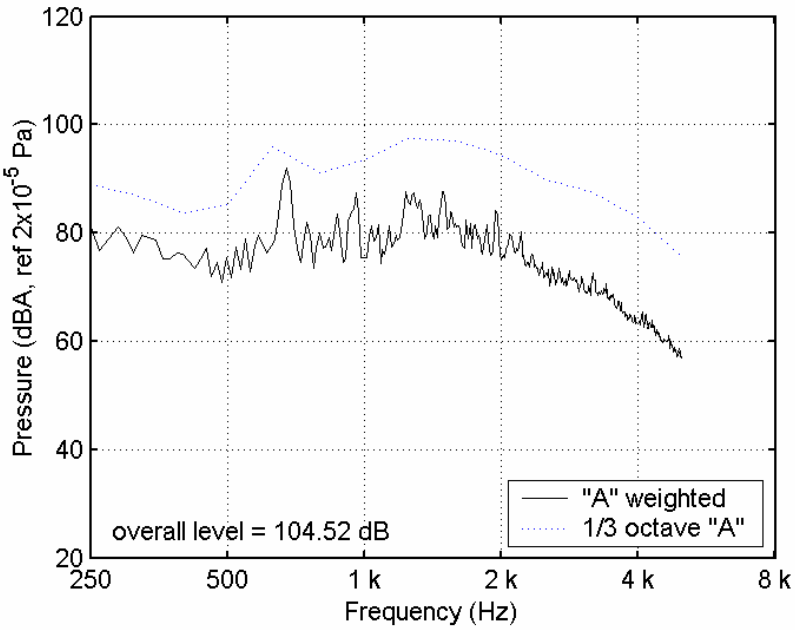

Figure 4.5.3 Frequency averaged PSD plot of noise collected from the longitudinal broom finish (lead microphone, unthreaded tire, 13.4 m/s)

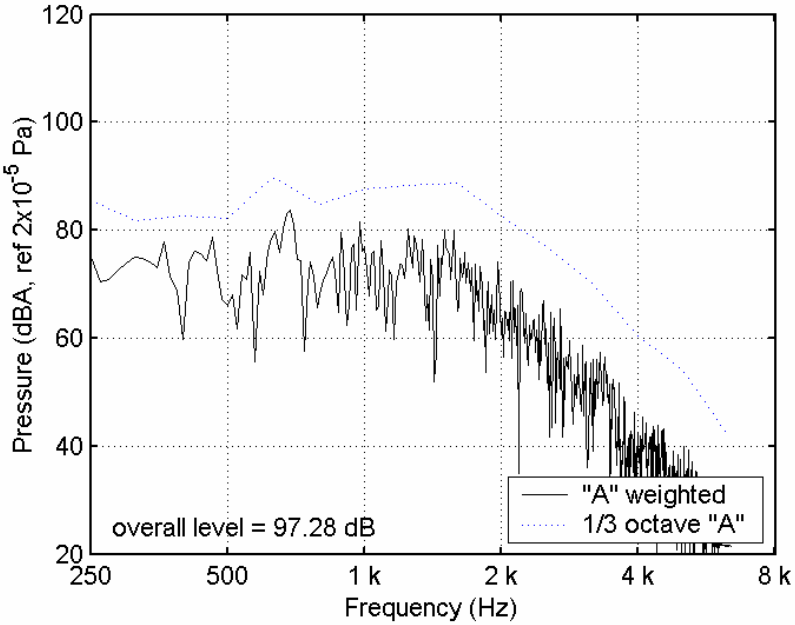

Figure 4.5.4 Time averaged PSD plot of noise collected from the longitudinal broom finish (lead microphone, unthreaded tire, 13.4 m/s)

4.5.1.3 Broom Transverse

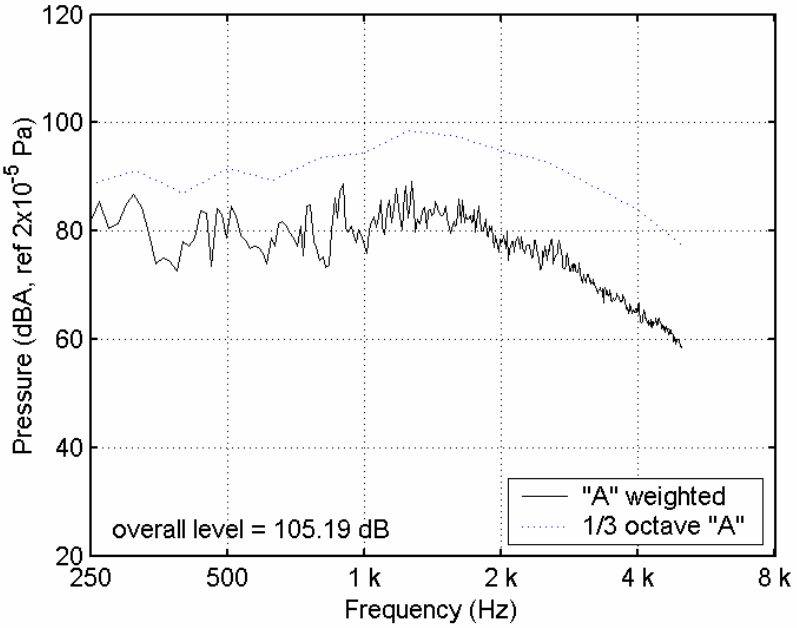

Figure 4.5.5 Frequency averaged PSD plot of noise collected from the transverse broom finish (lead microphone, unthreaded tire, 13.4 m/s)

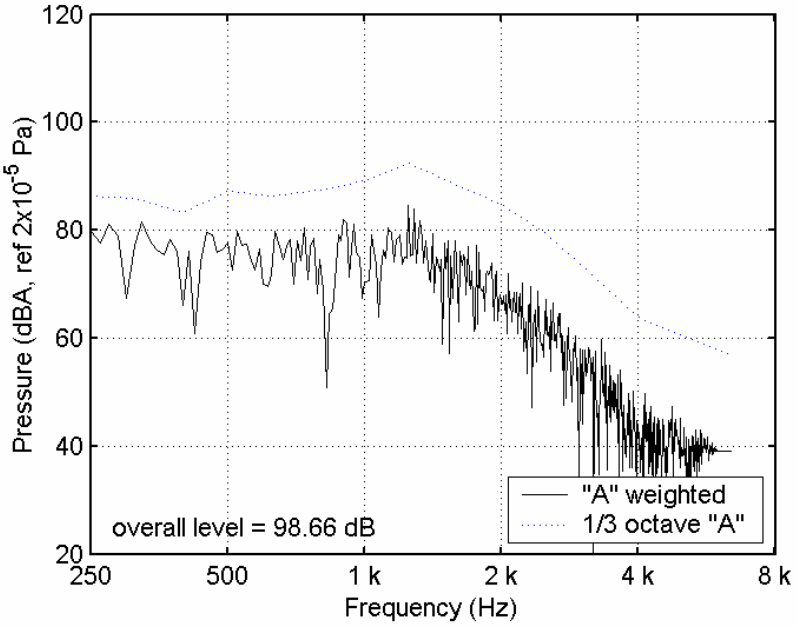

Figure 4.5.6 Time averaged PSD plot of noise collected over a transverse broom finish (lead microphone, unthreaded tire, 13.4 m/s)

4.5.1.4 Astroturf Longitudinal

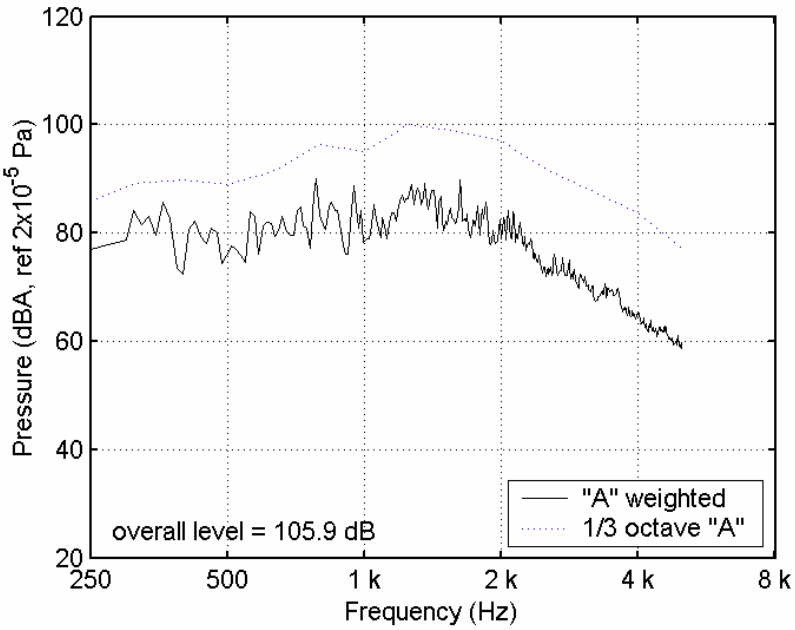

Figure 4.5.7 Frequency averaged PSD plot of noise collected from the longitudinal Astroturf finish (lead microphone, unthreaded tire, 13.4 m/s)

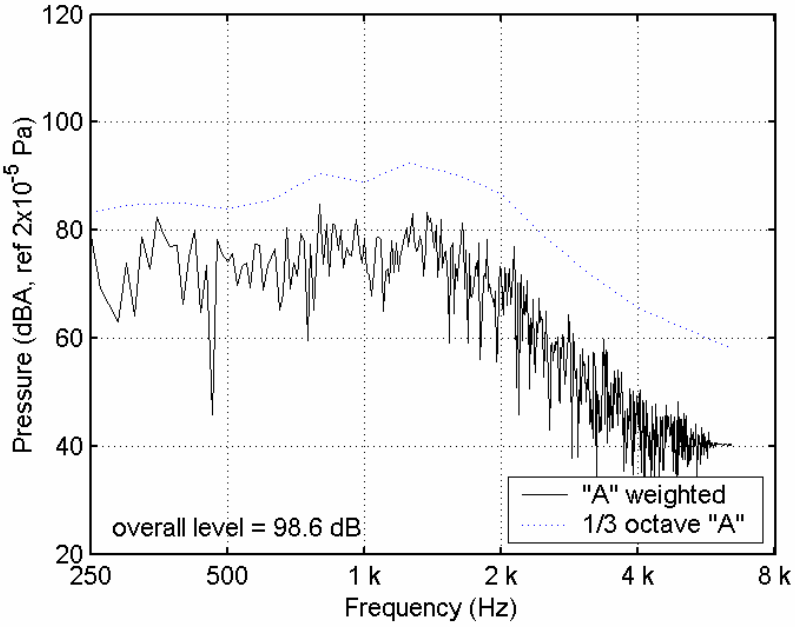

Figure 4.5.8 Time averaged PSD plot of noise collected over a longitudinal Astroturf finish (lead microphone, unthreaded tire, 13.4 m/s)

4.5.1.5 Comparison of Noise Data Obtained From Different Textures

Figure 4.5.9 shows a comparison of the frequency averaged data obtained for four different textures used in this study. It can be seen that the PSD for the Astroturf, broom transverse, and broom longitudinal are very similar, having a slightly higher sound pressure than the magnesium finish.

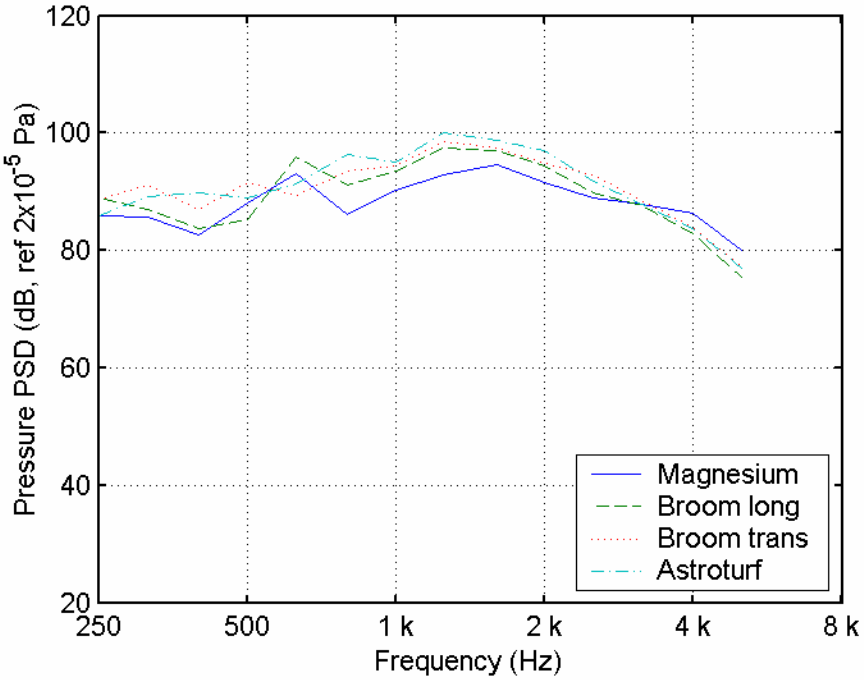

Figure 4.5.9 Frequency averaged PSD plot of noise collected over different surfaces (lead microphone, unthreaded tire, 13.4 m/s)

Figure 4.5.10 shows a time averaged PSD plot for different textured surfaces. The general trend on the data is the same as those observed in the frequency averaged. The magnesium trowel finish is the quietest of the textures presented in the noise data collected from the ungrounded surface study.

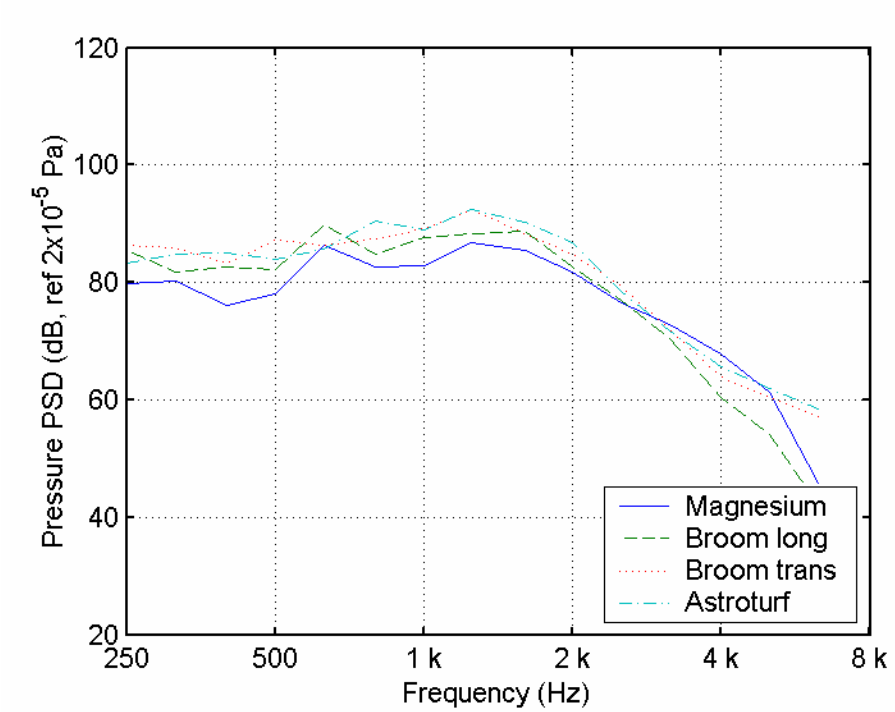

Figure 4.5.10 Time averaged PSD plot of noise collected over different surfaces (lead microphone, unthreaded tire, 13.4 m/s)

4.5.2 Transverse Tining with Different Geometries

In this section, power density spectra for different tine geometries are shown. Due to the spacing (30 cm) between the tines with different geometries, it was not possible to obtain frequency averaged data only time average data was obtained for this case. Frequency averaged data requires a test sample length of 1 m, and this sample has to have the same texture for the entire testing length. If the data is obtained by frequency averaged it is not possible to obtain noise data for a part of that sample. For the case time averaging, it is possible to extract the time pressure history of the sample length and by performing a FFT to the pressure history, is possible to obtain a PSD plot for a smaller section of the sample.

The data collected is presented as a black solid line and a $^1/_3$ octave filter is shown in the blue dotted line for ease of comparison. For the cases were multiple tines of the same geometry were tested an averaged of the $^1/_3$ octave filter data is presented as a thick solid red line. All the data presented is "A" weighted.

4.5.2.1 Beveled Edge Tines

The geometry of the beveled grinding blade is shown in Figure 4.3.7a, is important to note that the actual geometry of the tine will be slightly different from the geometry of the grinding blade. The difference in the geometry of the tine is due to vibrations of the grinder.

Figure 4.5.11 shows the power spectrum density plot collected over three tines grounded with the same blade. The average overall level for the three tines was 109.91 dB.

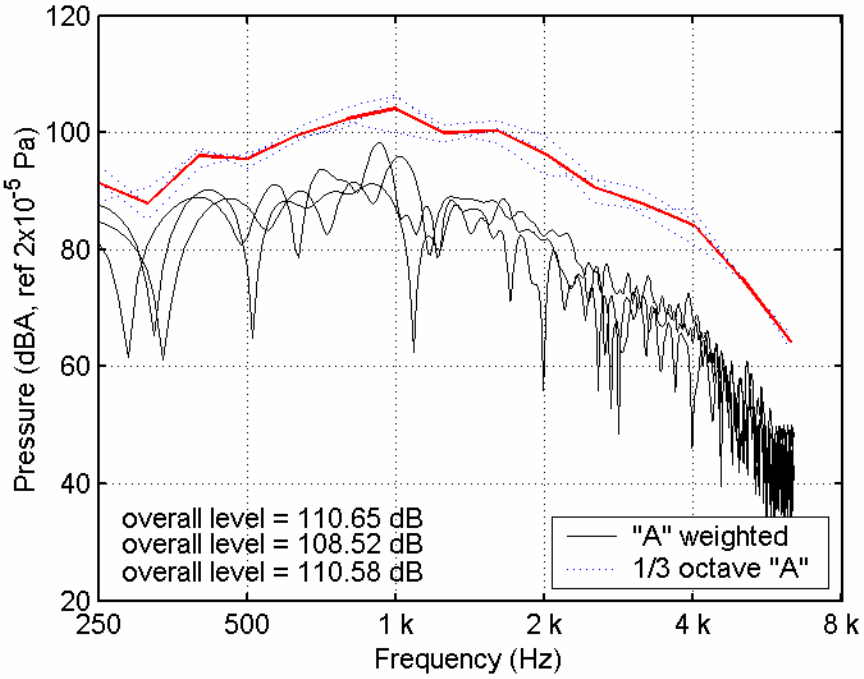

Figure 4.5.11 PSD plot of noise collected over 3 beveled tines on the TPTA using time averaging (lead microphone, unthreaded tire, 13.4 m/s)

4.5.2.2 Tines with Rounded Edges

The geometry of the rounded edge grinding blade is shown in Figure 4.3.7b. Figure 4.5.12 shows the power spectrum density plot collected over three tines grounded with the same blade. The average overall level for the three tines was 110.96 dB.

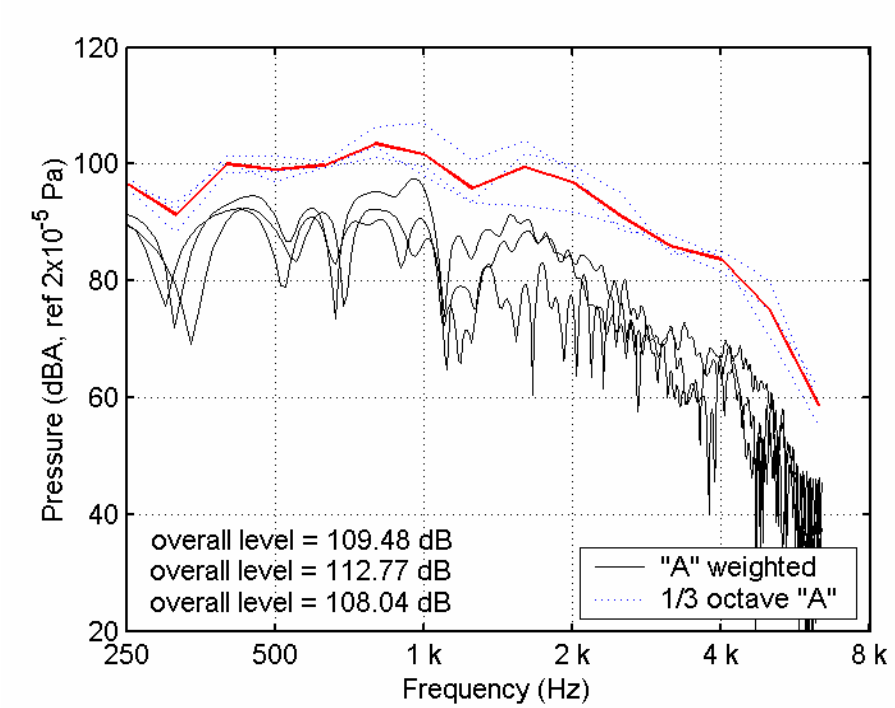

Figure 4.5.12 PSD plot of noise collected over 3 circled edge tines on the TPTA using time averaging (lead microphone, unthreaded tire, 13.4 m/s)

4.5.2.3 Tines with Different Widths

A typical geometry of a square tine is shown in Figure 4.3.7c, is important to note that the width of rectangular tines was changed. Figure 4.5.13 shows the PSD plot for ground tines with different widths. It can be seen that higher pressure level is associated with wider tines. The overall pressure levels for the different width are presented in the textbox. Is important to note that this data was collected over the same concrete sample by first starting with a ground surface and then adding a tine. The tine width was progressively increases without modifying any of the data acquisition settings. Figure 4.5.14 shows a relationship between the overall pressure level and the width of the tine.

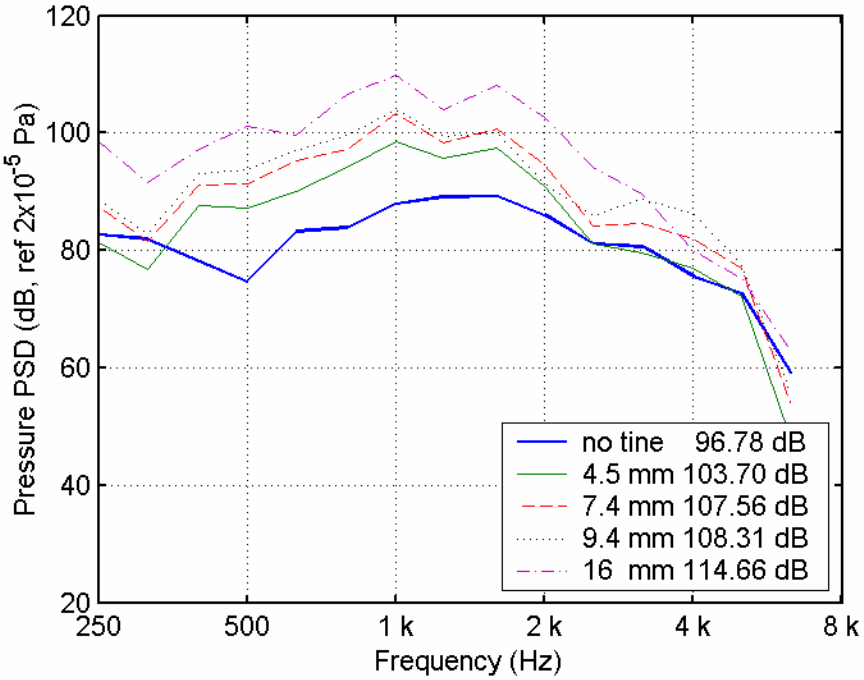

Figure 4.5.13 Time averaged PSD plot of noise collected over square tines with different widths; the overall noise level is shown next to the label (lead microphone, unthreaded tire, 13.4 m/s)

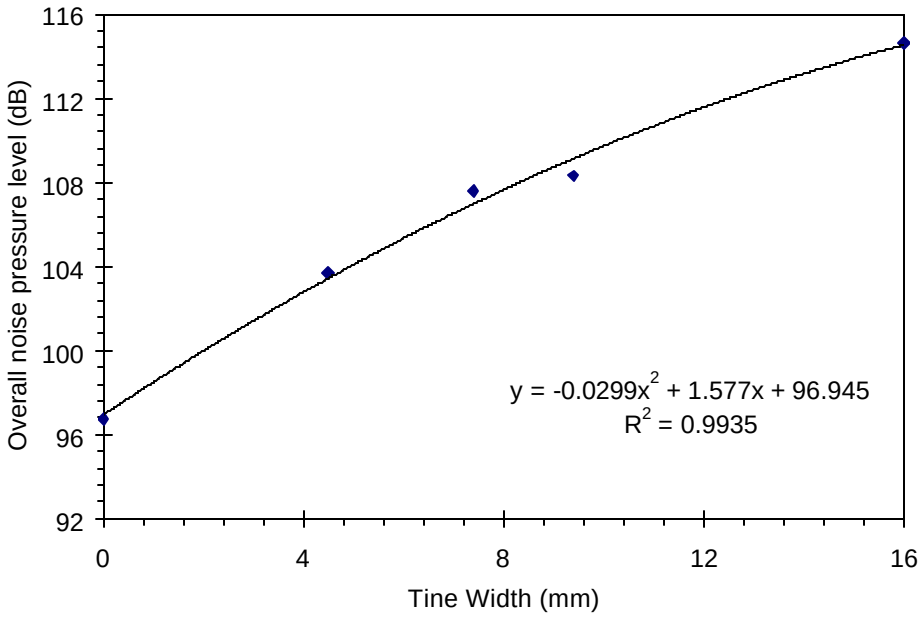

Figure 4.5.14 Relationship between overall noise level and the width of the tine

4.5.2.4 Transverse Uniformed Spaced Tining

Surfaces with transverse uniformed spaced tining were tested to assess the influence of residual vibration of previous tine over the next one. This residual vibration will generate louder noise as it add up over several tines. The data was collected using time averaging technique. Figure 4.5.15 shows the PSD plot of a series of tines with a width of 4.5 mm uniformly spaced at 25 mm. By comparing this data to the one obtained for a single tine (Figure 4.5.13) an increase in the overall pressure level of 3.05 dB is observed.

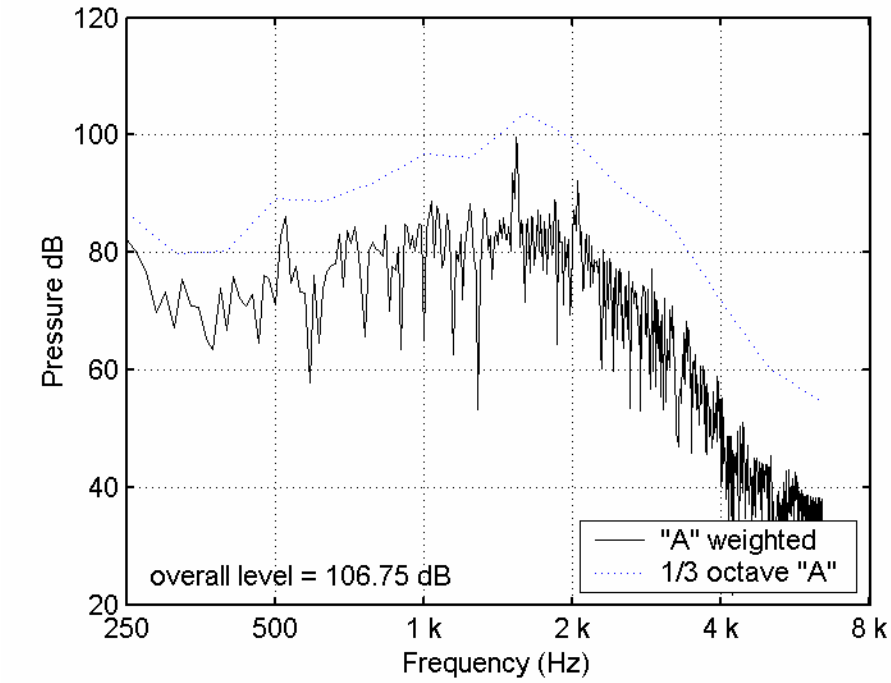

Figure 4.5.15 Time averaged PSD plot of noise collected over uniformly spaced tines (lead microphone, unthreaded tire, 13.4 m/s)

Figure 4.5.16 shows a comparison between a single tine and a series of tines with 25 mm separation. It can be seen that this increase in the overall pressure level previously mention is mainly due to an increase in the pressure level in frequencies between 1.2 kHz and 3 kHz. In addition, both PSD plot are very similar for frequencies below 1.2 kHz. This implies that tine and tire performance at low frequencies may be assessed by studying just a simple tine.

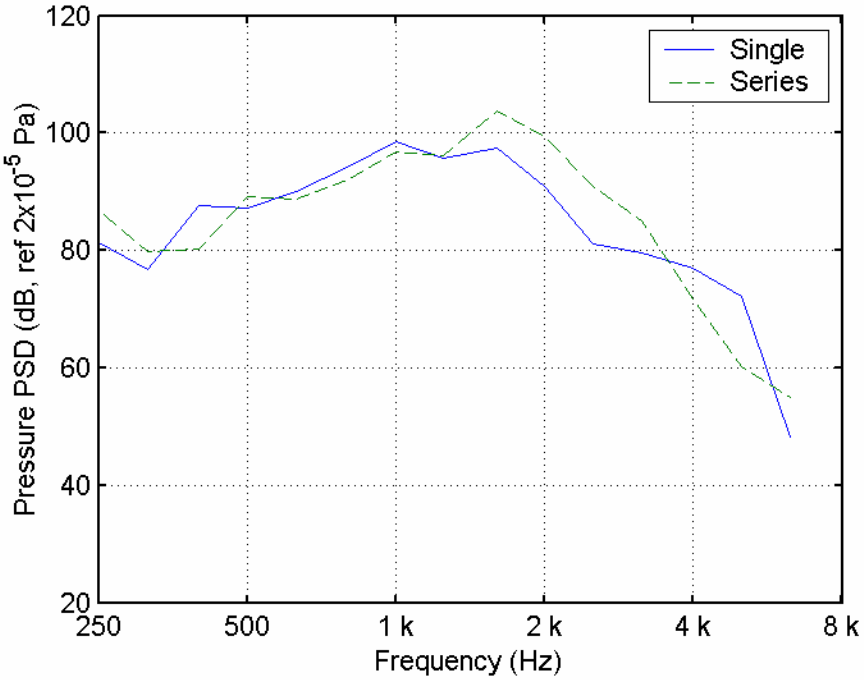

Figure 4.5.16 Comparison of pressure levels for a single tine and a series of uniformly spaced tines (time averaged data) (lead microphone, unthreaded tire, 13.4 m/s)

4.6 Chapter Conclusions

After performing tests on textured surfaces like Astroturf, broom and magnesium trowel finish and grounded tines using the TPTA, it can be concluded that:

Different types of textures will produce different noise level as the orientation and the depth of the texture changes.

That there is no significant influence of the tine edge geometry on the noise spectrum shape and the overall noise level. Increasing tine width of square tines increases the overall noise level without a noticeable impact on the shape of the noise spectrum. There appears to be a relationship between tine width and overall noise. The influence of having a series of tines in comparison with a single tine can only be seen at frequencies higher than 1 kHz.

The next chapter provides a description of surface characterization techniques. These techniques are used to characterize the surfaces discussed previously in order to further describe them. Stress-noise modeling is later performed using the obtained surface profile as an input for the modeling.

CHAPTER 5 TECHNIQUES TO CHARACTERIZE VARIOUS SURFACES

In this chapter, the techniques used for surface texture characterization are described, the data collected from these techniques is analyzed, and the results and implications are discussed. The collected surface texture data is input into the model described in CHAPTER 3 and used to obtain the contact stress distribution and obtain a noise power density spectrum for each of the different surfaces that could be compared to the data obtained in CHAPTER 4.

5.1 Sand Patch Method

A traditional method for obtaining texture depth is the sand patch method (ASTM-E965). In this method, a known volume of uniformly sized glass sand is poured on a dry surface of the pavement. The sand is distributed evenly over the surface of the pavement until a circular patch of uniform thickness is formed. To determine the average texture depth, the known volume of sand is divided by the area of the patch. It should be noted that the average texture depth only reflects macrotexture characteristics of the pavement and disregards microtexture. The traditional way to account for microtexture of the pavement surface is to measure frictional characteristics.

5.2 Non-Contact Laser Profilometer

The laser profilometer [Longman and Weiss 2002], shown in Figure 5.2.1, was developed to obtain a 3D profile of the surface. The profilometer consists of a table that the specimen can be placed on and a set of movable arms that hold the non-contact laser.

The arms that hold the laser are connected to a gear system and to a stepper motor, which allows controlled movement. The two arms move perpendicular to each other. The maximum resolution provided in the X-Y direction of the mechanisms is 200 spaces per inch (0.127 mm between spaces). To facilitate more rapid measurement, there are two lasers mounted on the moving platform. The distance between lasers can be adjusted depending on the size of the sample. The depth range of the laser profilometer is 5 mm with a micron resolution. The profilometer is connected to a computer that controls the speed of the laser travel, the intervals between measurements, and records the obtained data. The data is collected as a text file and later imported to a spread sheet for analysis.

The slabs with various surface textures were placed over a leveling plate (Figure 5.2.2) under the scanning table and leveled using the leveling screws. The height of the slabs was adjusted using the leveling screws to be within the optimal range of the laser.

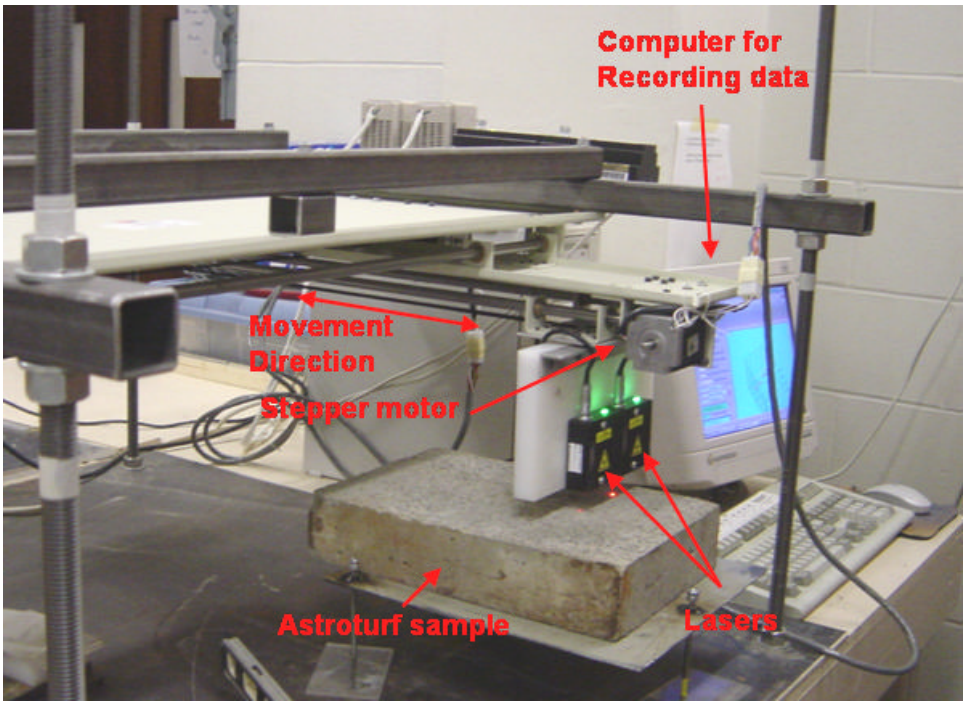

Figure 5.2.1 Laser profilometer scanning an Astroturf finished surface

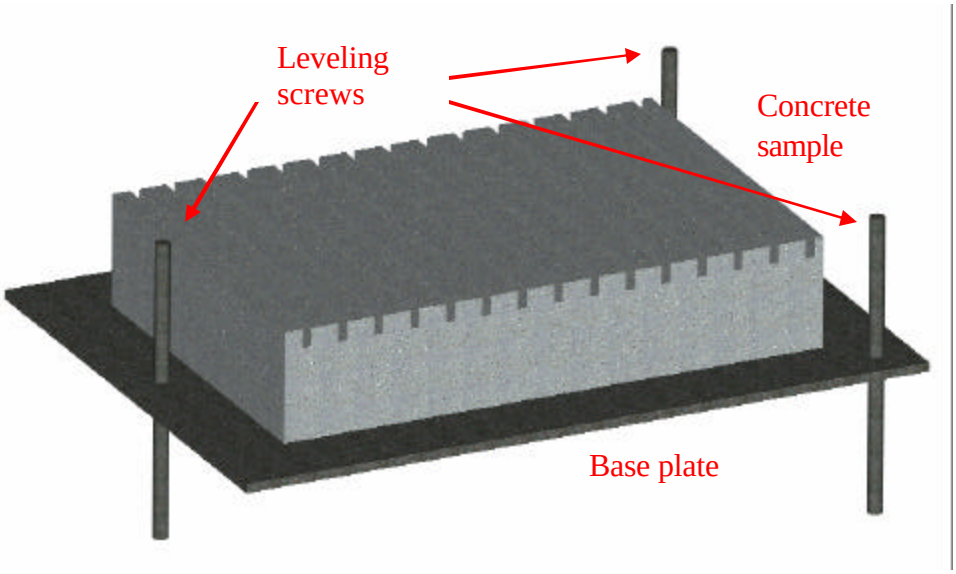

Figure 5.2.2 Schematic of the texture slab on a leveling plate

Table 5.2.1 shows a summary of different surface textures that were prepared in this study and scanned by laser profilometer. These textures were scanned using the maximum resolution of the laser profilometer; this resolution was 0.127 mm on longitudinal direction and micron level on the height direction. The textures were scanned in two dimensions to generate the data for use with the pressure distribution program. Since the resolution needed for the stress distribution program is 0.1 mm between each data point it was necessary to perform a cubic interpolation to improve the resolution.

Table 5.2.1 Summary of surfaces scanned with laser profilometer

Type of surface	Profile direction	Number of locations
Tines preformed infresh concrete	Transverse	4
Astroturf	Longitudinal	7
Magnesium trowel	Longitudinal	8
Tines cut into the hardened concrete	Transverse	6
Broomed	Longitudinal	6
Broomed	Transverse	8

5.2.1 Mathematical leveling of surfaces

Since the leveling of the slabs relative to the scanning head was done manually using a bubble level, a correction was performed individually to each set of data to adjust for any inclination on the surface texture. The correction was done by obtaining a tendency line for the original data and subtracting (on a point by point basis) the trend line from the original data. Figure 5.2.3 shows the original data obtained from the laser profilometer. A trend line was fitted to the original data and used to adjust the data. This adjustment was made by subtraction of the trend line to the original data on a point by point basis. The resultant profile was used as the input for stress-noise model.

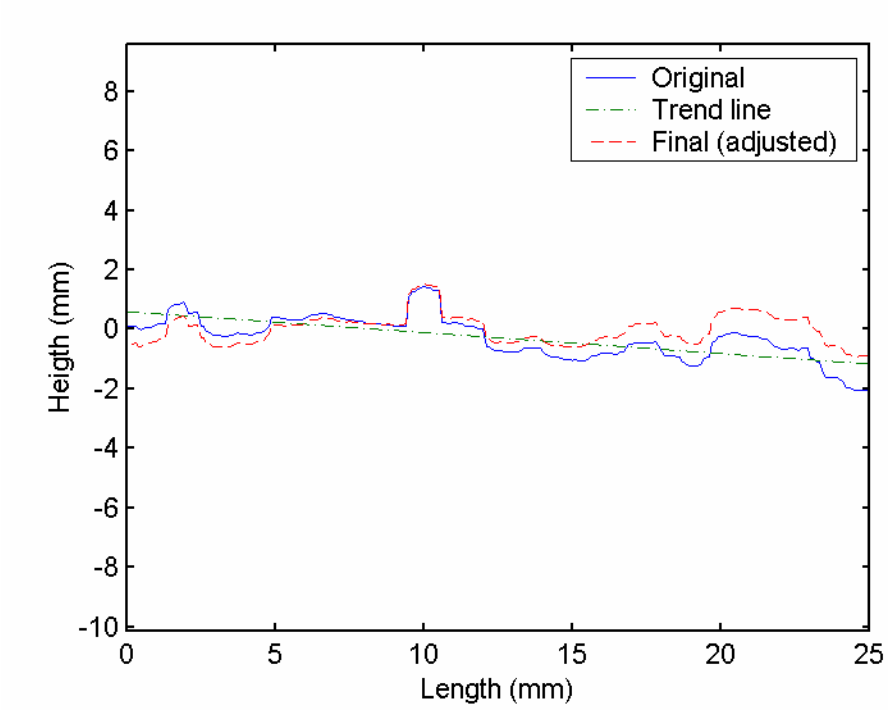

Figure 5.2.3 Mathematical leveling o scanned surfaces

5.3 Typical profiles of scanned surfaces

Figures 5.3.1 through 5.3.4 show typical profiles for the different surface textures.

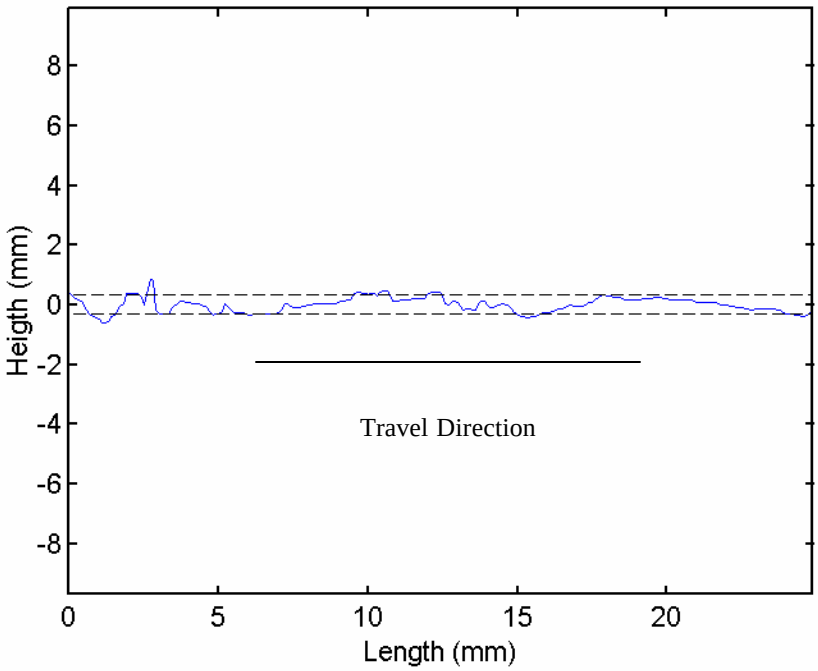

Figure 5.3.1 Typical astroturf texture profile

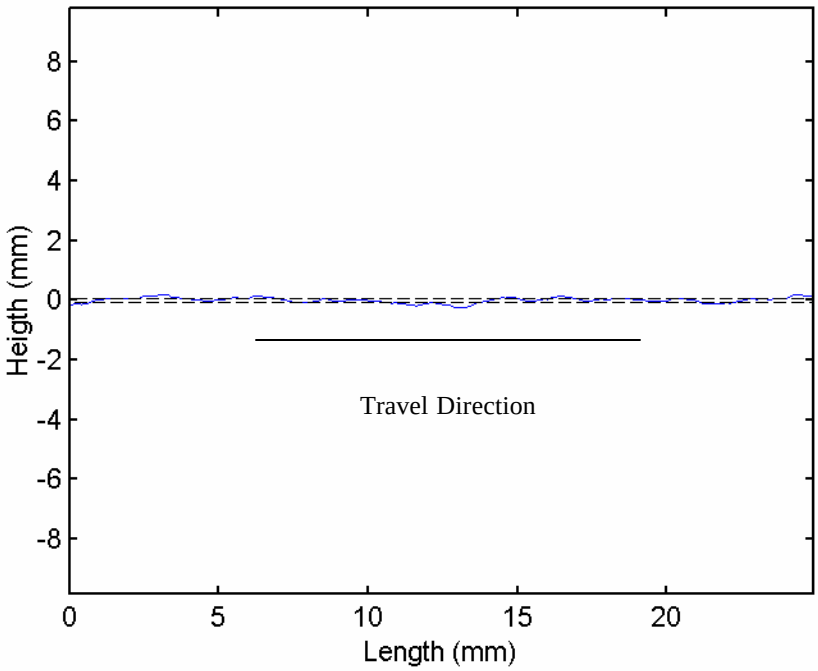

Figure 5.3.2 Typical magnesium trowel finish profile

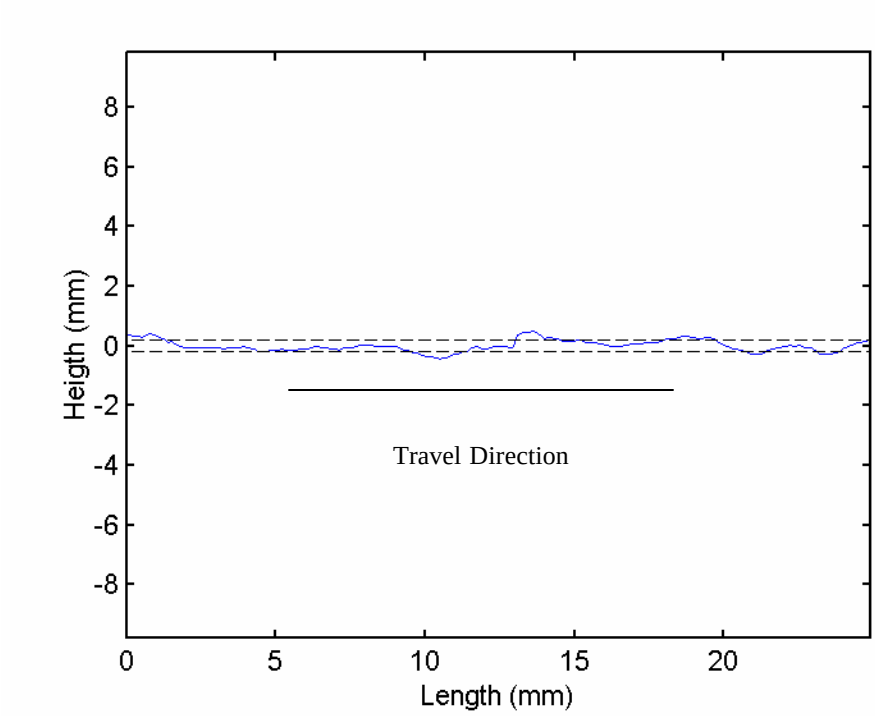

Figure 5.3.3 Typical longitudinal broom texture profile

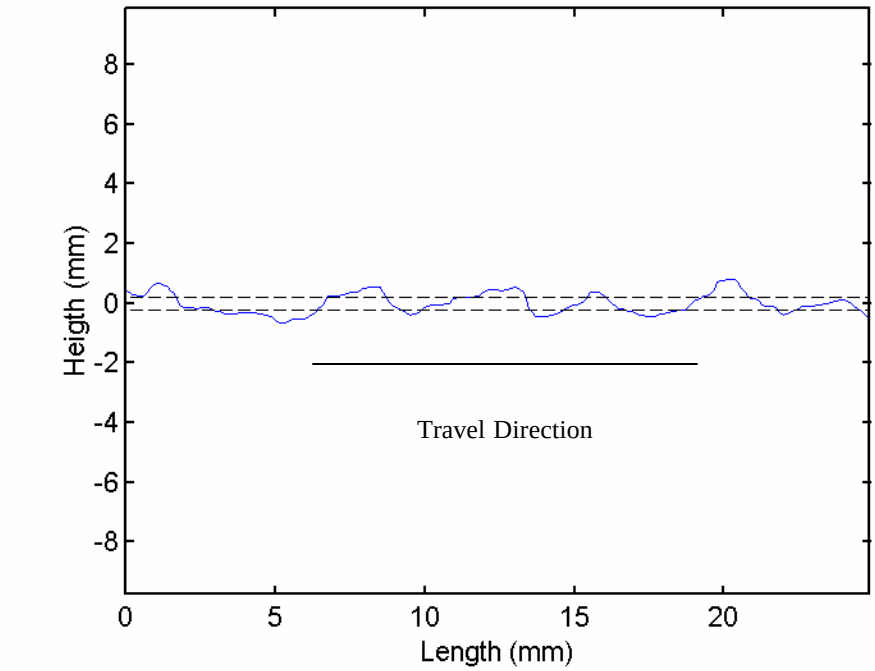

Figure 5.3.4 Typical transverse broom texture profile

5.4 Statistical Evaluation of Data from Different Surface Textures

The mean and standard deviation of the depth were obtained for each texture type as a way to characterize the surface. The mean depth of a surface type was obtained by averaging the average depth for each of the surface scans on the same surface type. The average depth for each surface scan was obtained by averaging the absolute values of the texture heights and multiplying it by 2.

Table 5.4.1 shows the mean depth and standard deviation values obtained from the different textures. It can be seen that, as expected, the Astroturf texture has the highest mean depth having a value of 0.64 mm and highest standard deviation of 0.23 mm. The second highest mean depth was for the transverse broom texture (0.45 mm and a standard deviation of 0.18 mm). The third highest values were for the longitudinal broom texture (mean depth of 0.35 mm and a standard deviation of 0.13 mm). It is important to note that the transverse and longitudinal broom textures data were obtained from the same surface by rotating the slab by 90°. The difference in the mean depth values occurred because for the longitudinal texture the laser was usually scanning a crest or a valley of the texture in a constant direction without switching between crests or valleys as in the transverse case. The mean depth of the transverse broom texture is recorded form the lowest valley point to the highest crest point, while the longitudinal broom texture records form the deepest to the highest point within a crest or valley. The lowest mean depth was for the magnesium trowel finish (0.12 mm and a standard deviation of 0.05 mm). The grooved and grounded tines data was not available due to the limiting 5 mm depth range of the laser profilometer.

Table 5.4.1 Summary of mean depths for different textures

Type of surface	Mean depth (mm)	Standard deviation (mm)
Astroturf	0.64	0.23
Magnesium trowel	0.12	0.05
Broom longitudinal	0.35	0.13
Broom transverse	0.45	0.18

5.5 Stress and Noise Modeling of Scanned Surfaces

Each of the scanned surfaces was modeled to calculate the stress distribution and power spectrum density for the stress distribution. As previously discussed in section 5.2 the surface texture data was interpolated to obtain the desired 0.1 mm resolution before the profilometer data was used as an input for the model. The input for the modeling was a vector containing the depths values of 250 points that were separated by the distance of 0.1 mm one from another.

The power density spectrum was obtained for each of the measured texture profiles. To better characterize the stress distribution the modeling was done for different scanning locations on the same surface. For each of these scanning locations a profile was obtained. Since each of these profiles was different to every other, it was necessary to obtain a power density spectrum for each of these profiles. In order to better describe the sound generation characteristics of each surface, an upper and lower pressure range together with the average pressure will be obtained for each texture type.

Stress-noise modeling was not performed on the grooved and ground tines because the stresses did not concentrate at the edges of the tine. The stress distribution was the same as for a surface without the tines (magnesium trowel finish). This happened because the stress was concentrated on the surface irregularities.

5.5.1 Astroturf Texture

Figure 5.5.1 shows the surface stress distribution for a typical Astroturf texture and its corresponding power spectrum density plot. Figure 5.5.2 is composed of the average of seven PSD obtained from the stress distributions of the successful surface scans obtained form the laser profilometer. The upper and lower limits look very similar and the pressure difference between them is approximately 5 dB.

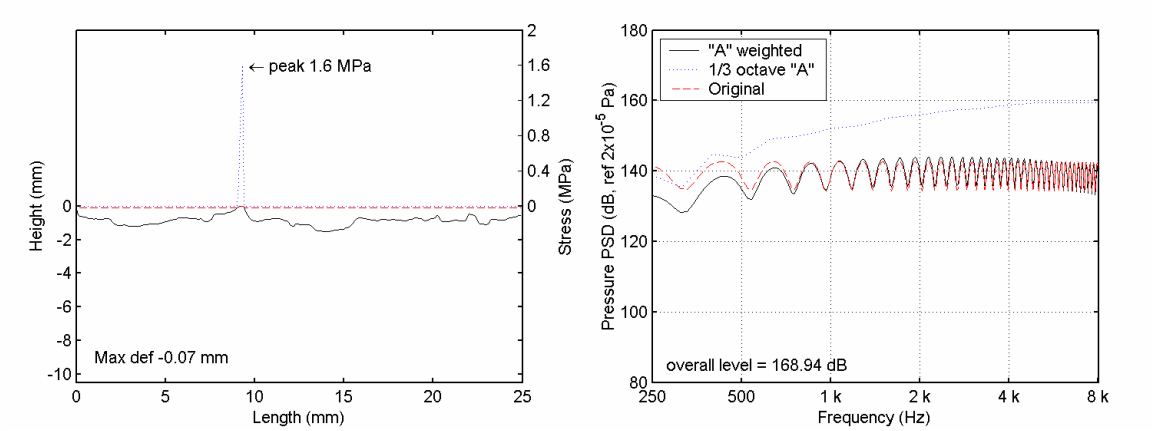

Figure 5.5.1 Typical stress distribution and modeled PSD plot for Astroturf texture

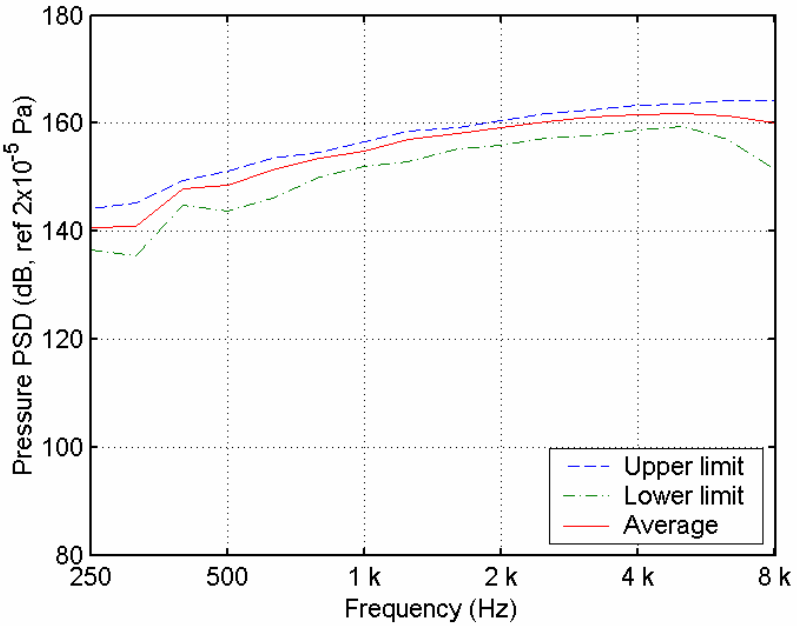

Figure 5.5.2 PSD plot of noise model for a longitudinal Astroturf finish showing upper and lower limits for different sections on the texture

5.5.2 Magnesium Trowel

Figure 5.3.3 shows the stress distribution and its corresponding power spectrum density plot for a typical surface texture of a magnesium trowel finish. Figure 5.5.4 is composed of the average of eight modeled power density spectrums obtained using the laser profilometer. The upper and lower limits for this case have different profiles as

compared to the Astroturf case. The pressure difference is approximately 6 dB for higher frequencies and around 15 dB for lower than 1 kH frequencies.

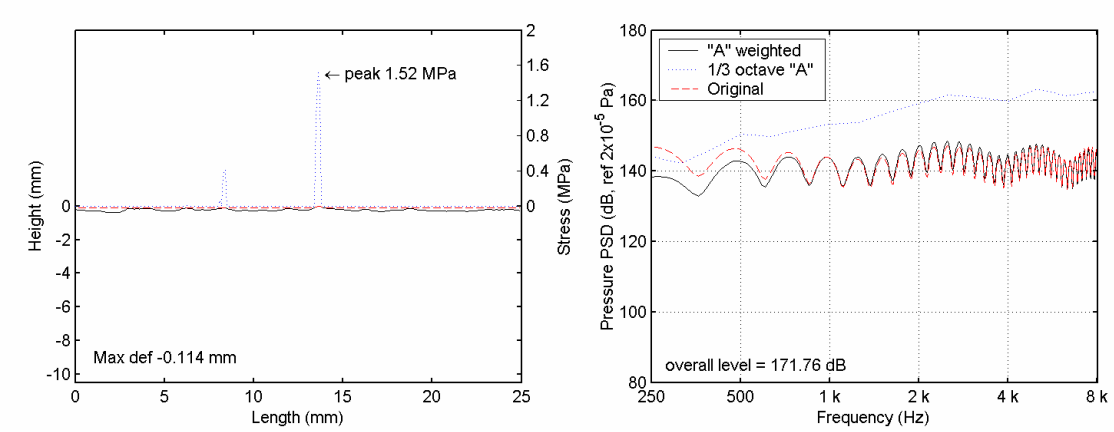

Figure 5.5.3 Typical stress distribution and modeled PSD plot for magnesium trowel finish

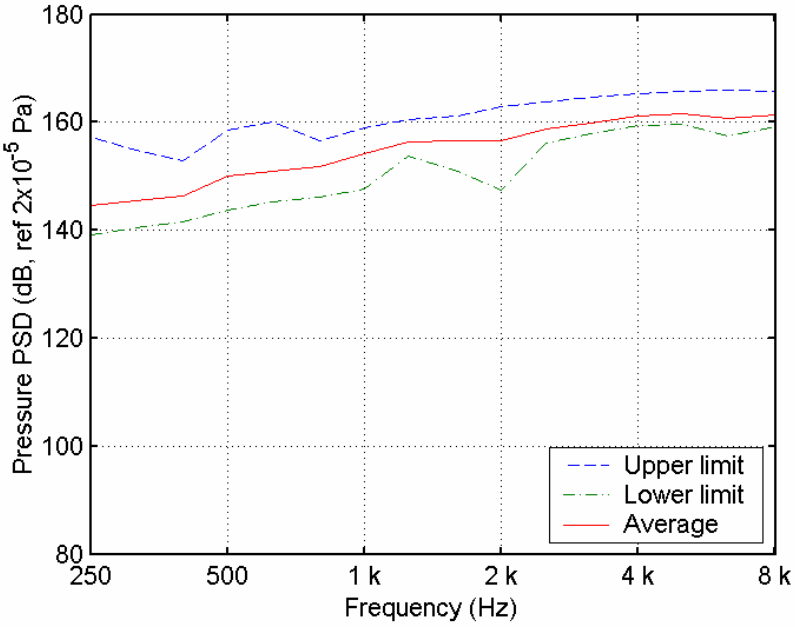

Figure 5.5.4 PSD plot of noise model for a magnesium trowel finish showing upper and lower limits for different sections on the texture

5.5.3 Broom Longitudinal

Figure 5.5.5 shows the stress distribution and its corresponding power spectrum density plot for a typical broom longitudinal surface texture. Figure 5.5.6 is composed of

the average of six modeled power density spectrums obtained using the laser profilometer. The upper and lower limits for this case look similar and the pressure difference is approximately 6 dB. The averaged PSD plot for the longitudinal broom texture looks similar to the one for the Astroturf texture but has a higher pressure difference form the minimum to the maximum limits.

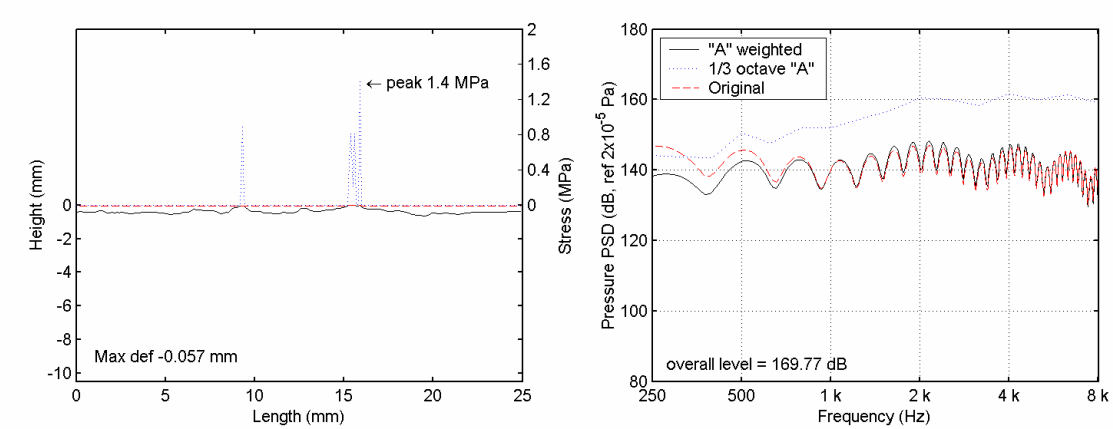

Figure 5.5.5 Typical stress distribution and modeled PSD plot for longitudinal broom texture

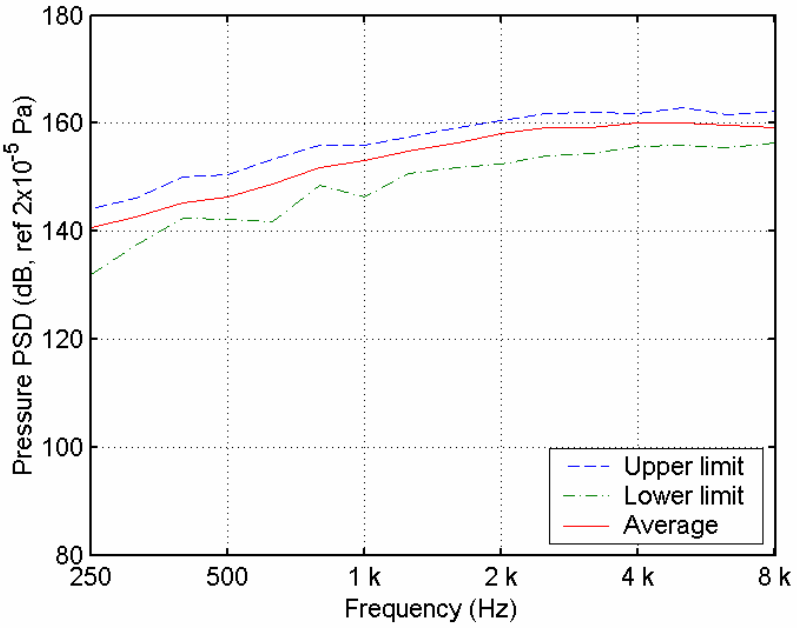

Figure 5.5.6 PSD plot of noise model for a longitudinal broom finish showing upper and lower limits for different sections on the texture

5.5.4 Broom Transverse

Figure 5.5.7 shows the stress distribution and its corresponding power spectrum density plot for a typical broom transverse surface texture. Figure 5.5.8 is composed of the average of eight modeled power density spectrums obtained using the laser profilometer. The upper and lower limits are not similar and the pressure difference for high frequencies is approximately 4 dB and 20 dB for lower frequencies.

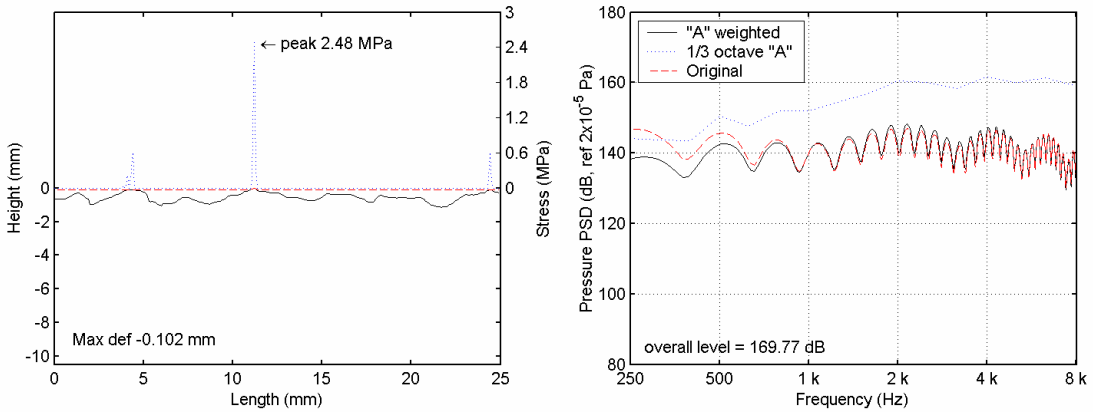

Figure 5.5.7 Typical stress distribution and modeled PSD plot for transverse broom texture

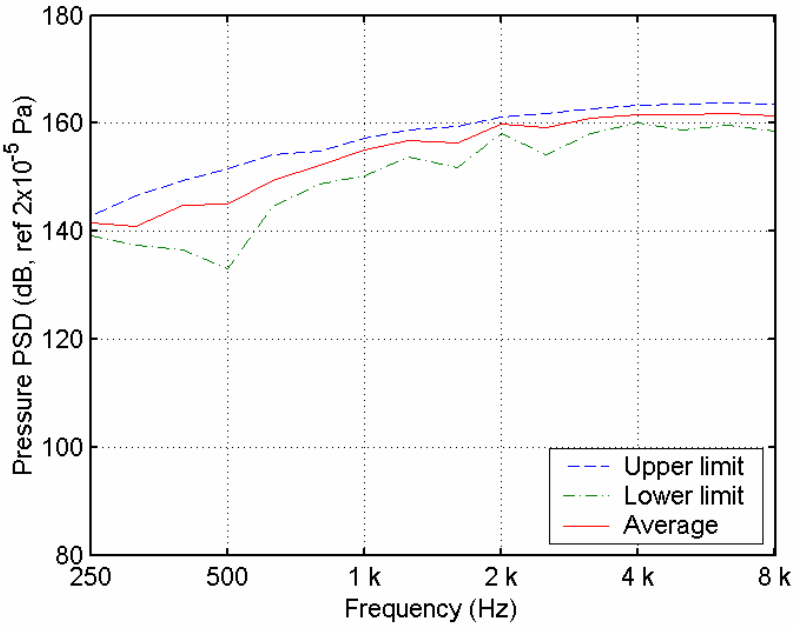

Figure 5.5.8 PSD plot of noise model for a transverse broom finish showing upper and lower limits for different sections on the texture

5.6 Chapter Conclusions

Different surface textures were scanned using the laser profilometer in order to obtain a mathematical description of the surface profile. The obtained profiles were used as an input for the stress-noise modeling program. After performing the modeling, it can be seen that rougher textures will produce power density spectrums with less variation as it is shown for the cases of the Astroturf and the broom transverse. This happens because usually for the model length of the texture as single stress concentration point appears for the rougher textures in comparison to multiple stress concentration point for smoother textures.

On the next chapter, a transfer function is proposed in order to link the stress-noise modeling to the data obtained by real size testing on the TPTA. The transfer functions are obtained using data from CHAPTER 3, CHAPTER 4, and CHAPTER 5.

CHAPTER 6 LINKING SURFACE MEASUREMENT WITH NOISE PREDICTION MODEL

In order to link the data collected on the TPTA to the modeling predicted it is necessary to correct for certain differences. These differences can occur for several reasons. First, it is necessary to understand that the sound pressure calculated by the model was calculated on the tire surface not on the air. Second, the sound pressure calculated by the model was at a different location than the measured sound; because the sound calculated was exactly at the location were the sound in generated and the measured sound has to travel the distance between the source and the microphone. Third, the noise spectrum generated by the contact stress modeling only takes into account the input force action on the tire, disregarding the radiation efficiency of the tire and the influence of tire dynamics that will modify the output noise. Is important to note that each of these transfer functions will be valid for a certain speed, tire type, inflation pressure, tire loading, and whether conditions in general. The procedure to correct the model noise was to generate a transfer function that can be multiplied to the output of the mathematical model to obtain the noise expected.

As previously discussed, the use of a transfer function will enable to improve the perditions from the mathematical model by taking into account aspects of the tire and the surface texture that the model was not design to do. There are some limitations in the use of a transfer function to relate the stress-noise modeling to the data obtained from the TPTA. One of the main limitations is that the radiation efficiency of the tire is different for different locations around the tire, and a transfer function should be provided for each of these locations.

6.1 Data Generation and Collection

The data used to obtain the transfer functions was collected and generated in three different scenarios:

i. Data modeled from tines discussed on section: 3.2 Modeling of Various Surfaces Textures and Tine Geometries. This data was generated form surfaces that were found to provide some noise reduction in the model. This textures and geometries could not be scanned on the laser profilometer due to its limitations on depth range. There was no variability on these data because it was modeled from surfaces with no variability on the geometry.

ii. Data modeled from surface textures scanned with the laser profilometer as discussed on section: 5.5 Stress and Noise Modeling of Scanned Surfaces. These data was obtained from averaging several power density spectrum plots for each surface texture. The texturing of these surfaces was done with the same procedure as the texturing for the samples of the TPTA.

iii. Data obtained by testing on the TPTA as discussed on 4.5 TPTA Test Results. These data is divided by the data obtain in (i) or (ii) depending which one was available having always preference to (ii), because it will conserve the natural randomness of the texture.

6.2 Transfer Functions

The transfer functions were calculated using the $^1/_3$ octave filtered data because is less susceptible to small chances in frequency. Equation 5.1 shows how the transfer functions were obtained.

$$TF = \frac{measured\_spectrum}{modeled\_spectrum} \tag{5.1}$$

The transfer functions were obtained by dividing the measured spectrum of the sound pressure (Pa) by the modeled spectrum of the contact stress distribution (Pa). It is important to note that the division has to be done in a non-referenced scale. In order to do that is necessary to transform the decibels into Pa before performing the division.

Sections 6.2.1 thru 6.2.3 show the different transfer functions obtained for the entire set of pavement samples that where modeled.

6.2.1 Textured Pavements

Figure 6.2.1 shows the power density spectrums that were used to obtain the transfer functions for texture pavements. Figure 6.2.1a illustrates the PSD plots of the textured surfaces obtained form testing on the TPTA as described on 4.5.1 while Figure 6.2.1b illustrates the PSD plots of the textured surfaces obtained form stress-noise modeling of the profiles obtained with the laser profilometer as described on 5.5 dividing these creates the transfer function.

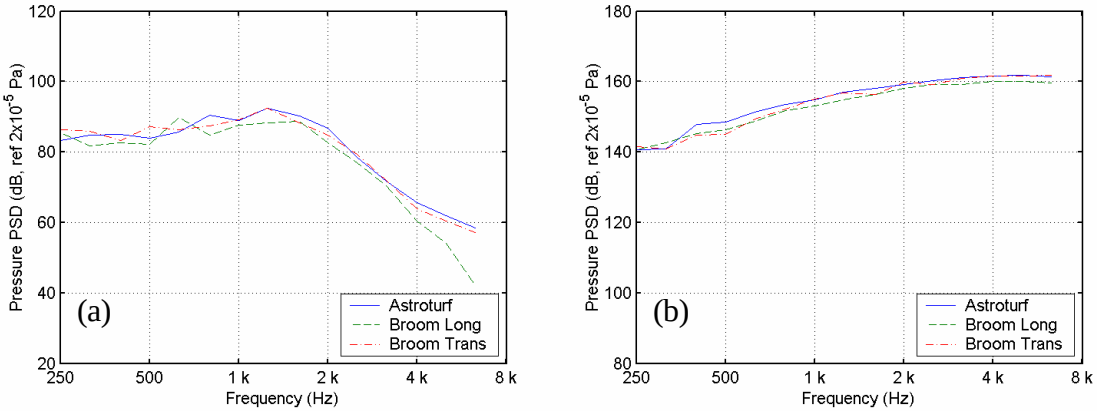

Figure 6.2.1 Measured (a) and modeled (b) spectrums for different surface texturing techniques

The computed transfer functions for the textured pavements are shown in Figure 6.2.2. A strong correlation between the three texture transfer functions. This correlation is shown as the three transfer functions for the different textures have the same ratio at different frequencies. Is important to note that these correlations are due to strong similarities among the data recorded on the TPTA and the computer model of the scanned surfaces.

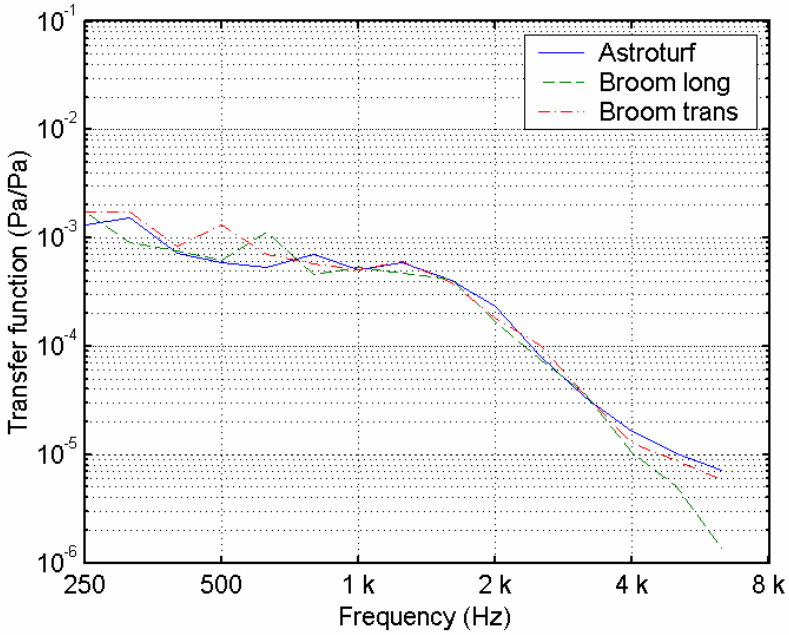

Figure 6.2.2 Transfer functions obtained for textured pavements

6.2.2 Tine Edge Geometry

Figure 6.2.3 shows the power density spectrums of the data used to obtain the transfer functions for tines with special edge geometries. Figure 6.2.3a illustrates a PSD plot obtained from testing on the TPTA for tines with special edge geometries as described on 4.5.2 while Figure 6.2.3b illustrates the PSD plots of molded profiles obtained from sections 3.2.3 and 3.2.4 dividing these spectrums generates the transfer function for tines with special geometries.

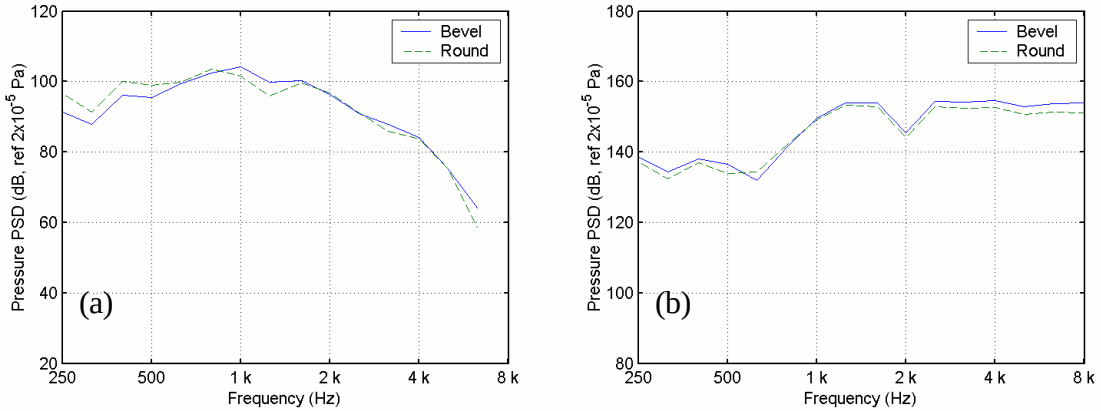

Figure 6.2.3 Measured (a) and modeled (b) spectrums for tines with different geometry

Figure 6.2.4 shows the transfer functions for the pavements with different tine geometries. There is a correlation between this transfer functions. This correlation is mainly due to the separation of the main stress concentration points in the mathematical model that was 9 mm, the stress concentration points have similar spacing that generates as similar frequency response.

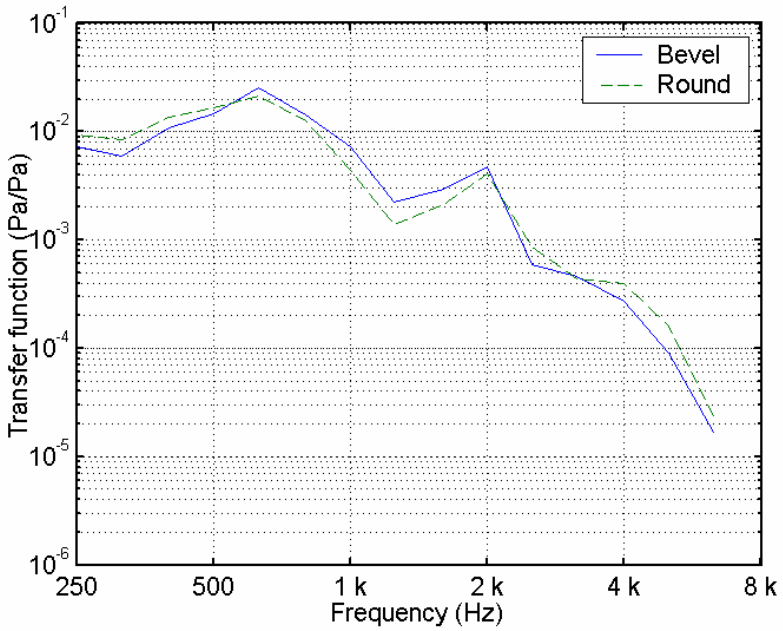

Figure 6.2.4 Transfer functions obtained for tines with different geometry

6.2.3 Tine Widths

Figure 6.2.5 shows the power density spectrums for different tine widths that were used to calculate the transfer functions. Figure 6.2.5a illustrates a PSD plot obtained from testing on the TPTA for square tines with different widths as described on 4.5.2.3 while Figure 6.2.5b illustrates the PSD plots of molded profiles obtained from section 3.2.1 dividing these data generates the transfer function for tines with different widths.

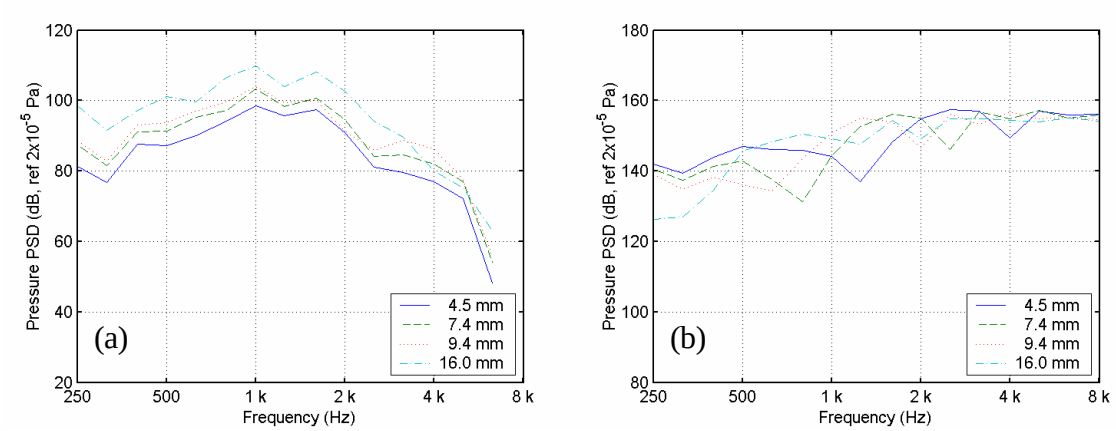

Figure 6.2.5 Measured (a) and modeled (b) spectrums for tines with different widths

Figure 6.2.6 shows the transfer functions for different tine widths. As it is shown, there is no correlation between these transfer functions. The lack of correlation is due because the mathematical model produces a change of frequency as the width of the tine changes, and the measured data on the TPTA produces an increment in sound pressure level, without having any change of frequency.

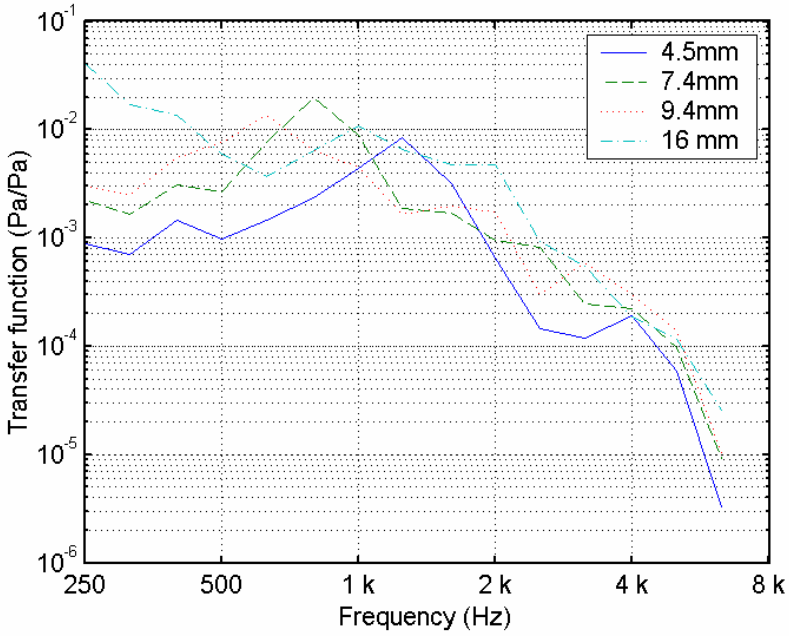

Figure 6.2.6 Transfer functions for square tines with different widths

6.2.4 Comparing Transfer Functions for Different Surfaces and Textures

Figure 6.2.7 shows a comparison between the different transfer functions for tines. As it is shown, there is lower variation in the ratio at higher frequencies than at lower frequencies. There appears to be no significant correlation between the tines with different widths and the tines with different geometries. As previously discussed, the lack of correlation is due to the fact that the model changes the modulation frequency of the PSD plots as the location and distance between the main stress concentration points changes while the measured data has a tendency to conserve the modulation but changes the level.

A maximum, minimum, and average of the tine transfer functions is shown in Figure 6.2.8, here is shown that the average of the transfer functions lies between the maximum and minimum.

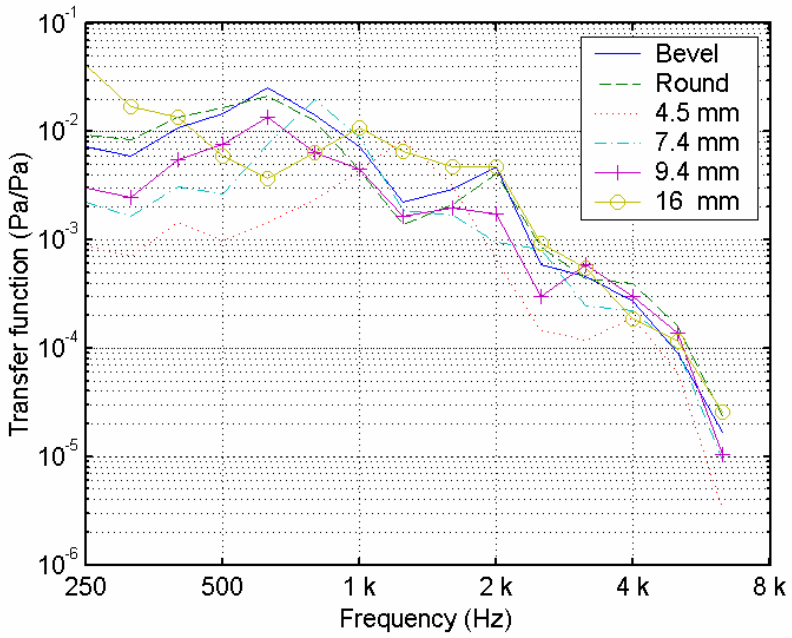

Figure 6.2.7 Transfer functions for different tine geometries

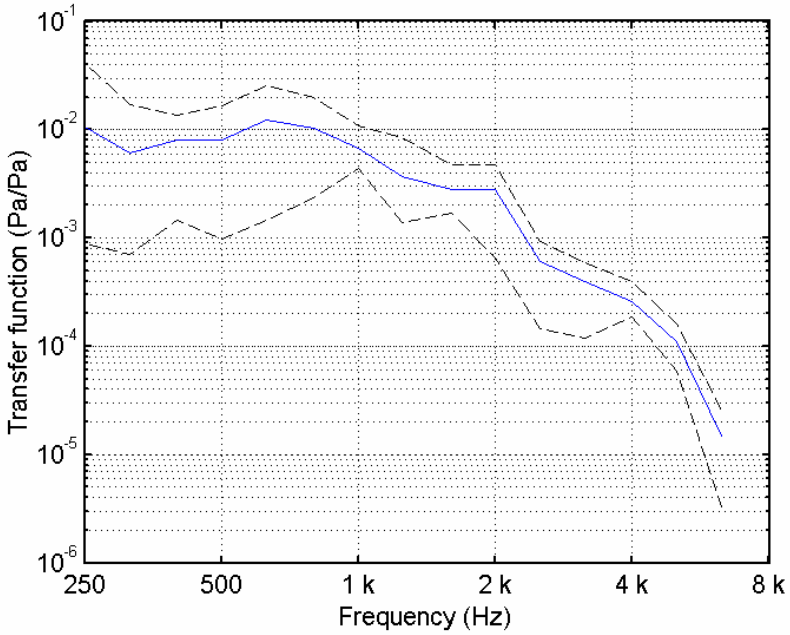

Figure 6.2.8 Average lower and upper limits for tines

Figure 6.2.9 shows the complete set of transfer functions including tines and textures. Here is shown that there is no correlation between the tined surfaces and the texture surfaces, having the texture surfaces a lower ratio in comparison to all of the tined surfaces. Figure 6.2.10 shows the average, maximum, and minimum limits of the transfer functions for all the surfaces and tines.

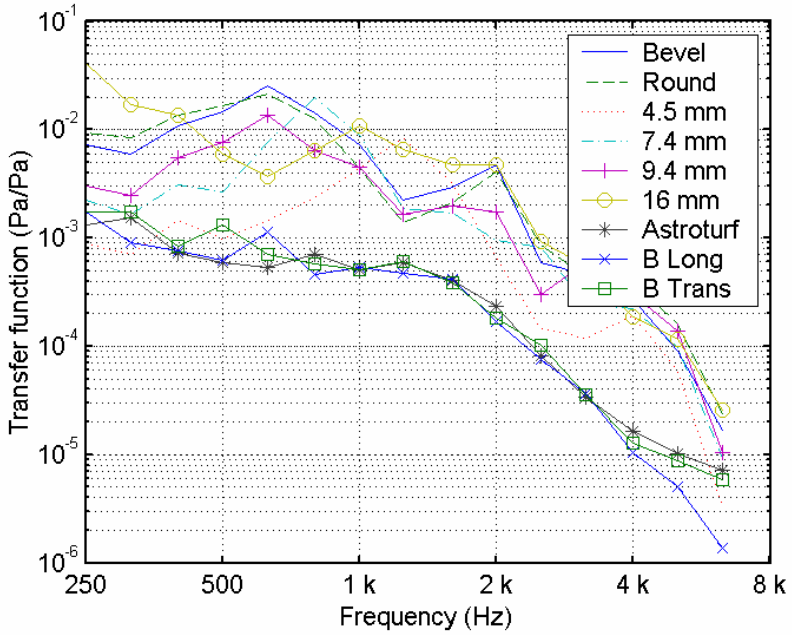

Figure 6.2.9 Transfer functions for tines and textures

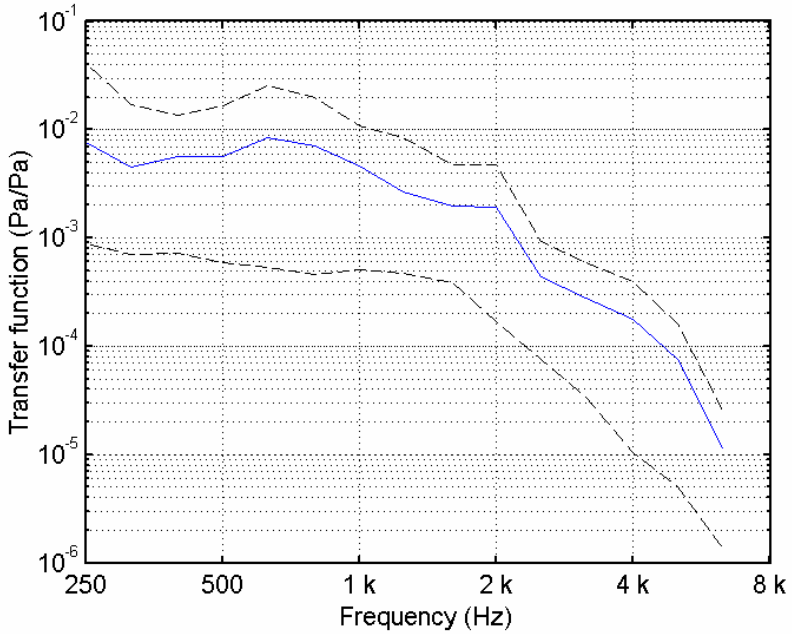

Figure 6.2.10 Average upper and lower limits for the transfer functions

6.3 Chapter Conclusions

A transfer function was calculated for each of the surfaces and types of tines that were tested on the TPTA. These transfer functions were obtained by dividing the measured spectrum obtained by testing on the TPTA by the modeled input spectrum obtained from stress modeling. In order to assess the validity of this transfer function it was necessary to obtain a transfer function of each type of surface or tine and compare them. The validity of the transfer function could be corroborated if all the transfer functions had the same shape and level.

It is clear that the use of transfer functions will have a limited validity. While it is obvious that there is a tendency on the transfer functions to be constant for cases which are similar. There is variability of that tendency.

The fact that the transfer functions have a high variability does not indicate that the use of contact stress modeling is inappropriate as a technique to model noise generation. This only indicates that there is more than one input force acting on the tire surface; and to accurately describe the noise generated when the excitation forces change significantly is necessary to assess all the different inputs that affect the tire and each of these inputs will have its own transfer functions.

The next chapter presents some of the different friction tests available and their limitations. It also presents a summary of friction testing done on different textured and tine surfaces and a relationship between friction and texture characteristics.

CHAPTER 7 IMPLICATIONS OF SURFACE TEXTURE ON SKID RESISTANCE OF PAVEMENTS

This chapter presents an analysis between friction resistance and surface texture profile. The surface texture was scanned using the approach described on CHAPTER 5. Friction testing was performed using the British pendulum (ASTM-E303) and the dynamic friction tester (ASTM-E1911). The following section describes some of the different friction testing equipment, how they work, and some of the implications on the use of the equipment.

7.1 Friction Testing

Skid resistance is an important aspect of road safety. The surface friction plays a key role in deciding which type of surface to use on a particular pavement. Skid testing can be performed using several methods, depending if the test is on site or in a laboratory.

7.1.1 Skid Trailer

Field testing is usually performed using a skid trailer (ASTM-E274) with geometry shown in Figure 7.1.1. The skid trailer can be towed behind a pick-up truck or van at a constant velocity while a nozzle dispenses water in front of the tire to simulate wet conditions. The test wheel of the trailer is coupled by a disc brake assembly to a calibrated force transducer, which measures the traction force and load on the wheel under braking. The skid trailer uses either a ribbed (ASTM-E501) or blank (ASTM-E524) test tire. The electrical/mechanical devices in the trailer are controlled by a computer in the pickup truck. The computer applies the brake in the skid trailer and detects the resultant wheel traction force, wheel load and vehicle speed and uses the

resulting force and time information to determine the friction of pavement for the standard test tire. The friction value detected is reported in real time.

Figure 7.1.1 Skid trailer (INDOT)

7.1.2 Dynamic Friction Tester

The dynamic friction tester (DFT) (ASTM-E1911) shown on Figure 7.1.2, consists of a spinning disk with its plain parallel to the test surface. This test can be performed on site or on laboratory samples provided that they have dimensions grater than 430 x 430 mm. Three rubber sliders are mounted on the lower surface of the spinning disk. The maximum tangential velocity the sliders can achieve is 90 km/h. Water is induced in front of the sliders. The testing is performed by lowering the spinning disk to the surface of the pavement and continuously monitoring the torque as the speed of the disk is reduced to a final stop by the friction between the pavement texture and the rubber sliders. The torque is transformed to a friction measurement by converting the torque to the force of the sliders and dividing it by the weight of the disk and motor assembly. The friction is recorded at 20, 40, 60, and 80 km/h. It is important to note that the DFT is not capable of distinguishing the direction of the surface; this implies that to the DFT is the same to have a longitudinal or transverse tining.

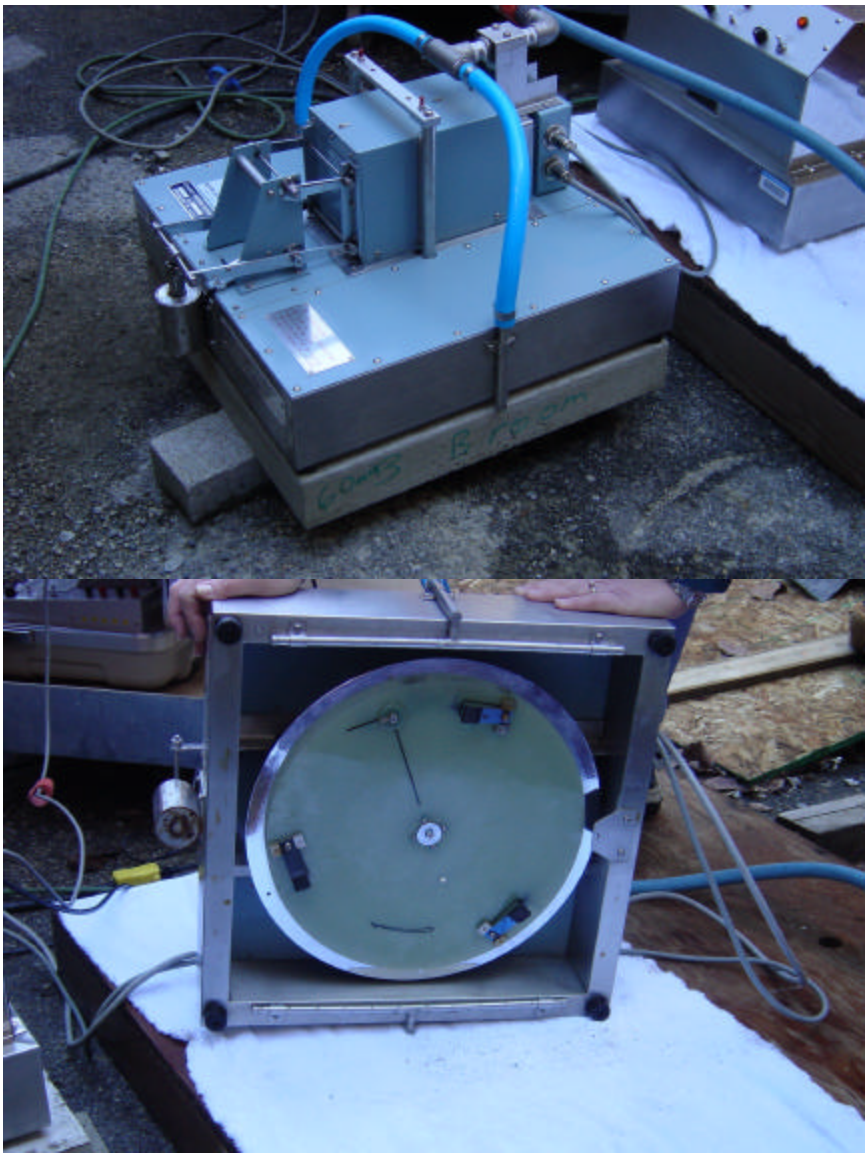

Figure 7.1.2 Dynamic friction tester

7.1.3 British Pendulum

Laboratory testing is usually done using the British pendulum (ASTM-E303) shown in Figure 7.1.3. This British pendulum consists of a pendulum type device with a rubber slider. The frictional properties of the surface are determined by releasing the pendulum. The test surface is previously cleaned and wetted before the test. The test is performed five times and the friction number is reported as the average of these tests.

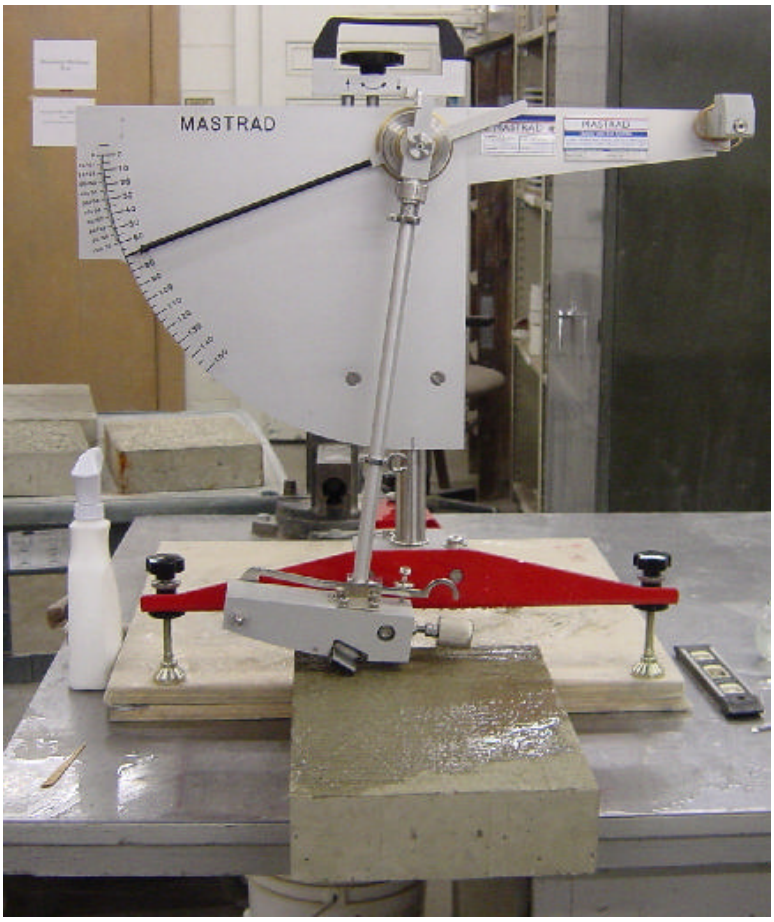

Figure 7.1.3 British pendulum set up

7.2 Testing different surface textures

Laboratory testing was done for the using the British pendulum (BP) and the dynamic friction tester (DFT) on several textured surfaces. The textured samples that were tested for friction using BP were also scanned using the laser profilometer to obtain the average texture depth.

7.2.1 British pendulum

Testing using the BP was performed on 381 by 254 mm slabs that were 75 mm thick. The slabs were tested at one, two, or four locations depending on the variability of the surface and the direction of travel, as shown in Figure 7.2.1. The size of each testing

location was 76.2 mm by 125 to 127 mm as required by ASTM-E303. To remove weak particles from the surface texture that may lead to friction resistance loss, the surface was altered using a wire brush. The friction number was obtained by averaging five consecutive tests on each testing location; the standard deviation was also calculated for each testing location.

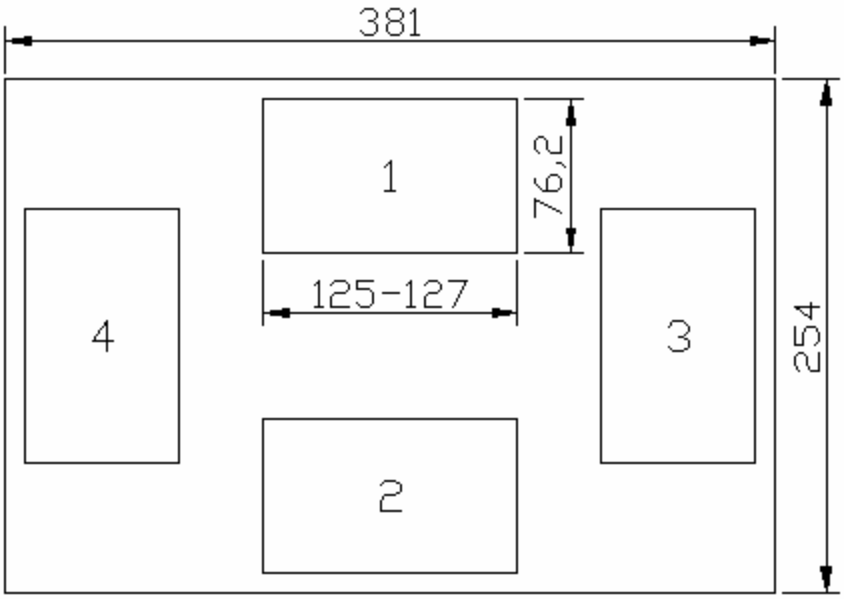

Figure 7.2.1 Slab dimensions for BP friction testing (mm), Numbers 1-4 indicate the individual test locations

Table 7.2.1 provides a summary of the different surfaces tested, describing if the test was done longitudinally or transversely, and the number of tests locations for each surface.

Table 7.2.1 Summary of the British pendulum friction testing plan

Type of surface	Testing direction	Number of locations
Grooved tines	Longitudinal and transverse	2
Astroturf original	Longitudinal	2
Astroturf brushed	Longitudinal	2
Magnesium trowel	Longitudinal	1
Ground tines	Longitudinal and transverse	2
Broom original	Longitudinal and transverse	4
Broom brushed	Longitudinal and transverse	4

7.2.2 Dynamic Friction Tester

Testing using the DFT was performed on 460 by 460 mm slabs that were 64 mm thick. The slabs were textured at 3 different times, 20, 40, and 60 minutes. The texturing methods used were: broom texture, Astroturf drag, finishing sponge texture, burlap drag plus grooved uniform spaced tining, and broom texture plus grooved uniform spaced tining.

The different setting time were used in order to asses the influence of time of texturing on the on average texture depth and friction properties. The different times were selected in order to have an early entry time (20 min), a late entry time (60 min), and average entry time (40 min).

The surfaces were cleaned with a wire brush before testing to remove any dust and loose particles. The testing was performed in accordance with ASTM E 1911. In order to calculate the International Friction Index (IFI) (ASTM E 1960) is necessary to obtain the average texture depth of the surface, this was done in accordance with ASTM E 2157. The average texture depth was obtained using the Circular Track Meter. The IFI was calculated using Equation 7.1. The international friction number is the result of applying a scaling factor to the friction data obtained directly from the DFT, this scaling factor lowers the skid number when the average texture depth is low and increases the skid number when the texture depth is high.

$$F_{60} = 0.081 + 0.732 \times DFT_{20} \times e^{\frac{-40}{108.1 \times MPD - 1.3}} \quad (7.1)$$

where:

DFT_{20} – Value at 20 kph from the DF Tester

MPD – Texture depth from CT Meter

7.3 Friction testing results

Table 7.3.1 shows the data collected from the dynamic friction tester. The data for the Astroturf texture at the setting times of 20 and 40 minutes was not obtained because the texture was uneven due to early entry time of the texturing procedure. The data for the broom and burlap plus tining for 20 minutes was not collected because the texturing procedure did not work at that early time; the grooves created by the rake were closing after the rake passed thru them because the surface of the concrete was in an early stage of setting. On Table 7.3.1 is shown that the highest IFI are for the tined pavement at a texturing time of 40 minutes, the values for 60 minutes are slightly lower. This behavior is constant thru the set of data having higher IFI for all the textures at a texturing time of 40 minutes in comparison with 60 min. For the case of the broom texture and the sponge finish, the friction numbers were higher for the 40 minutes than the 20 minutes texturing time.

Figure 7.3.1 shows a relationship between texturing time and the international friction index F-60. As previously discussed, there is a relationship between the texturing time and the friction properties of the surface. This trend on texturing time is clearly shown for the broom texture and the sponge finish texture and no so clearly for the broom tine and burlap tine texture due to the lack of data for a texturing time of 20 min. The trend shows that in order to achieve better fiction properties the texturing should be done at a “proper” time. This “proper” time will vary for different mixture proportions.

Table 7.3.1 Summary of friction testing using the Dynamic Friction Tester (ASTM E 1911)

Surface Texture Type	Time of Texturing	Average Texture Depth (mm)*	DFT 20**	IFI F-60***
Astroturf 60	60 min	1.45	0.790	0.53
Broom 20	20 min	0.52	0.435	0.23
Broom 40	40 min	0.58	0.735	0.36
Broom 60	60 min	0.44	0.781	0.32
Broom tine 40	40 min	1.20	0.942	0.59
Broom tine 60	60 min	1.27	0.866	0.55
Burlap tine 40	40 min	1.39	0.860	0.56
Burlap tine 60	60 min	1.28	0.808	0.52
Sponge 20	20 min	1.12	0.520	0.35
Sponge 40	40 min	0.85	0.736	0.43
Sponge 60	60 min	0.77	0.720	0.40

* ATD – obtained using the circular texture meter (ASTM E 2157)

** DFT 20 – obtained in accordance with ASTM E 1911

*** IFI F-60 – obtained from Equation 7.1 (ASTM E 1960)

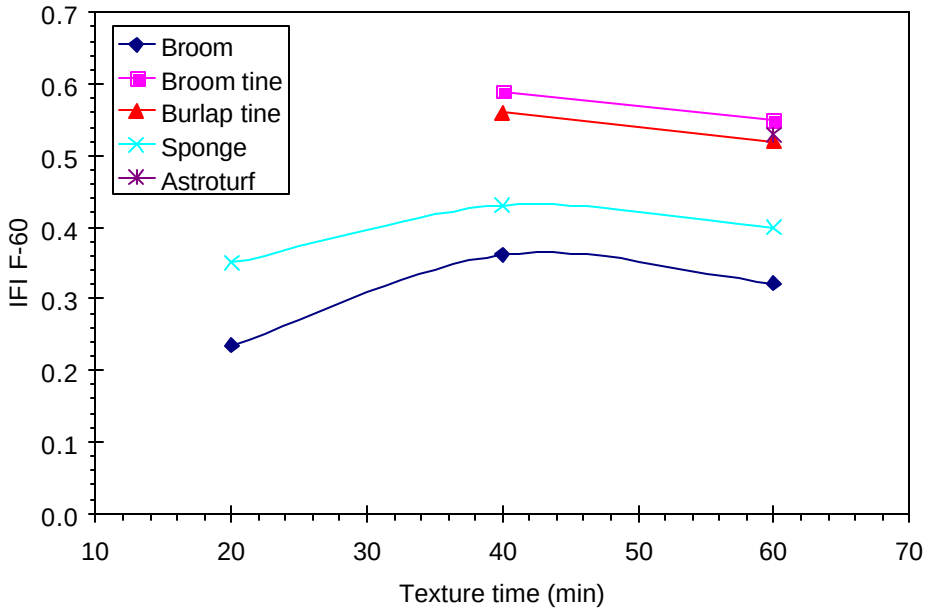

Figure 7.3.1 Relationship between texturing time and IFI F-60 for different textures

Figure 7.3.2 shows the average, maximum, and minimum values obtained for different surfaces tested with the British pendulum, and the information from Kuemmel [2000] on the skid trailer. The collected data for the BP testing is presented on Appendix C. The information from Kuemmel is presented as a reference in order to compare the friction numbers of the BP with the skid trailer. It can be seen that while there is some correlation between the BP friction numbers and the skid trailer number for the grooved longitudinal and transverse tining, but the variability is very different.

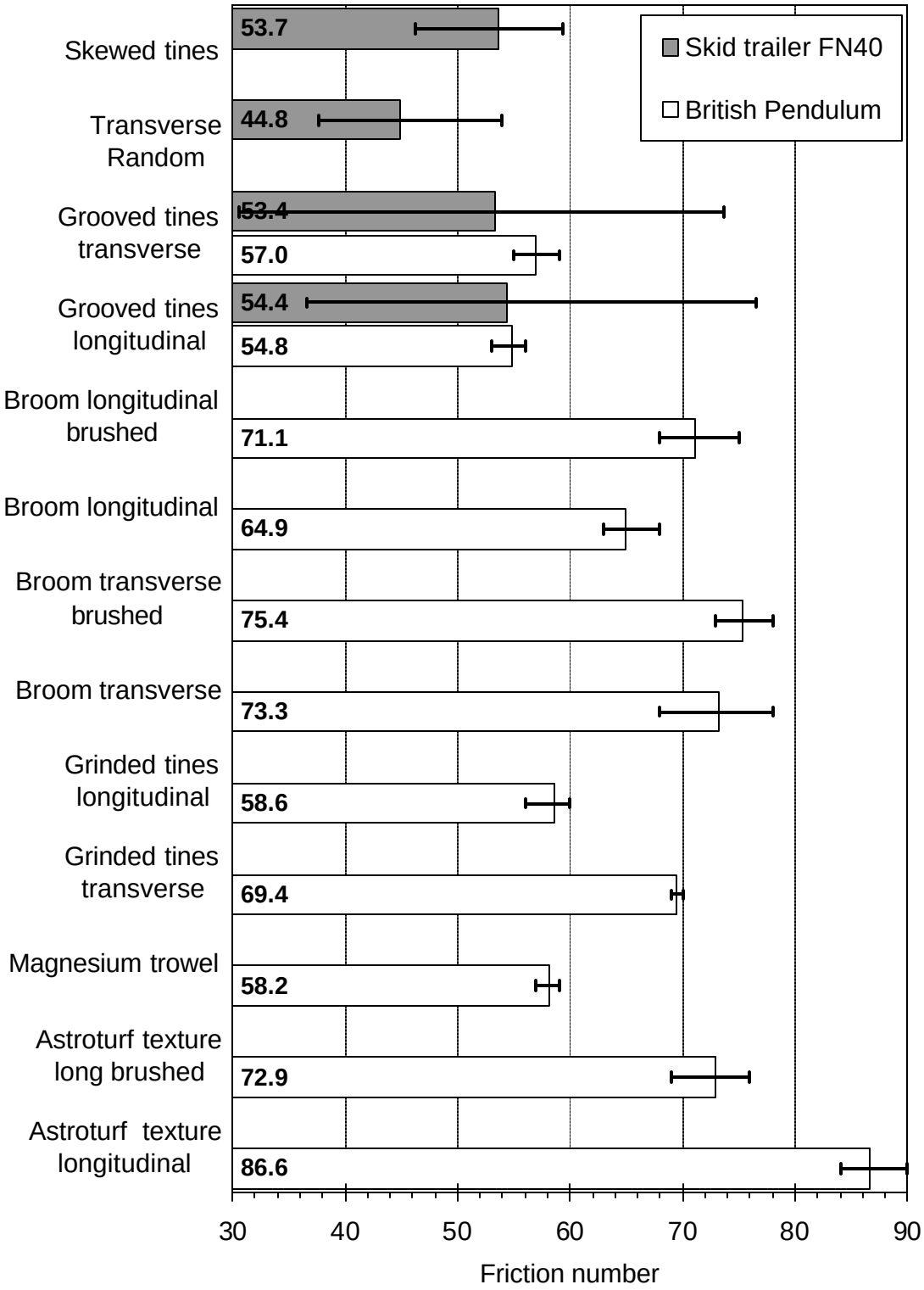

Figure 7.3.2 BP friction numbers for different surfaces obtained by testing and skid trailer (Fn 40 Bald) numbers from Kuemmel [2000] (notes: the surfaces may not be exactly the same, the number denotes the average value)

7.3.1 Comparing Friction Numbers and Textures Mean Depths

Friction between two bodies is achieved by the surface irregularities or roughness and force between both surfaces. The roughness of the surface can be measured as the average depth for each type of surface. In order to relate the friction properties of a surface with the noise generated as the tire rolls over the surface is necessary to find a characteristic that influences both of these aspects. A characteristic proposed to relate these aspects is texture depth.

Figure 7.3.3 shows a relationship between the average texture depth for different textured surfaces as obtained in section 5.4 and the friction number as obtained in section 7.2.2 . A linear trend can be seen relating the friction number with the mean depth. The different textures used in this relationship were Astroturf, magnesium trowel finish, broom transverse, and broom longitudinal.

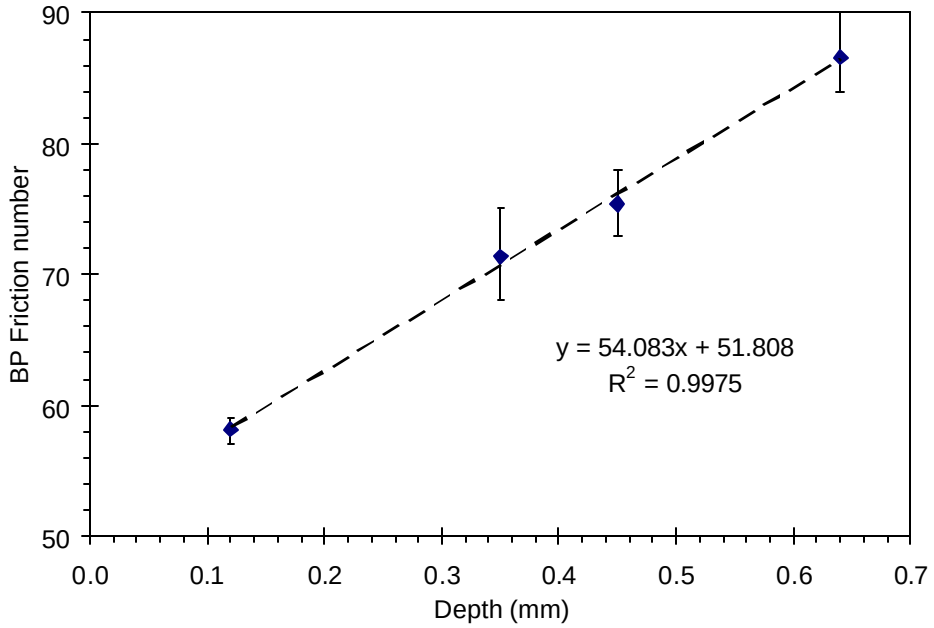

Figure 7.3.3 Relationship between the laser profilometer measure of texture depth and the British pendulum measure of friction number

Figure 7.3.4 shows a relationship between the average texture depth and the DFT value for 20 km/h the different textures used in this relationship are shown on Table 7.3.1. The relationship between DFT and the averaged texture depth is not as good as the one for the BP. However, there is the same tendency of higher friction as the average

texture depth increases. Some of the factors affecting this relationship are: First, the dynamic friction tester does not sense the direction of the texture in comparison with the British pendulum. Second four of the tested surfaces involve tines; that were not tested on the British pendulum.

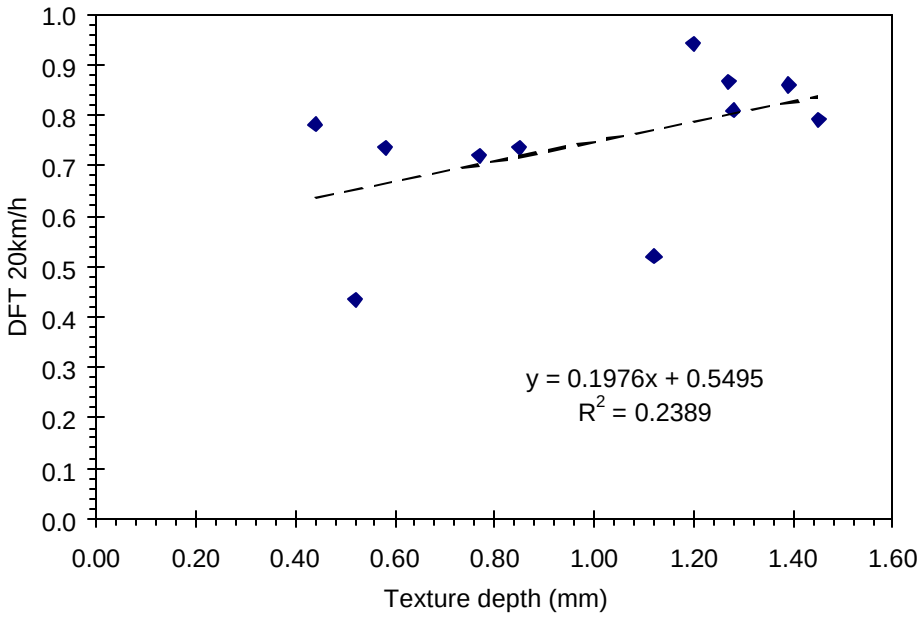

Figure 7.3.4 Relationship between dynamic friction tester numbers at 20 km/h and average texture depth

7.4 Friction and Noise

Friction and noise are two different phenomenons that occur while the tire rolls over a pavement. Figure 7.4.1 shows a relationship obtained from different textured surfaces relating the overall noise level obtained from testing on the TPTA and the friction numbers obtained by testing with the British pendulum. It is important to note that the overall noise levels obtained for these pavements are frequency averaged, this implies that they are considering noises like air pumping and wind noise generated by the tire. As it is shown in Figure 7.4.1, there is a trend as the friction number increases the overall noise level also increases, but there appears to be a limit to the amount of noise that can be produced.

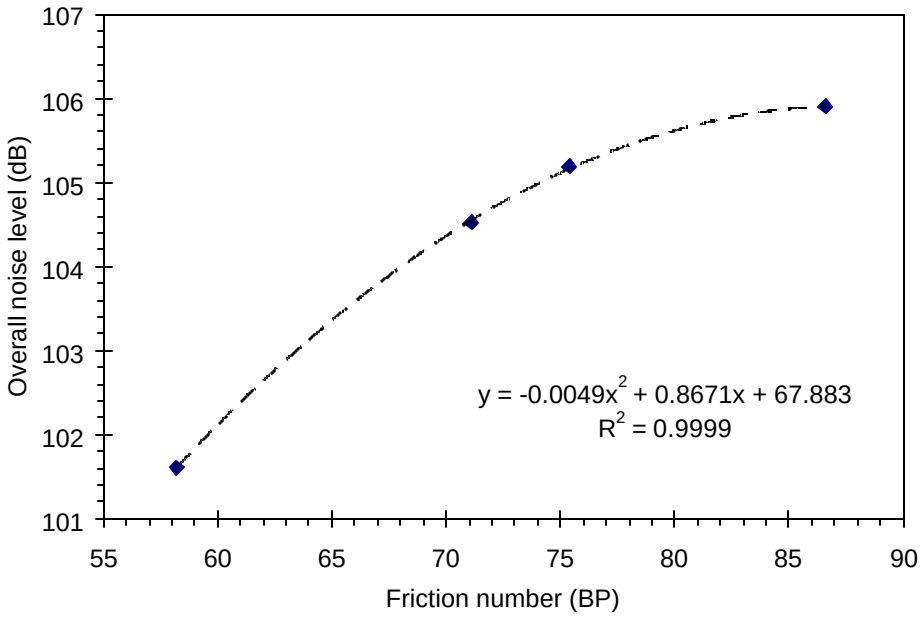

Figure 7.4.1 Relation of Friction numbers (British pendulum) and overall noise level (TPTA Frequency averaged)

7.5 Chapter Conclusions

Friction testing was performed by two different methods on different types of surfaces. First friction was performed using the British pendulum on surfaces with the same finish as the ones mounted on the TPTA. Second friction testing was performed using the dynamic friction tester to assess the influence of texturing time on friction and texture depth. A linear relationship was found for friction data obtained with the British pudendum and the texture depth obtained with the laser profilometer. The texturing time has an influence on the friction properties of the surface, there appears to be an optimum texturing time that depends on the desired surface and the mixture proportion of the concrete.

On the next chapter, a summary of this paper is presented and the final conclusions are drawn.

CHAPTER 8 SUMMARY AND CONCLUSIONS

This work details the results from a study that was conducted to link the surface characteristics of portland cement concrete pavements (depth, width, and shape of tines and surface texture) with the noise generated as a result of pavement/tire interaction. Noise spectra were modeled for several different pavement surfaces and compared with the noise spectra obtained on pavement surfaces in the laboratory. The main conclusions that can be drawn from this study are presented here.

8.1 Summary

8.1.1 Influence of Tine Geometry and Surface Texture on Noise Modeling

Contact stress modeling was performed to obtain an estimation of the input force spectrum component of the noise that the tire generates when rolling over different tine geometries and surfaces. The features of the tine geometry that were investigated included width, depth, and shape of the tine.

The results of the modeling efforts indicate that changing tine width affects primarily the modulation frequency of the input force spectrum without significantly change on the overall level. Rounding the edges of the tine resulted in the same tendency as varying tine width, that is in it lead to a change in the modulation frequency of the input force spectrum. Changing the geometry of the tine into a bevel did not produce significant changes for angles greater than 5°.

In order to model stress and noise associated with different surface textures it was necessary to characterize the surface profile. The profiles of the different surfaces (Astroturf longitudinal, magnesium trowel finish, broom longitudinal, and broom

transverse) were obtained using a laser profilometer and used in models that generated input force spectra. In addition, the average texture depth was obtained for each of these surfaces for the purpose of evaluating their friction characteristics.

8.1.2 Testing on the Tire/Pavement Test Apparatus (TPTA)

Testing using the TPTA was performed on different surfaces to assess the noise levels generated by a full-size tire traveling over different surface textures, tining shapes and patterns. The surfaces tested included: magnesium trowel finish, ground concrete, broomed longitudinal, broomed transverse, Astroturf longitudinal textures. In addition surfaces with transverse tines of different geometries (square, beveled, and rounded edge), and evenly spaced transverse square tines were also evaluated.

The results indicate that as the texture becomes rougher, the noise level increases. In general changing the width of the tine resulted in higher overall noise levels without any significant change in the shape of the frequency spectrum. Using rounded or beveled edges of the tines also did not result in significant change in the noise levels and the general shape of the spectrum.

8.1.3 Correlation of the Model and the TPTA Noise Spectra

In order to correlate the input force spectrum obtained by modeling with the noise spectrum obtained from the TPTA, it was necessary to generate a transfer function that would take into account tire dynamics and acoustic radiation. The transfer functions were generated by dividing the measured spectra by the modeled spectra.

The transfer functions for the textured pavements were similar to each other. The transfer functions for tines with beveled edge and rounded edge were also very similar to each other, but were substantially different than the ones for the textured surfaces. The transfer functions for the tines with different widths also substantially differ from each other.

8.1.4 Relating Friction to Texture Depth and Noise

Friction testing was performed on selected surfaces in order to assess the influence of texture depth on friction resistance. The friction testing was done using the British pendulum and the dynamic friction tester. The noise and surface friction were related using average texture depth. The overall noise level increased as the friction increased.

8.2 Conclusions

From the stress-noise modeling and the testing conducted on the TPTA it can be concluded that the shape of the edge of the tine does not significantly affect the overall noise level or the shape of the spectrum generated. However, the influence of the width of the tine was significant. The above conclusions apply only to tines perpendicular to the traffic direction. Reducing tine width will result in a reduction in the overall sound level.

Application of a FFT to the contact stress distribution between a pavement and a tire does not represent the input force spectrum of the noise generated in the TPTA by the tire rolling over the pavement. A change of tine width in the mathematical model produces a change on the modulation frequency of the power spectral density (PSD) plot with minimal or no change in the overall sound level of the spectrum. However, a change of tine width on the TPTA generates PSD plots with similar frequency content but different overall sound level.

8.3 Recommendations for Future Study

Research should be conducted to further develop a model that can provide a transfer function for each source thereby enabling the different paths of vibrational waves in the tire to be properly accounted for.

Similarly more studies are required on development of pavement texture that can provide desirable levels of safety and reduction in noise levels. In order to develop such texture it will be necessary to establish a fundamental understanding of the relationships between surface characteristics that influence both frictional properties of pavements, and generation of noise.

REFERENCES

ACI 325-88 (1988); "Texturing Concrete Pavements", reported by the American Concrete Institute Committee 325.

Alfosso-Ledee, F., et al (2000); "Tire/Road Noise Comparison of 2D and 3D Models for Horn Effect", Inter-Noise 2000.

Berengier, M. and F. Alfosso-Ledee (1998); "State-Of-The-Art on Prediction and Control of the Road Traffic Noise in France", TRB paper 980691, Transportation Research Board, Washington D.C., USA.

Brite Euram 3415 (1994); "Surface Properties of Concrete Road in Accordance with Traffic Safety and Reduction of Noise", State-of-the-art report, October 1994.

Bruel and Kjaer (2000); "Environmental Noise", instructional booklet, available at http://www.bksv.com/pdf/Environmental%20Noise%20Booklet.pdf.

Clapp, T. G., A. C. Eberhardt, and C. T. Kelly (1988); "Development and Validation of a Method for Approximating Road Surface Texture-Induced Contact Pressure in Tire-Pavement Interaction", Tire Science and Technology 16, pp 2-17.

Descornet, G. (2000); "Traffic Noise and Road Surfaces: State-of-the-Art", Belgian Road Center, editor.

Descornet, G., F. Fuchs, and R. Buys (1993); "Noise-Reducing Concrete Pavements", 5th International Conference on Concrete Pavement Design and Rehabilitation. Purdue University, West Lafayette, IN.

Donavan, P. R. (2002); "Examination of Tire/Road Noise at Frequencies Above 630 Hertz", The 2002 International Congress and Exposition on Noise Control Engineering, Dearborn, MI, USA August 19-21, 2002.

Fahy, Frank (1985); "Sound and Structural Vibration Radiation Transmission and Response", Academic press London.

Heerkens, J. C. and G. G. Van Bochove (1998); "Twin-Lay a new Concept of Drainage Asphalt Concrete", Proceedings Euro-Noise 98, Munich, Germany.

ISO/CD 11819-2 (2000); "Measurement of the Influence of Road Surfaces on Traffic Noise—Part 2: The Close-Proximity Method", Draft Standard ISO/CD11819-2 (International Organization for Standardization, Geneva, Switzerland, 2000).

Kim, Yong-Joe (2003); "Visualization of Tire Vibration and Sound Radiation and Modeling of Tire Vibration With an Emphasis on Wave Propagation", PHD Thesis, Purdue University, August 2003.

Kuemmel, D. A., R. C. Sonntag, J. A. Crovetti, Y. Becker, J. R. Jaeckel, and A. Satanovsky. (2000); "Noise and Texture on PCC Pavements – Results of a Multi-State Study", Report Number WI/SPR-08-99. Wisconsin Department of Transportation, Madison WI.

Longman, A. and J. Weiss (2002); internal report, Purdue University.

Nelson, P. M., and S. Phillips (1994); "Designing Porous Road Surfaces to Reduce Traffic Noise", Transportation Research Laboratory Annual Review 1994, Transportation Research Laboratory, Crow Thorne, England.

PIARC (1991); "Report of the Technical Committee on Surface Characteristics", XIXth World Road Congress – Marrakesh.

Sandberg, U and J. A. Ejsmont (2002); "The Influence of Tire Age and Wear on Tire/Road Noise Emission".

Sandberg, U and J. A. Ejsmont (2002);" Tire/Road Noise Reference Book" ISBN 91-631-2610-9.

Sandberg, U. and G. Descornet (1980); "Road Surface Influence on Tire/Road Noise", Proceedings Inter-Noise 80. Miami Florida, USA.

Sandberg, U.; (1999) "Low Noise Road Surfaces- A-state-of-the-Art Review", Journal Acoustical Society Japan.

Von Meier, A (1988); "Acoustically Optimized Porous Road Surfaces. Recent Experiences and New Developments", Proceedings Inter-Noise 88, Avingnon.

Von Meier, A (1992); "Thin Porous Surface Layers –Design Principles and Results Obtained", Proceedings Eurosymposium "The mitigation of Traffic Noise in Urban Areas", LCPC, Nantes, France.

Wayson (1998); "Relationship Between Pavement Surface Texture and Highway Traffic Noise", - NCHRP Synthesis 268, Transportation research board.

Appendix A Acoustics

Table A.1.1 $^1/_3$ octave band limits

$^1/_3$ octave band		
Lower cut off frequency	Center frequency	Upper cut off frequency
14.1	16	17.8
17.8	20	22.4
22.4	25	28.2
28.2	31.5	35.5
35.5	40	44.7
44.7	50	56.2
56.2	63	70.8
70.8	80	89.1
89.1	100	112
112	125	141
141	160	178
178	200	224
224	250	282
282	315	355
355	400	447
447	500	562
562	630	708
708	800	891
891	1000	1122
1122	1250	1413
1413	1600	1778
1778	2000	2239
2239	2500	2818
2818	3150	3548
3548	4000	4467
4467	5000	5623
5623	6300	7079
7079	8000	8913
8913	10000	11220
11220	12220	14130
14130	16000	17780
17780	20000	22390

Matlab program for executing $^1/_3$ octave filtering:

```
%input f and amp
%program for transforming to 1/3 octave band
 thirdoctave=[14.1 16 17.8;17.8 20 22.4;22.4 25 28.2;28.2 31.5, 35.5;35.5 40 44.7;44.7
50 56.2;56.2 63 70.8;70.8 80 89.1;89.1 100 112; 112 125 141; 141 160 178; 178 200
224;224 250 282;282 315 355;355 400 447;447 500 562; 562 630 708; 708 800 891;
891 1000 1122; 1122 1250 1413;1413 1600 1778; 1778 2000 2239;2239 2500
2818;2818 3150 3548;3548 4000 4467;4467 5000 5623;5623 6300 7079;7079 8000
8913;8913 10000 11220; 11220 12220 14130; 14130 16000 17780;17780 20000
22390];
for n=1:32;
    a(n)=10*log10(sum(10.^(amp(find(f>=thirdoctave(n,1) & f<=thirdoctave(n,3)))/10)));
    fm(n)=thirdoctave(n,2);
end
```

Table A.1.2 “A” weighting response

A weighting response	
Frequency (Hz)	A weighting (dB)
10	-70.4
12.5	-63.4
16	-56.7
20	-50.5
25	-44.7
31.5	-39.4
40	-34.6
50	-30.2
63	-26.2
80	-22.5
100	-19.1
125	-16.1
160	-13.4
200	-10.9
250	-8.6
315	-6.6
400	-4.8
500	-3.2
630	-1.9
800	-0.8
1000	0.0
1250	0.6
1600	1.0
2000	1.2
2500	1.3
3150	1.2
4000	1.0
5000	0.5
6300	-0.1
8000	-1.1
10000	-2.5
12500	-4.3
16000	-6.6
20000	-9.3

Matlab program for “A” weighting:

```
%input freq and logpsd
awe=[-70.4 -63.4 -56.7 -50.5 -44.7 -39.4 -34.6 -30.2 -26.2 -22.5 -19.1 -16.1 -13.4 -10.9 -
8.6 -6.6 -4.8 -3.2 -1.9 -.8 0 .6 1 1.2 1.3 1.2 1 .5 -.1 -1.1 -2.5 -4.3 -6.6 -9.3];
fofa=[ 10 12.5 16 20 25 31.5 40 50 63 80 100 125 160 200 250 315 400 500 630 800
1000 1250 1600 2000 2500 3150 4000 5000 6300 8000 10000 12500 16000 20000];
awdiff = interp1(fofa,awe,freq,'cubic');
logpsda=logpsd+awdiff;
```

Matlab program for overall noise level

```
for N=1:32
if isinf(A(N));
A(N)=0;
end
end
NL=10*log10(sum(10.^(A/10)));
```

Appendix B Matlab Program for Stress Distribution and Frequency

This Matlab program takes as input an X, Y profile with a resolution of 0.1 mm and saves all data to the hard drive of the computer; two other programs are required to plot the data.

```
disp(' ')
disp('     PROVIDE THE FILENAME (MAX 8 LETTERS)')
disp('     THE THE FILE NAME MUST PUT IN BETWEEN APPOSTROPHIES')
filename=input('THE FILE NAME IS: ');
fil=[filename ];
   eval(['save ',fil,' hodi vedi']);
E=416000;
ExPa=18000;
% road profile data
nsamp=length(hodi);                    % nsamp = number of sampling points
dnsamp=hodi(2)-hodi(1);          % distance between neighboring points
I=round((nsamp-1)/3);            % I = number of knots
if 3*I+1 > nsamp
  vedi(3*I+1)=vedi(nsamp);
  hodi(3*I+1)=hodi(nsamp)+dnsamp;
end

ip=hodi(1);                  % Contact initial point
ep=hodi(3*I+1);              % Contact end point
xi=[ip:(ep-ip)/I:ep];        % positions of knots
h=(ep-ip)/I;                 % distance between knots

xj=hodi(1:3*I+1);            % position of sampling points; number=3*I+1

% Tire properties
%E=4.16e6;        % Young's modulus of elasticity of rubber
```

```
mu=0.45;          % Poisson's ratio of rubber
%ExPa=1.8e5;     % Static external loaded pressure, 1 psi = 6.894757 e3 Pa.
vspeed=10;        % Tire rolling speed

% determine the z matrix
for i=1:I
  for j=1:(3*I+1)
    d=xj(j)-xi(i);
    if d < 0
      z0(i,j)=(h-d)*log(h-d)+d*log(-d)-h;
      z1(i,j)=d*z0(i,j)+(h-d)^2/2*log(h-d)-(h-d)^2/4-d^2/2*log(-d)+d^2/4;
      z2(i,j)=d^2*z0(i,j)+2*d*((h-d)^2/2*log(h-d)-(h-d)^2/4-d^2/2*log(-d)+d^2/4)...
        +(h-d)^3/3*log(h-d)-(h-d)^3/9+d^3/3*log(-d)-d^3/9;
      z3(i,j)=d^3*z0(i,j)+3*d^2*((h-d)^2/2*log(h-d)-(h-d)^2/4-d^2/2*log(-d)+d^2/4)...
        +3*d*((h-d)^3/3*log(h-d)-(h-d)^3/9+d^3/3*log(-d)-d^3/9)...
        +(h-d)^4/4*log(h-d)-(h-d)^4/16-d^4/4*log(-d)+d^4/16;
    elseif d == 0
      z0(i,j)=h*log(h)-h;
      z1(i,j)=h^2/2*log(h)-h^2/4;
      z2(i,j)=h^3/3*log(h)-h^3/9;
      z3(i,j)=h^4/4*log(h)-h^4/16;
    elseif d > h
      z0(i,j)=d*log(d)-d-(d-h)*log(d-h)+d-h;
      z1(i,j)=d*z0(i,j)-(d^2/2*log(d)-d^2/4-(d-h)^2/2*log(d-h)+(d-h)^2/4);
      z2(i,j)=d^2*z0(i,j)-2*d*(d^2/2*log(d)-d^2/4-(d-h)^2/2*log(d-h)+(d-h)^2/4)...
        +d^3/3*log(d)-d^3/9-(d-h)^3/3*log(d-h)+(d-h)^3/9;
      z3(i,j)=d^3*z0(i,j)-3*d^2*(d^2/2*log(d)-d^2/4-(d-h)^2/2*log(d-h)+(d-h)^2/4)...
        +3*d*(d^3/3*log(d)-d^3/9-(d-h)^3/3*log(d-h)+(d-h)^3/9)...
        -(d^4/4*log(d)-d^4/16-(d-h)^4/4*log(d-h)+(d-h)^4/16);
    elseif d == h
      z0(i,j)=h*log(h)-h;
      z1(i,j)=d*z0(i,j)-(h^2/2*log(h)-h^2/4);
      z2(i,j)=d^2*z0(i,j)-2*d*(h^2/2*log(h)-h^2/4)+h^3/3*log(h)-h^3/9;
```

```
        z3(i,j)=d^3*z0(i,j)-3*d^2*(h^2/2*log(h)-h^2/4)+3*d*(h^3/3*log(h)-h^3/9)-
(h^4/4*log(h)-h^4/16);
      else
        z0(i,j)=d*log(d)-d+(h-d)*log(h-d)-(h-d);
        z1(i,j)=d*z0(i,j)+(h-d)^2/2*log(h-d)-(h-d)^2/4-d^2/2*log(d)+d^2/4;
        z2(i,j)=d^2*z0(i,j)+2*d*((h-d)^2/2*log(h-d)-(h-d)^2/4-d^2/2*log(d)+d^2/4)...
          +(h-d)^3/3*log(h-d)-(h-d)^3/9+d^3/3*log(d)-d^3/9;
        z3(i,j)=d^3*z0(i,j)+3*d^2*((h-d)^2/2*log(h-d)-(h-d)^2/4-d^2/2*log(d)+d^2/4)...
          +3*d*((h-d)^3/3*log(h-d)-(h-d)^3/9+d^3/3*log(d)-d^3/9)...
          +(h-d)^4/4*log(h-d)-(h-d)^4/16-d^4/4*log(d)+d^4/16;
      end
    end
end

% Create the stiffness matrix
G(1:3*I+1,1:3*I+1)=0;
for j=1:(3*I+1)
    mava=0;              % a dummy variable
    for i=1:I
      mava=mava+z0(i,j);
    end
    G(j,1)=mava;
end

for j=1:(3*I+1)
    for i=1:I
      mava=0;
      if (i+1) <= I
        for m=i+1:I
          mava=mava+z0(m,j);
        end
      end
      G(j,3*i-1)=z1(i,j)+h*mava;
```

```
    G(j,3*i)=z2(i,j)+h^2*mava;
    G(j,3*i+1)=z3(i,j)+h^3*mava;
  end
end

% The iteration process to determine the penetration depthh
ctdh=min(vedi);                % the minimum value of road profile
dctdh=(max(vedi)-min(vedi))/1200;  % increment in determining the penetration depthh
ctdhix=10;                     % an index

while ctdhix == 10
  for i=1:3*I+1
    if vedi(i) >= ctdh
      fx(i)=vedi(i)-ctdh;
    else
      fx(i)=0;
    end
  end

  % Create the road profile matrix
  for j=1:(3*I+1)
    F(j)=-pi*E/2/(1-mu^2)*fx(j)+pi*E/2/(1-mu^2)*fx(1);
  end

  % Calculate the general coefficient vector
  GB=G\F';

  % Create the B coefficient matrix
  for i=1:I
    if i == 1
      B(i,1)=GB(1);
    else
      B(i,1)=B(i-1,1)+B(i-1,2)*h+B(i-1,3)*h^2+B(i-1,4)*h^3;
```

```
  end
  B(i,2)=GB(3*i-1);
  B(i,3)=GB(3*i);
  B(i,4)=GB(3*i+1);
end

% Create the contact pressure from the B coefficient matrix
for j=1:(3*I+1)
  i=1;
  win=10;
  while win == 10
    if (xj(j) >= xi(i))&(xj(j) <= xi(i+1))
      win=11;
    else
      i=i+1;
    end
  end
  cp(j)=B(i,1)+B(i,2)*(xj(j)-xi(i))+B(i,3)*(xj(j)-xi(i))^2+B(i,4)*(xj(j)-xi(i))^3;
end

% Calculate the average contact pressure
avpa=0;
for i=1:3*I+1
  if cp(i) > 0
    avpa=avpa+cp(i);
  end
end
avpa=avpa/(3*I+1);

%fprintf('%e %e\n',ctdh,avpa);

if (avpa > 1.05*ExPa)   % If the calculated pressure is larger than the external pressure
  ctdh=ctdh+dctdh;     % lift the tire
```

```
  elseif (ctdh ~= min(vedi))&(avpa < 0.95*ExPa) % if the contact pressure is smaller
    ctdh=ctdh-dctdh/2;   % down the tire
  else
    ctdhix=11;
  end
end

% Important information that this program yields and will save

mhodi=xj;                    % modified horizontal displacement
mvedi=fx+ctdh;               % modified vertical displacement
freq=[0:255]/512*vspeed/dnsamp;   % frequency
cpp(1:3*I+1)=0;
for i=1:3*I+1
  if cp(i) > 0
    cpp(i)=cp(i);
  end
end

cpft=fft(cpp,512)*dnsamp/vspeed;   % FFT of the contact pressure
cpfft=cpft(1:256);
psd=abs(cpfft).^2/2/(nsamp*dnsamp/vspeed);
beep;
    fn = [fil,'out'];
    eval(['fprintf("\nSaved hodi vedi ctdh mhodi mvedi cp freq cpfft psd in
"',fn,'.mat"\n");']);
    eval(['save ',fn,' hodi vedi ctdh mhodi mvedi cpp freq cpfft psd ip ep']);
```

Stress distribution plotting program:

```
clear
fs=10;
dir=cd;
```

```
[filename,pathname] = uigetfile ('*.mat', 'Select the data',150,150); %load the  file
if filename==0
   clear
else

   cd(pathname);
   load(filename);

   lcpp=length(cpp);
   cpp(1)=cpp(2);
   cpp(lcpp)=cpp(lcpp-1);
   hodi=hodi*1000;
vedi=vedi*1000;
mhodi=mhodi*1000;
mvedi=mvedi*1000;
cpp=cpp/1000000;

hold off;
clear('AX','H1','H2');
ylim2=ceil(max(cpp));
plot(hodi,vedi,'color','black');
hold;
[AX,H1,H2] = plotyy(mhodi,mvedi,mhodi,cpp);
set(get(AX(1),'Ylabel'),'String','Heigth (mm)','fontSize',fs)
set(get(AX(2),'Ylabel'),'String','Stress (MPa)','fontSize',fs)
xlabel('Length (mm)','fontSize',fs)
set(gca,'linewidth',1)
set(H1,'LineStyle','--')
set(H2,'LineStyle',':')
set(AX(1),'fontsize',fs)
set(AX(2),'fontsize',fs)
set(AX(1),'YLim',[-10.5 10.5])
set(AX(2),'YLim',[-ylim2 ylim2])
```

```
set(AX(1),'YColor','black')
set(AX(2),'YColor','black')
set(H1,'Color',[.5 .5 .5])
set(H2,'Color','black')
set(AX(1),'YTick',[-10:2:0])
set(AX(2),'YTick',[0:ylim2/5:ylim2])
set(gcf,'paperposition',[.25 2 5 3.75])
filename=filename(1:length(filename)-7);
boucle=10;

while boucle==10;

deci2=menu('Save Picture','      yes      ', '      no      ');
if deci2==1
geo='geo';
bm='.tif';
fng=[filename geo bm];
cd('D:\My Documents\Researsh\paper');
saveas(gcf,fng,'tiff');
boucle=11;
end
if deci2==2
   boucle=11;
end
end
cd(dir);
end
```

Frequency plotting program:

```
%Load road profile filename.
clear
hold off
```

```
dir=cd;
fs=10; % font size
[filename,pathname] = uigetfile ('*.mat', 'Select the data',100,100); %load the  file

if filename==0
   clear
else

   cd(pathname);
   load(filename);
   dnsamp=hodi(2)-hodi(1);
   nsamp=length(hodi);
   vspeed=13.415;
   lcpp=length(cpp);
   cpp(1:20)=cpp(21);
   cpp(230:250)=cpp(229);

   doubletine=(round(((4.2E-3)*vspeed)/dnsamp))-lcpp;
   lt=doubletine+lcpp*2;

cpp=[cpp cpp];
vcpp=[1:250 lt-249:lt];
vcppm=1:1:lt;
cppin=interp1(vcpp,cpp,vcppm);
nsamp=length(cppin);
dnsamp=.0001;

freq=[0:511]/1024*vspeed/dnsamp;   % frequency
cpft=fft(cppin,1024)*dnsamp/vspeed;   % FFT of the contact pressure


cpfft=cpft(1:512);
```

```
psd=abs(cpfft).^2/2/(nsamp*dnsamp/vspeed);

 bm='.tif';
 filename=filename(1:length(filename)-7);

logpsd=10*log10(psd/4e-10);



awe=[-70.4 -63.4 -56.7 -50.5 -44.7 -39.4 -34.6 -30.2 -26.2 -22.5 -19.1 -16.1 -13.4 -10.9 -
8.6 -6.6 -4.8 -3.2 -1.9 -.8 0 .6 1 1.2 1.3 1.2 1 .5 -.1 -1.1 -2.5 -4.3 -6.6 -9.3];
fofa=[ 10 12.5 16 20 25 31.5 40 50 63 80 100 125 160 200 250 315 400 500 630 800
1000 1250 1600 2000 2500 3150 4000 5000 6300 8000 10000 12500 16000 20000];
awdiff = interp1(fofa,awe,freq,'cubic');
logpsda=logpsd+awdiff;

 thirdoctave=[14.1 16 17.8;17.8 20 22.4;22.4 25 28.2;28.2 31.5, 35.5;35.5 40 44.7;44.7
50 56.2;56.2 63 70.8;70.8 80 89.1;89.1 100 112; 112 125 141; 141 160 178; 178 200
224;224 250 282;282 315 355;355 400 447;447 500 562; 562 630 708; 708 800 891;
891 1000 1122; 1122 1250 1413;1413 1600 1778; 1778 2000 2239;2239 2500
2818;2818 3150 3548;3548 4000 4467;4467 5000 5623;5623 6300 7079;7079 8000
8913;8913 10000 11220; 11220 12220 14130; 14130 16000 17780;17780 20000
22390];
for n=1:32;
    a(n)=10*log10(sum(10.^(logpsda(find(freq>=thirdoctave(n,1) &
freq<=thirdoctave(n,3)))/10)));
    fm(n)=thirdoctave(n,2);
 end
```

Appendix C Friction Tests Data Obtained with the British Pendulum

Table C.1.1 Friction tests data obtained with the British pendulum

Texture Type	Test 1	Test 2	Test 3	Test 4	Test 5	Average	Standard deviation
Astroturf longitudinal 1	89	86	86	86	84	86.2	1.79
Astroturf longitudinal 2	90	89	84	88	84	87.0	2.83
Astroturf longitudinal brushed 1	73	69	70	71	70	70.6	1.52
Astroturf longitudinal brushed 2	76	76	76	74	74	75.2	1.10
Magnesium trowel longitudinal	59	59	58	58	57	58.2	0.84
Grinded Tines transverse	70	69	70	69	69	69.4	0.55
Grinded Tines Longitudinal	60	60	59	58	56	58.6	1.67
Broom transverse 1	72	72	71	68	71	70.8	1.64
Broom transverse 2	78	76	76	75	74	75.8	1.48
Broom transverse Brushed 1	78	77	76	75	75	76.2	1.30
Broom transverse Brushed 2	76	75	73	75	74	74.6	1.14
Broom longitudinal 1	68	66	65	64	64	65.4	1.67
Broom longitudinal 2	66	64	65	64	63	64.4	1.14
Broom longitudinal brushed 1	74	72	70	72	69	71.4	1.95
Broom longitudinal brushed 2	75	72	70	69	68	70.8	2.77
Cast tines longitudinal	56	56	55	54	53	54.8	1.30
Cast tines transverse	59	57	59	55	55	57.0	2.00